SMART BRICKS FOR THE POST-EARTHQUAKE ASSESSMENT OF MASONRY BUILDINGS

Dissertation
submitted to and approved by the

Faculty of Architecture, Civil Engineering and Environmental Sciences
Technische Universität Braunschweig

and the

Department of Civil and Environmental Engineering
University of Florence

in candidacy for the degree of a
Doktor-Ingenieur (Dr.-Ing.) /
Dottore di Ricerca in Civil and Environmental Engineering[*)]

by
Andrea Meoni
born 10/01/1990
from Castiglion Fiorentino (AR), Italy

Submitted on	16 April 2021
Oral examination on	17 June 2021
Professorial advisors	Prof. Dr.-Ing. Laura De Lorenzis Prof. Dr.-Ing. Filippo Ubertini

2021

*) Either the German or the Italian form of the title may be used.

Abstract

A wide part of the European built heritage consists of masonry constructions originally designed with very limited if not completely absent earthquake resisting criteria, exposing the structures to possible fragile collapse mechanisms during earthquakes. Therefore, it is evident that the evaluation of the health state of these types of buildings after a seismic event plays a fundamental role in the preservation of human life and the historical and cultural building heritage. Structural Health Monitoring (SHM) systems represent a possible solution to this problem by allowing the assessment of the structural performance of the monitored construction during its service life, even in real-time or rapidly after an earthquake, as well as enabling scheduling of maintenance and retrofitting interventions. Although the usefulness of such systems is widely recognized, their application on masonry constructions is still limited due to practical drawbacks experienced in the use of the off-the-shelf sensing technologies. Recent developments in materials engineering introduced in the field of SHM the use of smart materials obtained by doping traditional construction materials, such as cement-based ones, with conductive fillers capable of improving the electrical and sensing properties of the base matrix, giving to the composite the capability of detecting changes in its strain conditions through the output of specific electrical signals. This Ph.D. thesis extends a similar concept to masonry buildings investigating the innovative smart brick technology, which consists of clay bricks doped with suitable conductive fillers and thus capable of revealing changes in their strain conditions by leveraging on their improved piezoresistive capability, i.e. by varying their electrical outputs accordingly.

The Thesis aims to promote the development of this newly conceived technology by addressing the missing/incomplete aspects in the reference literature, with the main objective of comprehensively designing, producing, and characterizing a reliable smart sensing device suitable for seismic SHM of masonry constructions. The choice of the most suitable conductive filler, the type of electrodes to be used for electrical measurements, the production process, and the sensing principle of the smart bricks are investigated. Furthermore, experiments are carried out to properly characterize the electrical, electromechanical, physical, and mechanical properties of such brick-like sensors. The Thesis also proposes two meaningful full-scale applications of the smart brick technology to demonstrate the effectiveness of the novel sensors in detecting and locating damages developed on masonry constructions, in particular, by focusing the attention on those induced by earthquake loading. Strategies for performing damage detection and localization by processing the measurements from the smart bricks are therefore proposed, while mechanical models are built to reproduce the performed experimental tests with the aim of numerically interpreting the outputs from the novel sensors physically installed within the tested specimens. The obtained results demonstrate that the proposed new formulation of smart bricks can be effectively employed for the post-earthquake assessment of masonry constructions, bringing the technology to a readiness level that is mature for field validation.

Keywords: *Smart bricks, Masonry structures, Structural health monitoring, Damage detection and localization, Self-sensing structural materials, Smart materials.*

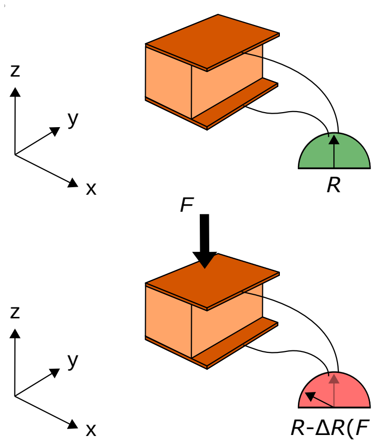

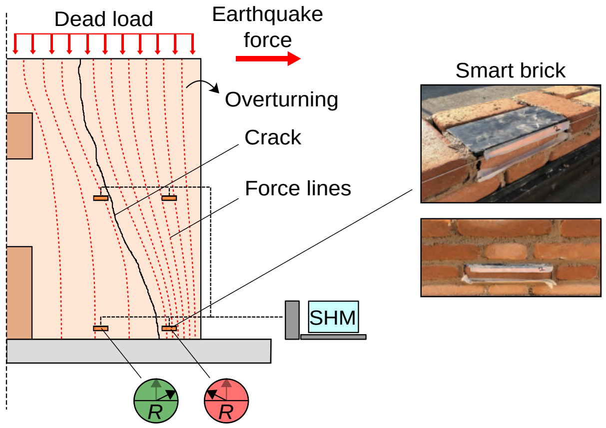

To my Family

Acknowledgements

This Thesis is the result of a joint International Doctoral Programme involving the Universities of Florence, Perugia, Pisa, and Braunschweig. In particular, the research activities object of this work were carried out by exploiting the facilities of the Department of Civil and Environmental Engineering of the University of Perugia and those of the Technische Universität Braunschweig under the supervision of Prof. Filippo Ubertini and Prof. Laura De Lorenzis.

First of all, I would like to express my sincere gratitude to my supervisor Prof. Filippo Ubertini. This research work would not have been possible without his knowledge and careful guidance. All my esteem goes to him.

Likewise, I am grateful to my supervisor Prof. De Lorenzis for sharing her knowledge with me with patience and dedication. A special thanks goes to her also for warmly welcoming me at the Technische Universität Braunschweig. It has been a wonderful experience.

I would like to sincerely thank my co-supervisor Dr. Antonella D'Alessandro. Her support, patience, and availability, as well as her contribution to the research activities, have been so important during these years.

A special thanks goes to Dr. Nicola Cavalagli and Dr. Roland Kruse for their support during the research activities and for sharing their knowledge with me. I really appreciated this.

I would like to express a huge thanks also to the other members of the Italian and German research group for the exchange of ideas over the years, their support, and help.

Finally, let me dedicate the biggest thanks to my Family. My parents, Vanna and Adriano, my brother, Alessandro, my sister-in-law, Francesca, my nephew, Augusto, and my sweetheart, Josephine.
No words are needed to say why. This work is dedicated to them.

Contents

List of Figures

List of Tables

Chapter 1

Introduction

1.1 Background and motivations

Recent Italian seismic events have sparked the interest of the entire European Community on the issue of the seismic vulnerability assessment of the built heritage, pointing out how the inadequate seismic safety level of several existing structures, most of which designed with outdated or even without any criterion for earthquake resistant design, is among the main causes of earthquake-induced damages and significant human, financial and functionality losses that occurred in the last decades. The situation is even more serious considering that about 60% of the European building heritage is represented by masonry structures, including historic and monumental constructions, which are typically prone to premature collapses, without any sign useful for early warning, due to the development of fragile crisis mechanisms during seismic events (Fig. 1.1).

In light of that, the preventive conservation of residential and cultural masonry buildings against the seismic hazard is an urgent priority, which demands tools capable of providing a quick evaluation of the structural conditions of the struck constructions immediately after an earthquake, so as optimizing retrofit and restoration interventions and, if necessary, promptly installing safety provisions for preventing further collapses during after-shocks.

Figure 1.1: Illustrations of earthquake-induced damages on masonry structures.

A possible solution to address this need in the field of structural engineering is to equip masonry structures with appropriate Structural Health Monitoring (SHM) systems for the evaluation of their structural integrity in real-time, including their post-earthquake assessment. Indeed, information gathered from SHM systems can be extremely useful to reveal if the construction being monitored is safely operational or it has reached some limit state. Nevertheless, despite the benefits that SHM systems can provide, their large-scale deployment in masonry constructions is rather limited nowadays, mostly due to practical drawbacks experienced in the use of the off-the-shelf sensing technologies. These, by possessing physical and mechanical properties very far from those of the monitored structures, pose questions concerning their effectiveness in reproducing the actual response of the masonry, as well as concerning their durability against environmental actions. Logistical difficulties, such as limitations in the number of sensors deployable in the case of aesthetic and architectural restrictions, are also frequent when dealing with the monitoring of historic and monumental masonry constructions.

A very attractive solution to the listed issues is represented by the adoption of the concept of smart material for replacing traditional sensing devices with smart sensors possessing physical and mechanical properties similar to those of the structure being monitored. According to such an innovative concept, the sensing capabilities of these newly conceived devices are typically obtained through the addition of electrically conductive nano- or micro- fillers to the traditional construction materials during their production process so as enhancing their intrinsic piezoresistivity. Smart sensors are therefore fully integrable within the load-bearing structures allowing spatially distributed and long-term reliable automated monitoring systems based on strain measurements without altering their structural response.

Along these lines, this Ph.D. thesis proposes the development of a new sensing technology based on brick-like sensors, called "smart bricks", for seismic SHM of masonry constructions. These novel sensors are characterized by an improved piezoresistivity, which allows them to provide traditional masonry constructions with smart monitoring capabilities enabling the self-assessment of their structural conditions over time. The main objectives promoted by this work to address missing/incomplete aspects in the reference literature are:

- Development of a new sensing technology for seismic SHM of masonry constructions, termed smart brick, determining the most suitable electrically conductive filler to be used for boosting piezoresistive capabilities in clay-based materials, as well as the most appropriate type of electrodes to be used for performing electrical measurements;
- Propose and validate an electromechanical model suitable for describing the strain-sensing behavior of the smart bricks. This should be usable for retrieving strain measurements through the post-processing of the electrical outputs from these innovative piezoresistive sensors;
- Provide a comprehensive characterization of the electrical, electromechanical, physical, and mechanical properties of the novel sensors according to the content of the electrically conductive filler used for their production;
- Determine and compensate the influence of environmental effects, due to changes in temperature and humidity, on the electrical response of the smart bricks;
- Development of damage detection and localization algorithms for real-time processing of data outputted by smart bricks allowing the assessment of the structural integrity of masonry constructions during their service conditions;
- Perform the experimental validation of the proposed damage detection and localization methods through a campaign of experimental and numerical investigations carried out on small- and full- scale masonry structures equipped with smart bricks and tested until damaged.

1.2 Outline

This work is organized in six chapters including conclusions. The main contents of each chapter are summarized as follows:

- **Chapter 1: Introduction**
  A general overview concerning background and motivations of the research. The main objectives of the work are also introduced.

- **Chapter 2: Structural health monitoring of masonry structures based on strain measurements**
  A review on the state-of-the-art regarding SHM techniques commonly applied to masonry constructions is addressed in this chapter, mainly focusing the attention on traditional and new monitoring approaches based on the assessment of strain-measurements.

- **Chapter 3: Modeling approaches for masonry structures**
  This chapter is dedicated to a critical analysis of the modeling strategies adopted for the definition of mechanical models for masonry that are available in the literature. A detailed overview on the computational tools and Finite Element (FE) analyses considered in this work is also presented.

- **Chapter 4: A new sensing technology for SHM of masonry structures: The smart brick**
  This chapter introduces the smart brick technology, illustrating the novelties pioneered by this work in the manufacturing process of the novel sensors and proposing an innovative electromechanical model to describe their strain-sensing behavior. A campaign of laboratory tests is presented to deeply investigate the electrical, electromechanical, physical, and mechanical properties of the new formulation of the smart bricks. The influence of the environmental effects on the electrical outputs of the novel sensors is also investigated.

- **Chapter 5: Applications of the smart brick technology**
  Meaningful experimental applications of the smart brick technology are introduced in this chapter to demonstrate that the novel sensors are effective for monitoring the structural integrity of masonry constructions. In light of that, damage detection and localization algorithms, based on the strain measurements from the smart bricks, are proposed and validated by means of their practical application to the considered case

studies. Numerical simulations are also carried out to interpret the outputs from the novel sensors.

- **Chapter 6: Conclusions**
  Further comments and remarks are reported in this closing chapter.

Chapter 2

Structural health monitoring of masonry structures based on strain measurements

2.1 Introduction

The European cultural and monumental building heritage is largely composed of masonry constructions characterized by a great historical importance such as churches, towers, and palaces. Even in the case of residential constructions, each masonry building can be considered unique since characterized by its own history including its initial design, the construction phases, and any modifications suffered during its service life. As a drawback, due to the variability of the events that may have influenced the story of a masonry construction, it generally appears difficult to define a simplified and schematic mathematical approach, based on the knowledge about utilized materials and adopted building techniques, for the evaluation of its structural response in service condition (De Fino and De Tommasi 2008). As an aggravating circumstance, it is worth noting that the largest part of the ancient masonry constructions were conceived to resist only to gravity loads resulting in the development of fragile collapses, frequently facilitated by poor maintenance conditions and material degradation, in the case of excessive tensile and shear forces acting during earthquake ground motions. Therefore, the real-time assessment of the structural response of masonry constructions plays a key role in the preventive conservation of the cultural heritage and in maintaining safety operational conditions for human lives. To this aim, continuous SHM systems represent a powerful tool for the observation of the structural performance/integrity of masonry buildings during their service life, permitting the identification of developing damages or critical conditions in real-time and the optimization of retrofitting and maintenance interventions based on up-to-date information.

With the main objective of framing the problem, this chapter deals with a literature review on the state-of-the-art of both traditional and innovative SHM techniques commonly applied to masonry constructions. The rest of the chapter is organized as follows. Section 2.2 reviews off-the-shelf sensing technologies with particular attention to SHM solutions employing strain measurements. Section 2.3 deals with innovative monitoring techniques based on the smart material concept, which was recently extended to the field of masonry constructions after the promising results achieved in the monitoring of concrete structures. Section 2.4 concludes the chapter with comments and remarks.

2.2 On the advantages of strain measurements for SHM of masonry structures

Masonry constructions are particularly prone to brittle collapses and structural pathologies commonly caused by excessive deformations, temperature- and load-induced stresses, differential foundation settlements, and earthquake loading. Monitoring the health state of a building during its service life can aid the preservation of its structural integrity over the time and the detection/localization of developing damages, with obvious benefits for establishing the existence of safety conditions for human lives immediately after a seismic event or in terms of managing costs for restoration and maintenance, through the planning of targeted interventions avoiding the reduction of the structural capacity (Lagomarsino 2006; De Lorenzis et al. 2007; Masciotta et al. 2017; Formisano et al. 2018). SHM is defined as the automation of damage detection, localization, and prognosis of structural systems and components (Sadoughi et al. 2018a). To date, SHM systems allow the continuous evaluation of the structural behavior of masonry constructions through the assessment of changes in static and dynamic response parameters properly selected (Saisi et al. 2018). As a general overview, Table 2.1 reports meaningful examples of SHM systems adopted for the long-term monitoring of historical masonry structures.

Table 2.1: Meaningful examples of SHM systems adopted for the long-term monitoring of historical masonry structures.

Structure	No.	Sensor Typology	Literature reference
Consoli Palace	3	Piezoelectric accelerometer	Kita et al. (2019)
	2	LVDT	
	2	Thermocouple K-type	
Palazzo Comunale di Castelfidardo	14	Capacitative accelerometer	Pierdicca et al. (2016)
Peristyle of Diocletian's Palace	7	Resistive strain gauges	Duvnjak et al. (2016)
	9	LVDT	
	1	Temperature sensor	
Chiesa Santa Maria di Collemaggio	9	High precision triangulation laser (crack measurement)	Alaggio et al. (2020)
	78	Force-balance accelerometer	
	5	Temperature/humidity sensor	
Milan Cathedral	12	Vibrating wire extensometer	Gentile et al. (2019)
	15	Bi-axial tilt meter	
	15	Temperature sensor	
	12	Hygrometer	
	1	Weather station	
	13	Bi-axial seismometer	
	10	Mono-axial seismometer	
Foz Coa's Church	3	LVDT	Mesquita et al. (2018)
	1	Potentiometer	
	1	Clinometer	
	2	Temperature sensor	
	1	Humidity sensor	
Sciri Tower	3	Piezoelectric accelerometer	Venanzi et al. (2020)
	2	Thermocouple K-type	
Gabbia Tower	3	Piezoelectric accelerometer	Ubertini et al. (2018)
	1	Temperature sensor	
San Pietro belfry	3	Piezoelectric accelerometer	Gentile et al. (2016)
	8	Temperature and humidity sensor	

A technique widely applied to this structural typology, in particular to slender structures such as towers and belfries, to assess their global structural behavior by using a limited number of sensors, is the long-term vibration-based monitoring. In this approach, dynamic parameters, such as the natural frequencies of vibration, are continuously monitored, usually by using accelerometers, to detect changes in their values correlated to local modifications in the structural stiffness, typically caused by damage initiation and material degradation (Ramos et al. 2010; Krstevska et al. 2010; Saisi et al. 2014). Nevertheless, despite the great potential shown by such approaches for the global assessment of the structural integrity, monitoring techniques based on dynamic parameters may fail when damages are extremely localized or when their severity is such that the dynamic response of the structure is not affected. In these cases, SHM techniques based on static parameters, such as displacements, tilts, and strain measurements may be more effective allowing the assessment of the evolution of cracks in localized portions of the structure by means of the installation of linear variable differential transformers (LVDT)s, tiltmeters, and resistive strain gauges (RSG)s (Vermeltfoort et al. 2007).

Many literary works demonstrated that the development of damages to the structures induces anomalies in their stress/strain field that can be revealed by using suitable monitoring approaches. Considering the lack of effective tools for carrying out a continuous evaluation of the stress field in masonry constructions, SHM techniques based on strain measurements represent a precious resource for gathering data to assess the integrity of the structures during their service conditions (Dally and Sanford 1987; Berger and Dally 1988; Yoshimura et al. 2004). Among the off-the-shelf strain-sensing technologies, RSGs appear conceivably the maturest and widespread devices adopted for monitoring strain in several research fields, including SHM of masonry constructions (Heise 1965; Kuang and Chen 1995; Martinez et al. 2008). As a general example of their operation, in Duvnjak et al. (2016) strain gauges were employed in a continuous monitoring system for the real-time assessment of a historical palace, demonstrating their usefulness for detecting the growth of existing cracking patterns (Fig. 2.1).

Figure 2.1: Example of using RSGs for monitoring masonry structures (Pictures by courtesy of Duvnjak et al. (2016)): (a) Overview of a measuring point; (b) Detail of a measuring point.

It is worth noting, however, that more frequently RSGs are used for determining the mechanical properties of masonry and its components, as reported in Pereira and Lourenço

(2016) and in Derakhshan et al. (2017). Other devices that reached their market maturity during the last decade are the fiber optic (FO) strain sensors, which are capable of allowing affordable instrumentation of large structures since these sensors are sensitive at each point of their length, thus showing a great potential for on-site damage detection and localization (Habel and Krebber 2011; Glisic et al. 2013). Promising applications of distributed FO technology to masonry constructions can be found in the work proposed by Liehr et al. (2009), which presented a FO sensor-integrated textile that can be used for strengthening purposes and strain monitoring device at the same time. Three-points bending tests conducted on two-stone samples demonstrated as the proposed sensor-integrated textile acted as sensor support by enabling direct strain transfer from the monitored structure to the FO sensors, which were capable of detecting cracks of width of 1 mm that developed during the tests. Similarly, in Valvona et al. (2017), FO sensors were embedded within a reinforcement layer suitable for seismic retrofitting intervention on masonry buildings. This advanced FO system was adopted for monitoring an old masonry pavilion vault under environmental conditions, thus highlighting as the optic sensors can be effective even in revealing small deformation in-service conditions. FO devices can be also directly integrated in the mortar joints of existing masonry structural elements (Fig. 2.2), as experienced in the work proposed by Verstrynge et al. (2018). Herein, FO strain sensors were employed for damage detection and localization during the execution of cyclic three-point bending tests performed on a full-scale masonry wall by increasing the intensity of the load applied during the tests. As main result, the paper pointed out that the FO technology is well suited for crack width quantification in masonry structural elements.


(a) (b)

Figure 2.2: Example of using FO sensors for monitoring masonry structures (Pictures by courtesy of Verstrynge et al. (2018)): (a) A fiber optic embedded within a mortar layer; (b) Detail of an anchor point of a fiber optic.

2.3 Monitoring strain with innovative SHM techniques exploiting the smart material concept

The smart material concept, recently developed through advances in the fields of nanotechnologies and materials science, is based on the main idea that selected inclusions, typically nano- or micro-fillers, organic molecules, polymeric and metallic particles, can be combined with traditional construction material to obtain advanced multifunctional composites possessing accurately modulated properties and therefore capable of finding a broad spectrum of employment in the modern engineering (Gandhi and Thompson 1992; García-Macías et al. 2018b; Chen and Akbarzadeh 2020).

Concerning the application of the smart materials to SHM of civil constructions, electrically conductive fillers are usually employed to enhance the piezoresistive capability of the traditional construction materials, such as the cement- or the clay-based ones, hence enabling the production of sensing composites with which, in principle, it is possible to build entire buildings, structural elements/components, or sensors of small sizes to be integrated in the load-bearing structure, capable of self-monitoring their strain state through the assessment of measurable variations in their electrical properties (Han et al. 2011; Rana et al. 2016; Birgin et al. 2020). Such a promising approach was initially adopted for the monitoring of concrete structures by means of the production of sensing construction composites obtained by doping matrices made of cement paste, mortar, or concrete with carbon fillers, such as graphene (GNP), carbon nanofibers (CNF)s, carbon nanotubes (CNT)s, or multiwalled carbon nanotubes (MWCNT)s. These are considered the most suitable electrically conductive inclusions for enhancing the piezoresistive capabilities of cement-based materials (Shah et al. 2009; Coppola et al. 2011; Azhari and Banthia 2012a; Magalhães et al. 2012; Galao et al. 2014; Yang et al. 2020). It is worth noting that the manufacturing of smart concrete composites, along with the electromechanical characterization of their behavior under quasi-static and dynamic loads, and their on-site applications, currently represent an open research field of rising interest (Hilding et al. 2003; Anand and Mahapatra 2009; Loh and Gonzalez 2015; D'Alessandro et al. 2016; García-Macías et al. 2018a). An investigation of the feasibility of using MWCNT cement-based composites for traffic monitoring is reported in Han et al. (2009). Herein, after conducting preliminary experiments to investigate the strain-sensing capability of the smart sensors when strained in compression, a road test was presented, demonstrating how such a typology of sensors embedded within a concrete pavement can be useful for a wide range of applications, such as traffic flow observation, weight-in-motion measurements, and vehicle speed detection.

In Saafi (2009), wireless CNT-reinforced cementitious sensors were firstly produced and characterized by carrying out axial compression tests, then inserted into concrete beams subjected to monotonic and cyclic loading. The obtained experimental results proved that the wireless response of those smart sensors well-revealed the initiation of cracks in the tested concrete beams through a sudden increase in their measured electrical resistance, hence pointing out their effectiveness for on-site early damage detection. The work proposed by Downey et al. (2017a) reported an exhaustive study concerning non-reinforced and reinforced cement paste structural elements made by doping cementitious matrices with MWCNTs. In the paper, a resistor mesh model was developed with the aim of detecting and locating damages that occurred to the smart structural elements by means of the post-processing of their electrical outputs. Testing the produced doped elements under uncontrolled and controlled damage states, the Authors demonstrated the effectiveness of the smart structural elements in self-monitoring their strain states, allowing also the detection and localization of suffered damages by means of the use of the proposed resistor mesh model to evaluate the permanent local changes that occurred in their electrical properties due to the developing cracks. Smart structural components were tested also in the work carried out by Ding et al. (2019), in which cementitious prismatic sensors, doped with a composite filler made of CNT and nano carbon black, were employed for monitoring the strain field in concrete columns under axial compression loads. In the paper, the response of the proposed strain-sensing sensors was evaluated before and after their embedding within the columns. The obtained results demonstrated that the proposed sensors were able to reveal changes in strain within the monitored structural elements, highlighting their effectiveness for the monitoring of prefabricated concrete components.

Considering the results achieved by applying the smart material concept to SHM of concrete structures, nowadays, this innovative technology was extended to the clay-based construction materials to embed smart monitoring capabilities in traditional masonry constructions. In Ubertini et al. (2017a), the Authors reported for the first time the development of fired clay bricks called “smart bricks”, representing a novel class of durable smart sensors for monitoring the strain field in masonry constructions, whose piezoresistive capabilities were improved through the addition of MWCNTs to the fresh clay matrix, hence by slightly modifying the production process of the conventional clay bricks. The work addressed the optimization of the manufacturing process of such innovative smart bricks, dealing with a study on the stability of different carbon fillers at high temperatures. Tests under compression loads were also carried out on the proposed clay-based sensors, instrumented with Kanthal wire electrodes, to investigate their strain-sensing capabilities. The obtained results pointed out that bricks doped with MWCNTs possessed an enhanced sensitivity to the applied strain compared to that of plain bricks, therefore highlighting their possible employment for SHM purposes. In Downey et al. (2017b), the Authors introduced a new formulation of smart bricks produced by using titanium dioxide particles to dope the fresh clay matrix. The work first illustrated the characterization of the strain-sensing behavior of the novel sensors according to the amount of filler used for their production, then introduced a first experimental application of the smart brick technology for monitoring strain variations in a medium-scale wall specimen subjected to eccentric axial compression loads. The obtained results demonstrated that smart bricks were capable of monitoring changes in the strain field of the masonry wall, promoting their use also for cracks detection. A theoretical investigation on the effectiveness of the smart bricks for the post-earthquake assessment of masonry constructions was discussed in García-Macías and Ubertini 2019. The paper addressed the numerical simulation of two case studies, including a masonry shear wall and a masonry building subjected to seismic loading, both instrumented envisioning a monitoring system involving smart bricks. In particular, the latter numerical test emphasized the usefulness of spatial interpolation approaches for the reconstruction of the maps of the relative variation in electrical resistance by means of the post-processing of the electrical outputs from the novel sensors. Indeed, the assessment of anomalies in the mapped trend of the electrical measurements from smart bricks permitted to reveal damages developed to the mechanical model of the masonry building, putting in evidence the theoretical potentiality of this new sensing technology for monitoring masonry constructions under earthquake loading. A further application of the smart material concept to clay-based materials was recently introduced in Wang et al. (2020). In this case, the Authors turned out conventional clay bricks into supercapacitors by using chemical vapors that reacting with the red iron oxides contained in the internal macro-porous structure of the bricks, formed an electrically conductive network of nanofibers. The paper reported a comprehensive investigation of the electrical properties of this formulation of smart bricks, describing in detail its innovative production process. Such a modified brick is therefore able to store charge, with possible employment in the field of civil constructions as power supply, sensing device, and more.

2.4 Closing remarks

This chapter presented an overview of the state-of-the-art of strain-based SHM techniques commonly applied to masonry constructions. In particular, both traditional strategies, in which off-the-shelf sensing technologies are employed, and innovative approaches, based on the smart material concept, were framed. The advantages of using strain measurements instead of dynamic parameters were also discussed.

RSGs and FO sensors are the maturest and reliable tools for monitoring the health state of either new or existing masonry constructions, permitting the tracking of the changes in their strain field induced by developing damages. In order to fulfill this task, the aforementioned sensors should be installed directly on the portion of the building affected by the damage or deployed within dense sensor networks, otherwise, a reliable identification and localization of the damages can be challenging (Glisic and Inaudi 2008; Glisic and Verma 2011; Bao and Chen 2012). In light of that, it is worth considering that historical masonry constructions such as churches, towers, and palaces, are commonly subjected to strict aesthetic and architectural limitations that make difficult the installation of SHM systems involving a large number of sensing devices, to the detriment of the completeness of the information obtainable concerning their structural response. Even when the deployment of large sensor networks is permitted, it should be taken into account that measurements provided by RSGs and FO sensors only partially allow to appreciate the actual structural response of the monitored structures, inasmuch as these devices are externally attached to the outer surfaces of the constructions, hence less sensitive to the internal stress/strain redistributions induced by the development of damages, and possess physical and mechanical properties that are very far from those of the conventional masonry, which is a heterogeneous material of high complexity especially in the case of ancient structures. Therefore, it appears obvious that the listed drawbacks limit the large scale deployment of continuous SHM systems to masonry constructions, despite their benefits are clear.

Considering this framework, the development of new sensing technologies capable of overcoming the actual limiting factors shown by the off-the-shelf devices appears as an urgent priority for promoting the implementation of monitoring systems to masonry constructions, which clearly demand more practical and scalable sensing devices to be largely employed. Innovative solutions were proposed in the literature to overcome the listed limiting aspects (Rathod and Jain 2018; Yeo et al. 2020). Among all, this work focused the attention on the concept of smart material since it represents a powerful resource for integrated strain-based SHM systems, as also demonstrated by the experimental applications of the nanomodified cement-based sensors previously introduced. On the other hand, the analysis of the state-of-the-art also highlighted that the use of smart sensors for monitoring strain in masonry constructions is feasible and promising, but is currently at a very early stage of development.

Along these lines, this work recognizes the use of the smart material concept in monitoring applications as a rising and effective alternative to the traditional SHM techniques commonly applied to masonry constructions. Therefore, further developments in the smart brick technology are proposed in the next chapters with the main objective of comprehensively designing and characterizing a reliable smart sensing device suitable for seismic SHM of masonry constructions, also demonstrating its employment for meaningful tasks, such as the reconstruction of the strain field in the monitored structures and the detection and localization of damages with particular attention to the earthquake-induced ones.

Chapter 3

Computational modeling of masonry structures

3.1 Introduction

Masonry is a composite material consisting of bricks and mortar layers arranged according to a plus-minus engineered bond pattern. Its intrinsic heterogeneity, particularly marked in the case of ancient constructions, results in complex mechanical behavior, with anisotropy in both the linear and nonlinear range, which demands advanced mechanical models, often discretized by means of the FE method, to be accurately replicated (Sacco et al. 2018). During the last half-century, the scientific community leveraged consistently the computational analysis of masonry constructions by developing tools for predicting their structural response. These are nowadays satisfactorily employed to investigate the mechanical behavior of new buildings, e.g., for the optimization of their design (López-Almansa et al. 2010), as well as to interpret the in-service structural response of existing constructions and for the assessment of their near-collapse behavior, thus aiding the determination of their operational conditions, their safety, or the design of strengthening and retrofitting interventions (Valente and Milani 2016). Mechanical models are also frequently adopted in synergy with seismic SHM systems seeking for anomalies in the response of the monitored structures (Ivorra and Pallarés 2006; Clementi et al. 2017; Compán et al. 2017; Angjeliu et al. 2020).

With the aim of providing a clear comprehension of the methodologies pursued in this work to build, discretize, and analyze the mechanical models later introduced, this chapter reports an overview on the modeling strategies commonly employed when dealing with masonry, also presenting the computational tools adopted for analyzing masonry constructions in the case studies proposed in Chapter 5. Accordingly, the rest of the chapter is organized as follows. Section 3.2 proposes a literature review on the modeling strategies for masonry, while Section 3.3 introduces the computational tools utilized in this work. In particular, the constitutive model employed for the numerical simulation of the nonlinear mechanical behavior of the masonry and its components is described in detail. Section 3.4 concludes the chapter with comments and remarks.

3.2 Modeling strategies for masonry

Modeling strategies for masonry are generally classified in micromodeling and macromodeling approaches based on the scale at which the masonry is analyzed. The choice of a computational method rather than another largely depends on the masonry construction typology, the specific masonry behavior, and the level of accuracy demanded in the numerical outputs (Lourenco 1996; Addessi et al. 2014; D'Altri et al. 2019). Micromodeling approaches allow the adoption of different constitutive laws for each component of the masonry, i.e. bricks and mortar layers, as well as the detailed modeling of the brick-mortar interaction, thus including the reproduction of slips and detachments between the components. Generally, in a detailed micromodel, bricks units and mortar layers are discretized by using continuum elements characterized by linear or nonlinear mechanical behavior, while interface elements or contact interactions can be employed to simulate the bonding between the masonry components (Fig. 3.1(b)).

The mechanical properties involved in the constitutive laws should be determined by testing each masonry component. In Sacco and Toti (2010) a detailed micromodel was proposed to reproduce the mechanical behavior of masonry arches under axial compression loads, for which experimental results were available. In this case, bricks and mortar layers composing the structural elements were modeled with a linear mechanical behavior, while interface elements, characterized by an interface cohesive model combining damage and friction, were adopted to numerically reproduce the brick-mortar interaction. The obtained results

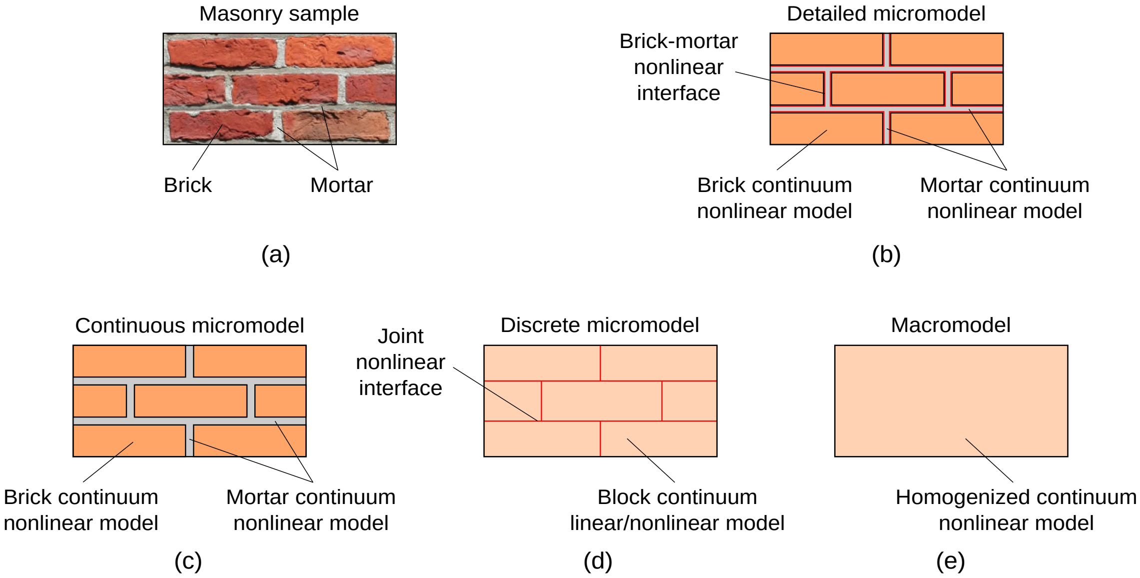

Figure 3.1: Illustration of the modeling strategies for masonry: (a) Sample of masonry; (b) Detailed micromechanical model; (c) Continuous micromechanical model; (d) Discrete micromechanical model; (e) Macromechanical model.

proved the effectiveness of the adopted modeling strategy and of the constitutive laws proposed for modeling the brick-mortar interaction since a good agreement between the obtained numerical and experimental outputs was found. As exemplified in Sacco and Toti (2010), such micromodeling approaches are usually preferred in case of mechanical models representing structural elements or portions of constructions, such as façades, pier panels, vaults, and arches since they ensure a high level of accuracy, as well as the numerical simulation of the main failure mechanism that can occur to the masonry components and the brick-mortar interfaces, at the expense of high computational costs. In light of that, detailed micromodeling approaches can be simplified by neglecting the modeling of the brick-mortar interfaces (Fig. 3.1(c)). In Petracca et al. (2017) a continuous micromodel, in which both brick units and mortar layers were modeled by using 2D plane-stress continuum elements with nonlinear mechanical behavior, was proposed for the analysis of masonry walls under shear stress states and benchmarked with other two micromodels based on the use of brick-mortar interfaces. Experimental results were exploited for the validation of the numerical simulations, proving that all the investigated modeling strategies were equally capable of describing the behavior of the tested structural elements up to their failure. Furthermore, the obtained results highlighted the reduction in computational costs achieved with the use of the continuous micromodel at the expense of a lower accuracy reached in the estimation of the shear strength with respect to the other considered modeling strategies. Alternatively, discrete micromodels represent a further simplification of the strategies involving brick-mortar interfaces. According to this methodology, expanded blocks are modeled by continuous elements characterized with a linear or nonlinear mechanical behavior, while mortar layers are lumped in joint nonlinear interfaces reproducing the brick-mortar interaction (Fig. 3.1(d)). It is worth noting that the equivalent mechanical properties of the expanded blocks are determined by considering the original masonry assemblage, hence employing homogenization techniques that allow the computation of the mechanical parameters of the equivalent masonry by taking into account the mechanical properties of bricks and mortar layers (Cluni and Gusella 2004; Ridwan et al. 2017). An interesting example concerning the adoption of a continuous micromodel for numerically simulating the behavior of a masonry wall subjected to vertical and horizontal loads is reported in Abdulla et al. (2017). Here, expanded blocks were characterized with a plasticity model capable of reproducing the compressive nonlinear behavior of the masonry, hence a contact interaction, able to take into account the cohesive behavior and the damage in tension, was proposed to numerically reproduce the brick-mortar interfaces. A masonry wall specimen was experimentally tested in both in-plane and out-of-plane conditions, then the mechanical model was used to replicate the experiment. The obtained results proved the effectiveness of the proposed continuous micromodel, whose numerical outputs were in satisfactory agreement with the data experimentally acquired by testing the wall specimen and used as benchmark for the validation of the proposed modeling strategy. Concerning the numerical reproduction of large masonry constructions, such as towers and palaces, the use of macromechanical models is widely recognized by researches and engineers as the most suited modeling technique since, in this case, the use of a micromodel would result in heavy computational costs due to the geometrical dimensions of the structure being modeled and to its numerous building details. Macromechanical models smear out bricks, mortar layers, and brick-mortar interactions in a continuum element that can be characterized either with a linear or nonlinear mechanical behavior to numerically simulate the global structural response of the masonry instead of that of its single components. This results in a compromise between accuracy and computational efficiency (Fig. 3.1(e)). Typically, homogenization techniques are adopted to determine the equivalent mechanical parameters of the continuum element. In some cases, the stress-strain relationships taken into account for the structural analysis are directly derived by testing structural settings of sufficiently large sizes under homogeneous states of stress. As a general rule, the accuracy of a macromodel is strongly related to the definition of its constitutive laws and its equivalent mechanical properties. Macromodels can be however employed also for the reproduction of masonry structural elements of small sizes, as demonstrated in Wu and Hao (2006). In this paper, the Authors first derived the equivalent elastic properties, strength envelope, and failure characteristics of the masonry material by considering a 3D masonry basic cell, a selected homogenization technique, and FE analyses; then, the obtained homogenized 3D model was utilized to simulate the response of a masonry wall to airblast loads. Numerical analyses were also carried out with a continuous micromodel. The comparison between these two different modeling strategies demonstrated that the macromodel was able to reproduce the global behavior of the wall under blast loading achieving a more than acceptable accuracy and with a convenient computational efficiency.

3.3 Computational tools and Finite Element Analysis

From a mechanical point of view, masonry is a very complex material. Its mechanical response is strongly affected by the arrangement, in a certain pattern, of bricks and mortar, which are characterized by a quasi-brittle behavior both in tension and compression. The brick-mortar interfaces are known to represent planes of weakness due to the coupling of different materials, and therefore are often the preferred path for the development of cracks due to slips and detachments between the components. Globally, masonry possesses higher values of strength in compression rather than in tension, nevertheless, all its mechanical characteristics, such as the elastic modulus and the fracture energy, suffer from a marked anisotropy. In this work, the Concrete Damaged Plasticity (CDP) model was adopted for the reproduction of the nonlinear mechanical behavior of the masonry and its components (Lubliner et al. 1989; Lee and Fenves 1998; Cińcio and Wawrzynek 2005). The constitutive model is available in Abaqus, a commercial FE analysis software (Hibbett et al. 1998) used in this work for modeling and analyzing mechanical models and also for the visualization of the results obtained from the numerical simulations.

The CDP model is a plastic-damage model, nowadays widely used for reproducing the nonlinear behavior of the masonry in macromechanical modeling approaches (Valente and Milani 2019b; Libecajtová 2020), which allows taking into account different yield strengths in tension and compression, as well as the softening behavior in tension as opposed to initial hardening followed by softening in compression. The constitutive model can be also employed to simulate damages to the masonry, considering different degradation of the elastic stiffness in tension and compression, and the stiffness recovery effects during cyclic loading. It is worth noting that the CDP model assumes that the elastic stiffness degradation is isotropic, i.e. stiffness moduli corresponding to different directions decrease proportionally and independently of the direction of loading. Owning such features, this constitutive model is also suited for the simulation of the mechanical behavior of bricks and mortar in more refined modeling approaches, such as the micromechanical ones (D'Altri et al. 2018). Fig. 3.2(a) exemplifies the uniaxial response in tension and compression of the material according to the CDP model.

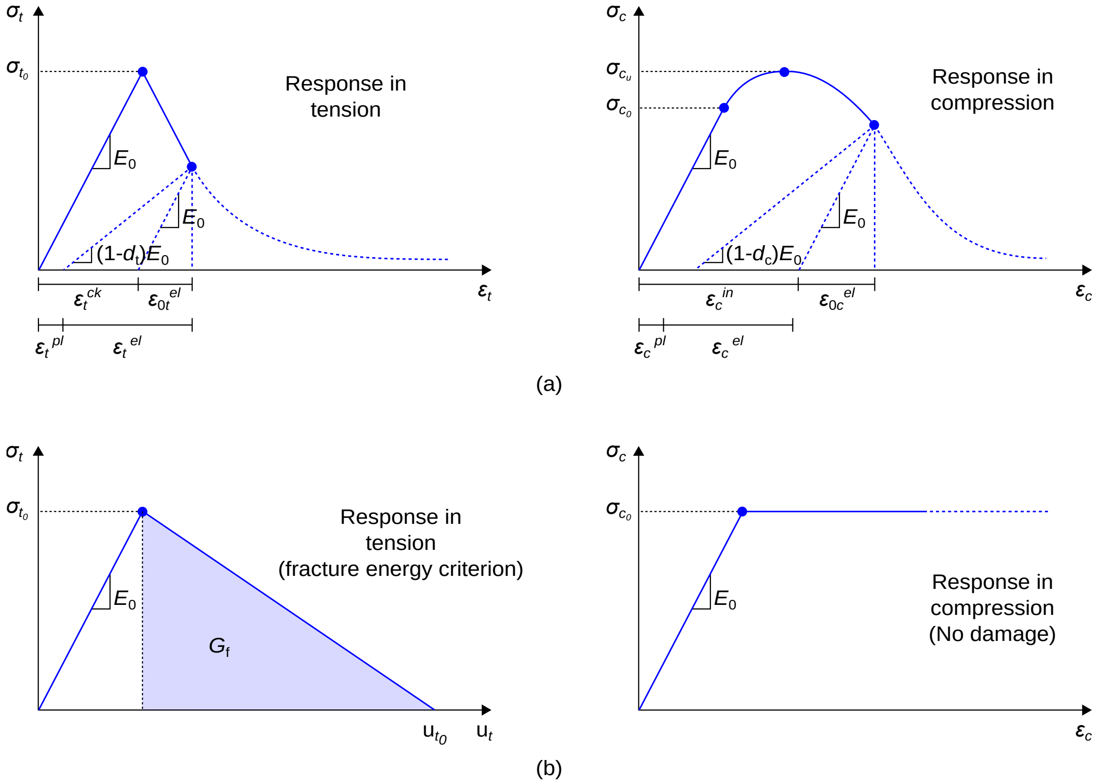

Figure 3.2: Illustration of the uniaxial response in tension and compression of masonry according to the Concrete Damaged Plasticity model: (a) Theoretical responses provided by the constitutive model; (b) Responses adopted in this work.

Under tension, the stress-strain response is linear up to the failure stress, σ_{t0}, which corresponds to the crack initiation in the material. The propagation of cracks results in the softening stress-strain response branch. Under compression, the stress-strain response is linear up to the yield stress, σ_{c0}, then there is a hardening branch until reaching the ultimate stress, σ_{cu}, which is followed by a softening stress-strain response branch. The unloading of a damaged material results in a response characterized by a reduced elastic stiffness equal to $(1-d_t)E_0$ or $(1-d_c)E_0$ in tension and compression, respectively, where d_t is the scalar damage variable in tension (DAMAGET), d_c is that in compression (DAMAGEC), and E_0 is the elastic modulus of the undamaged material. The value of the scalar damage parameters theoretically ranges from 0, indicating an undamaged material, to 1, representing a fully damaged material. In practical applications, it is however set less than 1 avoiding convergence issues during the FE analyses. According to the considered constitutive model, σ_{t0} and σ_{c0} can be expressed as follows:

$$\sigma_{t0} = (1 - d_t)E_0(\epsilon_t - \epsilon_t^{pl}), \tag{3.1}$$

$$\sigma_{c0} = (1 - d_c)E_0(\epsilon_c - \epsilon_c^{pl}), \tag{3.2}$$

where ϵ_t and ϵ_c are the total strain in tension and compression, while ϵ_t^{pl} and ϵ_c^{pl} are the equivalent plastic strain in tension and compression, respectively. In order to avoid mesh sensitivity in the results from the FE simulations, i.e. for reducing the dependence of the numerical solution from the discretization of the geometry of the problem, the fracture energy criterion, proposed by Hillerborg et al. (1976), was considered in this work to model the elastic stiffness degradation specifying cracking relative displacements (cracks openings), u_{ck}, instead of cracking strains, ϵ_t^{ck}. Accordingly, the post-failure behavior in tension of the material is specified by considering a linear isotropic degradation of its elastic stiffness, adopting $u_{t0} = 2G_f/\sigma_{t0}$ for the computation of the cracking displacement at which complete loss of strength takes place, u_{t0} (see Fig. 3.2(b)). In this relation, G_f, represents the value of the fracture energy of the material. The "plastic" displacement in tension, u_t^{pl}, is automatically computed by Abaqus as follows:

$$u_t^{pl} = u_t^{ck} - \frac{d_t}{(1 - d_t)} \frac{\sigma_t l_0}{E_0}, \tag{3.3}$$

where l_0 is the characteristic length. This is based on the element geometry and formulation, e.g., it is a typical length of a line across an element used to discretize the geometry in case of first-order elements. Fig. 3.2(b)) also shows that a simplified response in compression was considered in this work with respect to the standard formulation of the constitutive model. In particular, the CDP model was set with a $d_c = 0$, meaning that no damage in compression is taken into account. Therefore, in this particular case, $\epsilon_c^{pl} = \epsilon_c^{in}$, being ϵ_c^{pl} the plastic strain and ϵ_c^{in} the inelastic component (see Fig. 3.2(b)). It is worth noting that this assumption was made since no damage in compression was detected to the structures tested in Chapter 5. Generally, the reduction in the elastic stiffness due to damages developed in the material under uniaxial tension and compression is expressed as follows:

$$E = (1 - d)E_0, \tag{3.4}$$

where d is a scalar degradation variable (SDEG) function of d_t and d_c:

$$(1 - d) = (1 - s_t d_c)(1 - s_c d_t), \tag{3.5}$$

It should be noted that s_t and s_c are dependent on the stress state and their use is necessary to introduce the stiffness recovery effect in the CDP model. As default setting, the constitutive model recovers the compressive stiffness upon a crack closure as the load reverses from tensile to compressive state, while the tensile stiffness is not recovered as the load changes from compressive to tensile state once the material is crushed. This is the typical behavior of a quasi-brittle material under cyclic loading conditions, therefore it well represents the mechanical behavior of the masonry, as well as that of its components. The variables s_t and s_c are defined as follows:

$$s_t = 1 - w_t H(\sigma_{11}), \tag{3.6}$$

$$s_c = 1 - w_c(1 - H(\sigma_{11})), \tag{3.7}$$

where w_t and w_c represent the weight factors that control the recovery of the tensile and compressive stiffness, while $H(\sigma_{11})$ is the Heaviside function that is assumed equal to 1 if $\sigma_{11}>$ 0 (tension) and equal to 0 of $\sigma_{11}<$ 0 (compression). The default behavior of the CDP model is obtained by setting $w_t = 0$ and $w_c = 1$, considering that 0 means no stiffness recovery, while a value equal to 1 indicates the total stiffness recovery. In light of that, and considering the settings adopted in this work to describe the damage in tension and compression, the reduction in the elastic stiffness was computed through a simplified relationship as reported as follows:

$$E = (1 - s_c d_t)E_0, \tag{3.8}$$

A Drucker-Prager strength criterion, modified by means of the parameter K_c, is used in the CDP model. The parameter K_c is the ratio between the second stress invariant on the tensile meridian and the one on the compressive meridian. This is introduced in the model to modify the shape of the yield function in the deviatoric plane. As specified in the users guide Simulia (*ABAQUS/Analysis User's and Theory Manual*), a $K_c < 1$ ensures a yield surface of a shape similar to a triangle with curved sides as much as K_c moves away from the value of 1. This is necessary to obtain a yield surface approximating the Mohr-Coulomb criterion in the deviatoric plane. The nonassociated flow law assumed in the CDP model is expressed through the following relationship:

$$\dot{\vec{\epsilon}}^{pl} = \dot{\lambda}\frac{\partial \mathrm{G}(\vec{\sigma})}{\partial \vec{\sigma}}, \tag{3.9}$$

where $\dot{\vec{\epsilon}}^{pl}$ and $\vec{\sigma}$ are the plastic strain rate vector and the stress vector, respectively. The flow potential G used for this constitutive model is the Drucker-Prager hyperbolic function, which can be expressed as:

$$\mathrm{G} = \sqrt{(e\sigma_{t0}\tan\psi)^2 + \bar{q}^2} - \bar{p}\tan\psi, \tag{3.10}$$

where ψ is the dilatation angle measured in the $\bar{p}-\bar{q}$ plane at high confining pressure, σ_{t0} is the uniaxial tensile stress at failure taken from the user-specified tension stiffening data, and e is the eccentricity that defines the rate at which the function approaches the asymptote (the flow potential tends to a straight line as the eccentricity tends to zero). It should be noted that ψ allows controlling the dilatancy behavior of the material. In particular, the dilatancy increases as the value of ψ increases, however, the use of relatively high values of this angle may cause too optimistic results for stiffness and bearing capacity of the material ("Calibration of the CDP model parameters in Abaqus"). Constitutive models describing the softening behavior and stiffness degradation of materials can be affected by severe convergence issues when employed in implicit FE analysis. The introduction of viscoplastic regularization of the constitutive equations is a widely adopted solution to overcome such numerical problems in practical applications (Valente and Milani 2019a). The CDP model can be therefore regularized by introducing a viscosity parameter, μ, in its formulation, thus aiding the convergence rate in the softening branch. Small values of this viscosity parameter should be adopted to avoid compromising the outputs from the FE simulations. If the viscosity parameter is greater than zero, the outputs of the plastic strain and stiffness degradation refer to:

$$\dot{\epsilon}_v^{pl} = \frac{1}{\mu}(\epsilon^{pl} - \epsilon_v^{pl}), \tag{3.11}$$

$$\dot{d}_v = \frac{1}{\mu}(d - d_v), \tag{3.12}$$

where $\dot{\epsilon}_v^{pl}$ is the viscoplastic strain rate, ϵ^{pl} is the plastic strain component, and $\dot{d}_v$ is the viscous stiffness degradation variable. The stress-strain relationship, in the case of the viscoplastic formulation of the CDP model, is expressed as follows:

$$\sigma = (1 - d_v)E_0(\epsilon - \epsilon_v^{pl}), \tag{3.13}$$

Further information concerning the implementation of the CDP model in the mechanical models developed in this work, such ad the value of the parameters of the constitutive laws of the model and the mechanical properties of the materials, set case-by-case, are reported in Chapter 5. The Abaqus implicit solver was adopted to run the FE simulations by using 12 cores of a 2.60 GHz dual Intel Xeon Gold 6126 node mounted on a Beowulf cluster.

3.4 Closing remarks

This chapter dealt with the computational modeling of masonry with the purpose of supporting the mechanical models and FE analyses considered in this work.

A literature review on the existing modeling strategies for masonry constructions was reported, mainly focusing the attention on the scale at which the masonry is analyzed. Micromechanical approaches allow the representation of brick units and mortar layers separately, plus the definition of their interaction. These strategies are particularly effective when the main aspect of the modeling is the investigation of the local distributions of stresses/strains and damages. Their use is therefore recommended for the simulation of the structural response of small size elements since their employment for the modeling of large constructions would demand unsustainable computational costs. To address this issue, simplified variants of the detailed micromodels can be considered, such as the continuous and discrete micromodels. Macromechanical approaches can be invoked in case of large constructions, with the limiting aspect that only their global structural response, along with the development of damages, can be investigated. These strategies neglect the individual discretization of the components of the masonry by taking into account an equivalent masonry material whose mechanical behavior is described through suited constitutive laws and by using equivalent mechanical properties derived from the homogenization of those of the single components. The reduction in computational costs is certainly marked. It is worth noting that independently of the modeling strategies adopted, reliable and effective mechanical models can only be defined if a complete material description is available. Overall, the choice of the most suitable modeling strategy should be weighted according to the complexity of the construction under investigation, the outputs required, and the data available.

Another relevant aspect to be taken into account in the computational modeling of masonry is its nonlinear mechanical behavior, which is characterized by a quasi-brittle response under both tension and compression, even if for this latter, the ultimate strength is much higher. This discrepancy is particularly marked in the case of ancient constructions. In this work, the CDP model, implemented in the commercial software for FE analysis, Abaqus, is considered to represent the structural response of the masonry and its components in tension and compression and for the simulation of the damages suffered in tension by considering an isotropic linear degradation of their elastic stiffness. A further key feature of the CDP model, which can be particularly useful when dealing with the investigation of masonry construction subjected to seismic loading and which therefore was exploited in this work, is represented by the possibility to simulate the closure of cracks under cyclic loading conditions by means of the recovery in the elastic stiffness when the load changes from tension to compression states. The CDP model was fully described in this chapter including these characteristics.

Chapter 4

A new sensing technology for SHM of masonry structures: The smart brick

4.1 Introduction

Continuous SHM systems allow the assessment of the structural performances/integrity of masonry constructions by means of the tracking of a broad range of engineered features, such as modal parameters, tilts, and displacements, in a real-time approach. Nevertheless, the development of cracking patterns in masonry structural elements leads to the onset of anomalies in their strain field that make particularly effective SHM techniques based on strain measurements for damage detection and localization. Despite their reliability in measuring strain, off-the-shelf sensing technologies are affected by practical drawbacks, in particular by scalability and deployment issues, which nowadays are limiting the large scale implementation of such traditional sensing devices for SHM of masonry constructions.

From that perspective and considering the literature review presented in Chapter 2, this chapter introduces novelties concerning the development of the smart brick technology, an innovative SHM solution recently proposed for monitoring strain in masonry structures allowing the overcoming of the main limiting aspects experienced by using traditional sensing devices since it is based on the employment of piezoresistive brick-like sensors, called "smart bricks", fully integrable within the load-bearing structures. The organization of the rest of the chapter is hereinafter reported. Section 4.2 illustrates in detail the smart brick technology describing the novelties introduced by this work in the production process of the novel sensors, the methodology utilized for conducting electrical measurements, and their strain-sensing principle based on an innovative electromechanical model herein proposed. Section 4.3 presents the methodologies adopted for testing the electrical, electromechanical, physical, and mechanical properties of the smart bricks. Methods for conducting a study on the influence of the environmental effects on the electrical outputs of the novel sensors are also outlined. Section 4.4 collects results achieved in the performed investigations, while Section 4.5 closes this chapter reporting final comments and remarks.

4.2 The smart brick technology

Smart bricks are a new sensing technology for seismic SHM of masonry structures based on strain measurements, consisting of piezoresistive brick-like sensors that can be embedded within the load-bearing structure to monitor permanent changes in the strain field. Based on their piezoresistive behavior, enhanced through the addition of suitable nano- or micro-fillers to fresh clay matrices during the production process of the conventional clay bricks, an increase in the compression load applied on a smart brick leads to an increment in its compressive strain state and a measurable reduction in its electrical resistance, with respect to the initial condition, resulting in the strain-sensing capabilities of the novel sensor, as exemplified in Fig. 4.1(a). Smart bricks can be therefore placed at specific locations of a masonry construction, even in portions of its load-bearing structure not inspectable after the completion of the building phase, to monitor the strain gradient induced by damages due to earthquake loading. In particular, according to their deployment in the structure being monitored, smart bricks can reveal the initiation of global collapse mechanisms, as well as the occurrence of local failures like overturnings and mechanisms based on the arch effect, since all of these results in redistributions in dead loads which the novel sensors can detect as changes in their electrical outputs (4.1(b)). It should be noted that, following this sensing principle, smart bricks can also aid the detection and localization of damages due to a broader range of structural pathologies that typically affect masonry buildings during their service life, such as damages due to excessive stresses/strains, or that induced by differential foundation settlements.

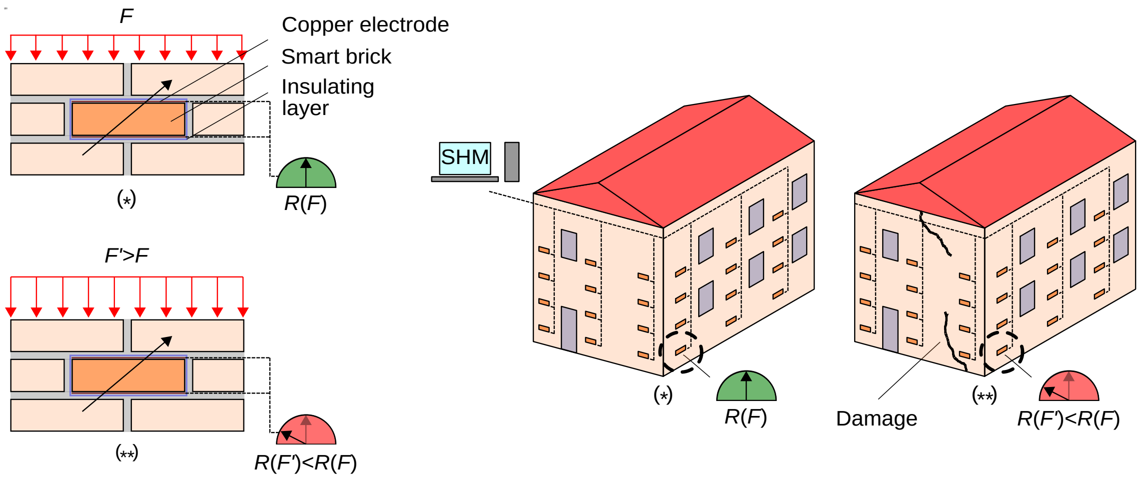

(a)

Fig. 4.1: Simplified illustration of the smart brick technology: (a) Exemplification of the strain-sensing behavior of a smart brick (R is the electrical resistance of the smart brick); (b) Exemplification of the use of the smart bricks for monitoring a masonry building with highlighted the changes in the electrical resistance of a sensor due to the redistribution of the internal load paths induced by the development of damages to the structure.

4.2.1 Production process

The production process of the conventional clay bricks consists of four main phases where the clay is first mined, then molded, dried, and finally fired. The burning phase, during which a temperature between 900 and 1200°C is commonly reached, can be considered the most important part of the entire process, where clay loses plastic properties by developing mechanical strength. Although the literature review proposed in Section 2.3 indicates the carbon-based fillers as the best electrically conductive inclusions to enhance the piezoresistive capabilities in cement-based composites, it should be taken into account that such particles possess a low heat resistance, hence they may be not so suited for the production of smart bricks and the improvements of their sensing capabilities, contrary to the expectations. To deepen this aspect, a thermogravimetric analysis (TGA) was carried out by subjecting to thermal cycles up to 900°C small amounts of carbon-based fillers commonly used for the production of cement-based composites, such as CNFs, MWCNTs, and GNP, to assess their heat resistance by comparing their weights before and after the heating. An analytical balance, model Sartorius, with reading accuracy of 0.01 mg, was employed for the weighing. Fig. 4.2 reports the residual weight percentages computed for each carbon-based filler, by showing that all tested inclusions were characterized by a marked weakness with respect to the investigated high temperature. Therefore, even by considering that when carbon-based fillers are embedded within the clay matrices their resistance to elevated temperature might increase, it can be challenging to accurately determine the amounts of filler still present inside the bricks after firing. The obtained results definitely proved that carbon-based fillers are not the most suitable inclusions for the production of smart bricks.

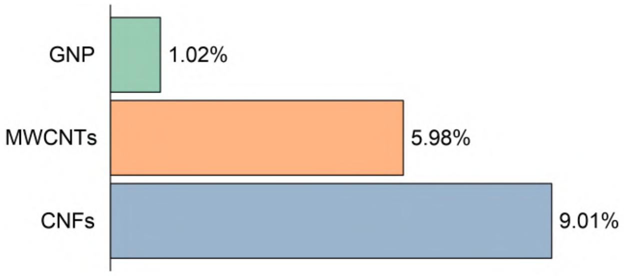

Fig. 4.2: Residual weight percentages computed for the investigated carbon-based fillers after heating to 900°C.

In light of that, while seeking for improvements in the formulation of the smart bricks, this work proposes, as a novelty, the use of stainless steel microfibers as electrically conductive filler for the production of the novel sensors. In particular, steel fibers, model R.STAT/s, with a diameter of 12 μm, length of 5 mm, made with a special alloy, AISI 316L (Fe 68%, Cr18%, Ni 12%, and Mo 2%), were employed. These are characterized by a low electrical resistivity, of the order of 60–80 Ω/cm, as well as by high resistance to the elevated temperature, even over 1000°C, as demonstrated by carrying out a TGA, whose results are reported in Fig. 4.3. A small amount of steel fibers were subjected to thermal cycles performed by increasing the temperature up to 900°C (Fig. 4.3(a)). The weight of the fibers and their electrical resistance were measured before and after each thermal cycle, by using an analytical balance, model Sartorius, and a high-speed digital multimeter, model NI PXI-4071, respectively. The obtained results show that the investigated physical and electrical properties of the steel fibers were unaffected by the heating, thus demonstrating that the considered metallic filler can be used to produce the novel sensors (Fig. 4.3(b, c)). Fig. 4.4 shows Scanning Electron Microscope (SEM) micrographs of the steel fibers for the inspection of their morphology and dispersion within the clay matrices.
The production process of the smart bricks employed in this work is illustrated in Fig. 4.5.

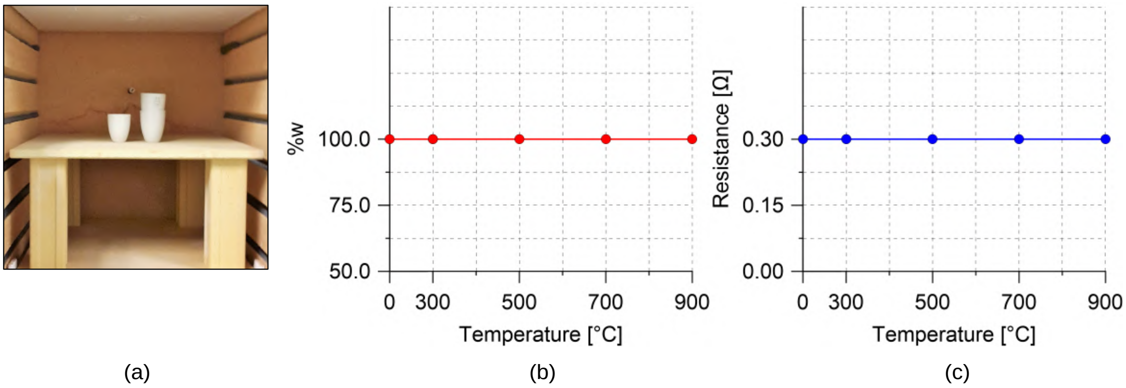

Fig. 4.3: Results from TGA carried out on a sample of stainless steel microfibers: (a) Adopted experimental setup; (b) Residual weight of the sample of fibers at the investigated temperatures; (c) Electrical resistance of the sample of fibers at the investigated temperatures.

Firstly, fresh clay, mined from a quarry located in Central Italy (cfr. Acknowledgements), was mechanically mixed with the desired amount of steel fibers, defined as a fraction of the weight of the prepared fresh clay (Fig. 4.5(a)). Such a procedure permitted to obtain the composite material shown in Fig. 4.5(b). Secondly, brick samples were formed by pouring doped clay in wet wooden molds sprinkled with sand, thus obtaining samples of prismatic shape of 70x50x50 mm^3. At this step of the production, some wet bricks were instrumented with four Kanthal wire electrodes, of diameter of 2.2 mm, embedded symmetrically within the top horizontal side of the bricks, to perform electrical measurements as described in Ubertini et al. (2017a) (Fig. 4.5(c1)), while the others were simply prepared for the next step (Fig. 4.5(c2)) since the electrodes were mounted only after the burning phase. Wet bricks were first dried in an oven at a temperature of 90°C for six hours and then fired at 900°C for additional six hours (Fig. 4.5(d)). After the burning phase, bricks previously instrumented with the embedded wire electrodes were ready-to-use (Fig. 4.5(e1)). Non-instrumented samples were instead equipped with two external copper plate electrodes, of thickness of 50 μm, placed on their opposite horizontal sides with a dry contact, whose employment represents a further novelty proposed by this work (Fig. 4.5(e2)). Sensors with external electrodes were further covered with an insulating polymeric tape to avoid current flow propagation when smart bricks are embedded within masonry structural elements. It is worth noting that some un-instrumented burned bricks were equipped with conductive resin stripe electrodes to measure their internal electrical conductivity with a negligible contact resistance, a procedure that otherwise would not be possible by means of the use of either inner wire or external plate electrodes (Fig. 4.5(e3)). In this case, conductive

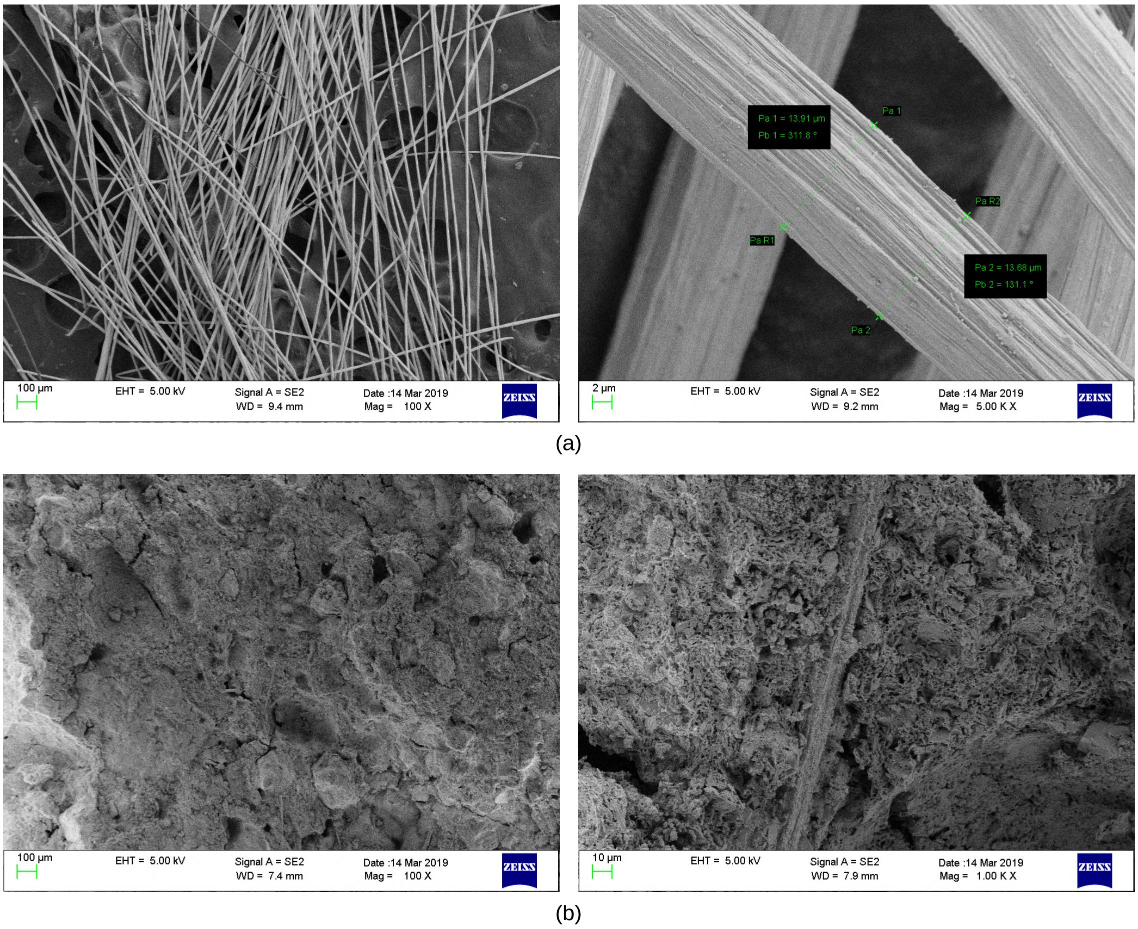

Fig. 4.4: SEM micrographs of the stainless steel microfibers: (a) Inspection of the morphology of the metallic filler; (b) Inspection of the dispersion of the metallic filler within a clay matrix.

resin stripes were produced by mixing graphite powder with a two-component clear epoxy commercial adhesive, named Araldite 2020, in the percentage of 75% in weight of the utilized adhesive and were made by directly spreading the conductive mixture on the middle of the vertical sides of each sample, hence forming conductive electrodes of thickness of 1 mm and width of 10 mm (Cacciotti et al. 2018). At this early stage of development, conductive resin stripe electrodes were only used to conduct electrical measurements in laboratory conditions since their employment for strain-sensing purposes requires further investigations and raises some concerns about the long-term durability of their bonding with bricks.

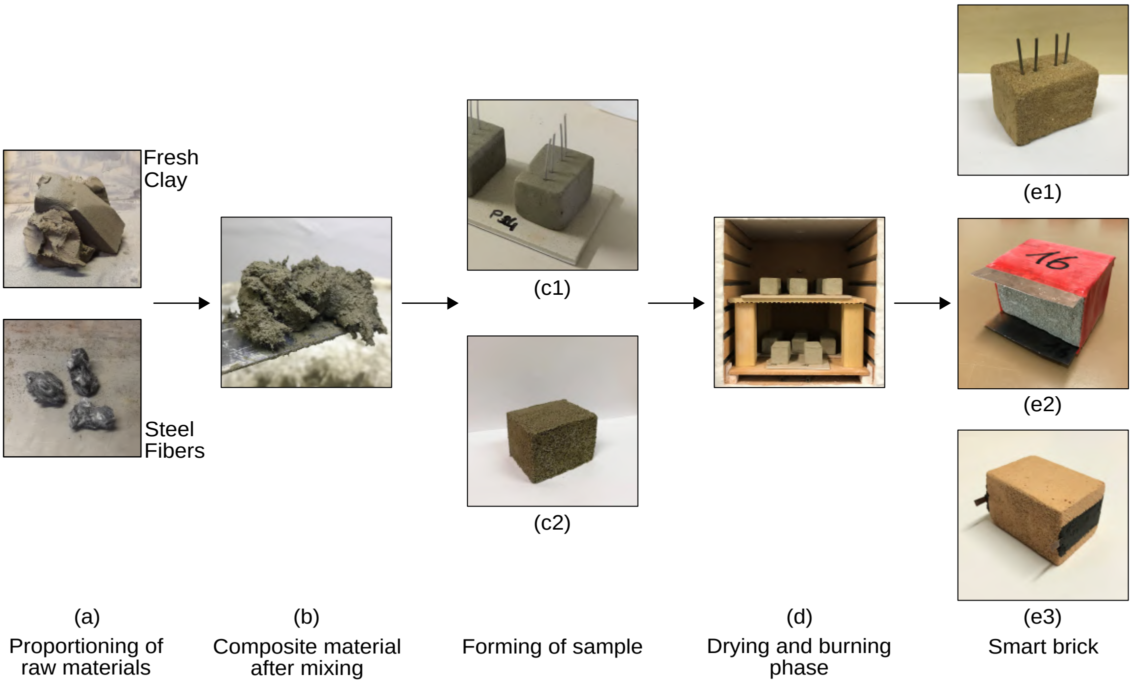

Fig. 4.5: Production process of smart bricks doped with stainless steel microfibers.

4.2.2 Electrical measurements

Experiments proposed in this work were conducted by performing electrical measurements by means of a biphasic Direct Current (DC) measurement approach developed, in the work proposed by Downey et al. (2017c), to reduce the polarization effect that commonly affects dielectric materials, such as the cement- or clay-based ones, by producing a time-based drift in their electrical outputs under the application of constant electrical inputs (Chung 2002; Hou and Lynch 2005). AC measurement approaches can be also used to eliminate the drift due to the polarization by charging and discharging the dielectric material, nevertheless, the electrical characteristics determined through the use of these techniques are still affected by a drift in time with respect to the provided electrical input (Wen and Chung 2002; Azhari and Banthia 2012b). Assuming that the time drift induced by the polarization effect is an intrinsic property of dielectric materials due to the application of a constant voltage to perform electrical measurements and that it is fully dependent on the direction of the generated current flow, the biphasic DC measurement approach reverses the direction of the current flow within the material to eliminate the polarization effect by applying a voltage square wave composed by a positive constant part, used to acquire current/voltage

measurements and a negative constant part, used for material depolarization by reversing the direction of the current flow. In particular, current/voltage measurements are taken when the acquired current/voltage signal is stable, approximately at the 80% of its positive constant part, to avoid drifts in the outputs with respect to the provided voltage input.
Electrical measurements on smart bricks were carried out by using an in-house developed software called "SHM-Smartbricks" (see Fig. 4.6). Based on Python environment (Rossum 1995), the software is a collection of tools able to handle both the data acquisition from the novel sensors, by exploiting National Instruments (NI) drivers, and the processing of the acquired data in real-time. In particular, data acquisition can be carried out by considering the approaches described below.

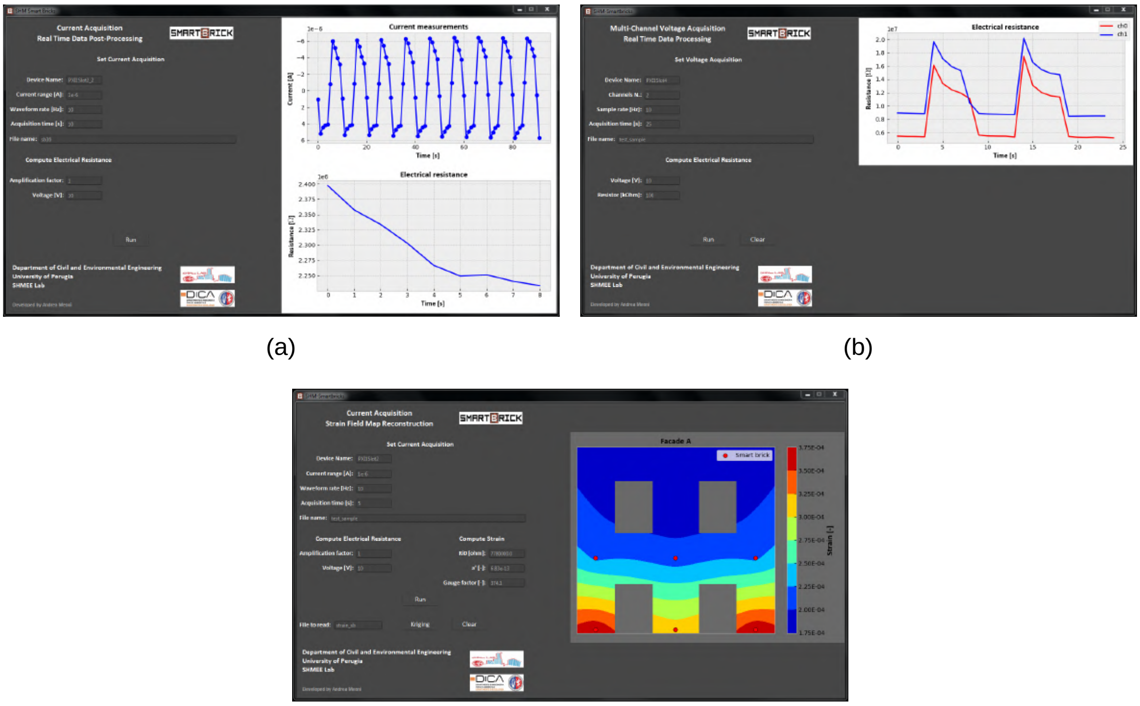
Current Acquisition
Real Time Data Post-Processing

Set Current Acquisition

Device Name:
Current range [A]: 1e-6
Waveform rate [Hz]: 10
Acquisition time [s]: 10
File name:

Compute Electrical Resistance

Amplification factor: 1
Voltage [V]: 10

Department of Civil and Environmental Engineering
University of Perugia
SHMEE Lab

Developed by Andrea Meoni

(a)

Multi-Channel Voltage Acquisition
Real Time Data Processing

Set Voltage Acquisition

Device Name:
Channels N.: 2
Sample rate [Hz]: 10
Acquisition time [s]: 25
File name: test_sample

Compute Electrical Resistance

Voltage [V]: 10
Resistor [kOhm]: 100

Department of Civil and Environmental Engineering
University of Perugia
SHMEE Lab

Developed by Andrea Meoni

(b)

Current Acquisition
Strain Field Map Reconstruction

Set Current Acquisition

Device Name:
Current range [A]: 1e-6
Waveform rate [Hz]: 10
Acquisition time [s]: 5
File name: test_sample

Compute Electrical Resistance

Amplification factor: 1
Voltage [V]: 10

Compute Strain

R0 [ohm]:
α* [-]: 6.83e-13
Gauge factor [-]: 374.1

File to read: strain_sb

Department of Civil and Environmental Engineering
University of Perugia
SHMEE Lab

Developed by Andrea Meoni

(c)

Figure 4.6: Screenshots from the software "SHM-Smartbricks" for acquisition and real-time processing of the data from smart bricks: (a) The tool dedicated to the single-channel acquisition of electrical measurements; (b) The tool dedicated to the multi-channel acquisition of electrical measurements; (c) Example of a tool for real-time processing of the data from smart bricks. In this case, the software reconstructs and displays the strain field map of a monitored building.

4.2.2.1 Single-channel acquisition

The single-channel acquisition approach allows performing electrical measurements on one smart brick at a time. According to the electrical setup shown in Fig. 4.7(a), a RIGOL DG1022 function generator was used to supply a voltage square wave of ±10 V (20 V peak-to-peak) with a duty cycle of 50% and a frequency of 1 Hz to the considered smart brick. The data acquisition system was composed of a chassis, model NI PXIe-1073, equipped with a digital multimeter NI PXI-4071 set at a sampling frequency of 10 Hz. Current measurements acquired from the novel sensor were post-processed to compute the total electrical resistance of the brick, R, according to Ohm's law:

$$R(t)|_{t=\tilde{t}} = \frac{V}{I(t)|_{t=\tilde{t}}}, \tag{4.1}$$

where V is the applied constant voltage in the positive part of the square wave, equal to +10 V, I is the measured current intensity value, and $\tilde{t}$ is the specific time instant when each current sample is taken. The total electrical resistance was resampled at 1 Hz according to the sample rate of the voltage square wave input.

Fig. 4.7(b) reports an example of application of the single-channel approach for conducting electrical measurements. A smart brick was subjected to a prestressing load of 1 kN by using a hand-operated hydraulic press. Every five seconds, approximately, the load acting on the sensor was reduced at about 0.3 kN. Load variations can be clearly detected by observing the time history of the total electrical resistance of the tested smart brick since each reduction in the applied load resulted in an increase in the value of the electrical output of the brick.

4.2.2.2 Multi-channel acquisition

The multi-channel acquisition approach allows performing electrical measurements on multiple smart bricks at a time. According to the electrical setup shown in Fig. 4.8(a), a RIGOL DG1022 function generator was used to supply a voltage square wave of ±10 V (20 V peak-to-peak) with a duty cycle of 50% and a frequency of 1 Hz to an MPX switcher, model Selit MD3060, capable of replicating the voltage input to multiple smart bricks. In order to determine the value of the current flowing within each channel, a known resistor, $R_{\text{in-line}}$, was arranged in series with each novel sensor, and the correspondent voltage drop, V_{drop}, was measured through an analog input module, model NI PXIe-4303, mounted on a chassis, model NI PXIe-1073. The current, I, flowing in the i-th channel was computed

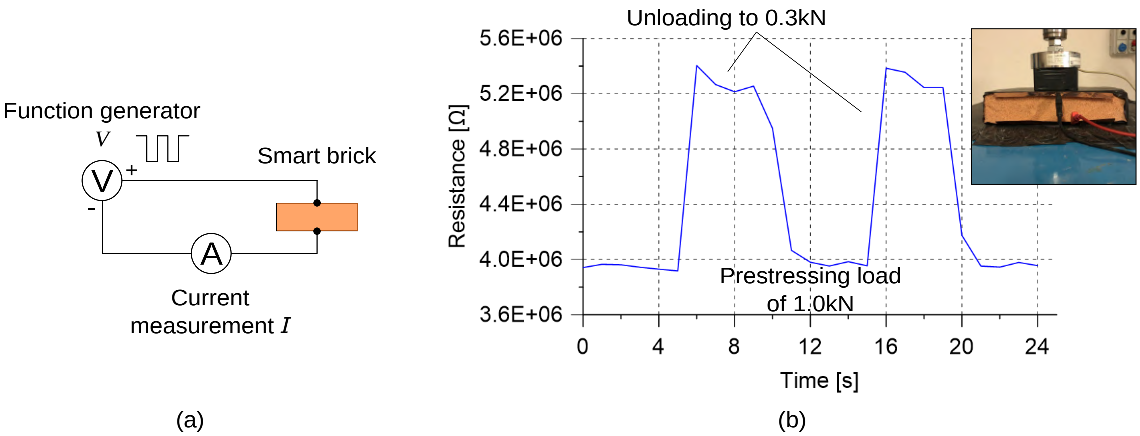

Figure 4.7: Electrical measurements on smart bricks: (a) Illustrative scheme of the setup for single-channel acquisition; (b) Time history of the total electrical resistance obtained from a smart brick tested under compression loads. The single-channel acquisition approach was adopted to acquire data from the novel sensor.

as follows:

$$I(t)_i|_{t=\tilde{t}} = \frac{V(t)_{\text{drop},i}|_{t=\tilde{t}}}{R_{\text{in-line},i}}, \tag{4.2}$$

where $\tilde{t}$ is the specific time instant when each voltage sample is taken. Therefore, the total electrical resistance of the smart brick correspondent to the i-th channel was determined through the following relationship:

$$R(t)|_{t=\tilde{t}} = \frac{V - V(t)_{\text{drop},i}|_{t=\tilde{t}}}{I(t)_i|_{t=\tilde{t}}}, \tag{4.3}$$

where V is the applied constant voltage in the positive part of the square wave, equal to +10 V. The total electrical resistance was resampled at 1 Hz according to the sample rate of the voltage square wave input.

Fig. 4.8(b) reports an example of application of the multi-channel approach for conducting electrical measurements. Two smart bricks, placed in column, were subjected to a prestressing load of 1 kN by using a hand-operated hydraulic press. Every five seconds, approximately, the load acting on the sensors was reduced at about 0.3 kN. Load variations can be clearly detected by observing the time histories of the total electrical resistance of the tested smart bricks since each reduction in the applied load resulted in an increase in the value of the electrical output of each brick.

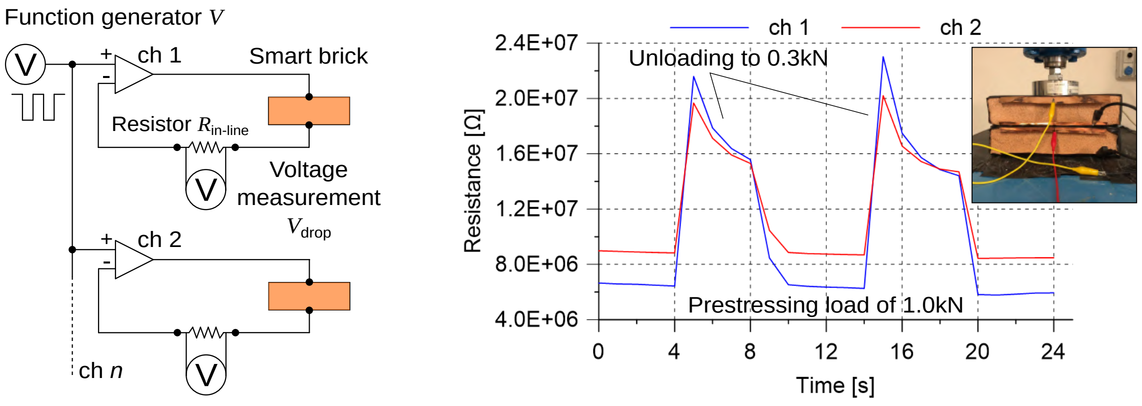

(a)

(b)

Figure 4.8: Electrical measurements on smart bricks: (a) Illustrative scheme of the setup for multi-channel acquisition; (b) Time histories of the total electrical resistance obtained from the two smart bricks tested under compression loads. The multi-channel acquisition approach was adopted to acquire data from the novel sensors.

4.2.3 Strain-sensing principle: Introduction of the series resistors model

Smart bricks made with stainless steel microfibers are durable clay bricks with an improved piezoresistive capability, whereby an increase in their compressive strain state leads to a reduction in their internal electrical resistance. Such an electromechanical behavior can be therefore exploited for strain monitoring purposes. Until today, variations in the internal electrical resistance of smart bricks and changes in their strain conditions were correlated through a linear relationship retrieved from the electromechanical model of the traditional RSGs (Ubertini et al. 2017a; Downey et al. 2017b):

$$\frac{\Delta R_{\mathrm{i}}}{R_{\mathrm{i},0}} = \frac{R_{\mathrm{i},\epsilon} - R_{\mathrm{i},0}}{R_{\mathrm{i},0}} = -\lambda\epsilon, \tag{4.4}$$

where ΔR_{i} is the change in the internal electrical resistance of the smart brick, $R_{\mathrm{i},\epsilon}$ and $R_{\mathrm{i},0}$ are the strained and unstrained internal electrical resistance of the smart brick, respectively, ϵ is the applied uniaxial strain, assumed positive in compression and λ is the gauge factor. This represents the amplification of strain by the electrical measurement, defined as:

$$\lambda = 1 + 2v + \frac{\frac{\Delta\rho}{\rho}}{\epsilon}, \tag{4.5}$$

where v is the Poisson's coefficient of the smart bricks and $\Delta\rho$ represents the relative change in resistivity under strained conditions, being ρ the electrical resistivity of the bricks. More in detail, the first term of Eq. (4.5), $1+2v$, represents the change in the electrical resistance of the bricks due to the change in their geometry, while the second one, $\frac{\Delta\rho}{\rho}/\epsilon$, characterizes the piezoresistive contribute of the gauge factor. It is worth noting that, in the case of smart bricks, the value of the second term can be varied depending on the amount of stainless steel microfibers present inside the clay matrices. On the other hand, in the case of traditional RSGs, this component can be considered small and stable, being their sensing principle largely due to the contribution of the first term of Eq. (4.5). According to the percolation theory, gradually increasing the content of conductive filler within an insulating matrix, a critical amount of filler, termed percolation threshold, can be reached. In its surrounding or above, the electrical conductivity of the composite material is significantly enhanced due to the formation of continuous conductive networks within the doped matrix. Below the percolation threshold, in the transition zone where the composite becomes a conductor, conductive paths of filler are weak, hence the electrical conductivity is slightly improved, whereas the strain-sensing capabilities of the doped material are greatly enhanced and the gauge factor reaches is maximum value (Cochrane et al. 2007; Ponnamma et al. 2018; Laflamme et al. 2018). Therefore, exploiting the percolation theory, the gauge factor of the smart bricks can be adjusted to match the best strain-sensing capabilities, unlike that of RSGs, whose fixed value is usually around 2. It should be noted that Eq. (4.4) can be written in a more practical form, suited for experimental applications, by pointing out the strained internal electrical resistance of the bricks, $R_{\mathrm{i},\epsilon}$:

$$R_{\mathrm{i},\epsilon} = -\lambda R_{\mathrm{i},0}\epsilon + R_{\mathrm{i},0}, \tag{4.6}$$

It is also interesting to note that the piezoresistivity is not the only contribution that should be taken into account for describing the strain-sensing behavior of the smart bricks when these are equipped with external copper plate electrodes. Indeed, the presence of a dry contact between the surfaces of the smart bricks and those of the electrodes results in a contact resistance, R_{c}, that introduces a non-linearity, dependent on the compression stress, σ, acting on the sensor, between the changes in strain of the novel sensor and the variations in its electrical resistance. Therefore, the contribution due to the contact resistance at the sensing is considerable when smart bricks are subjected to a relatively low compression state, whereas it tends to negligible values by increasing σ. According to the literature, the contact resistance and can be expressed through the following simplified equation (Zhang et al. 2019):

$$R_{\mathrm{c}} = a\sigma^{-b} + R_{\mathrm{c},\infty}, \tag{4.7}$$

where a and b are positive constants, while $R_{\mathrm{c},\infty}$ represents the value of the contact resistance for infinitely large stress.

In light of that, this work proposes an innovative electromechanical model, called series resistors model, to describe the strain-sensing behavior of the smart bricks by linearly linking Eq. (4.6) and Eq. (4.7), hence taking into account the piezoresistive effect and the sensing at the contact electrodes simultaneously (Fig. 4.9). In particular, assuming a linear elastic mechanical behavior of the smart bricks, whereby σ can be replaced with $E\epsilon$, being E the Young Modulus of the bricks, the total electrical resistance of the novel sensors, R, is now correlated to the applied strain, ϵ, as follows:

$$R = R_{\mathrm{i},\epsilon} + R_{\mathrm{c}} = a(E\epsilon)^{-b} - \lambda R_{\mathrm{i},0}\epsilon + R_{\mathrm{i},0} + R_{\mathrm{c},\infty}, \tag{4.8}$$

It should be noted that the value of ϵ, reported in Eq. (4.8), is always greater than zero, since either when tested in laboratory conditions under compression loads or embedded within masonry structural elements, smart bricks are strained by prestressing or dead loads, respectively. The relative change in total electrical resistance, $\Delta R/R_{\mathrm{i},0}$, under applied strain, is:

$$\frac{R - R_{\mathrm{i},0}}{R_{\mathrm{i},0}} = \frac{\Delta R}{R_{\mathrm{i},0}} = \frac{aE^{-b}}{R_{\mathrm{i},0}}\epsilon^{-b} - \lambda\epsilon + \frac{R_{\mathrm{c},\infty}}{R_{\mathrm{i},0}}, \tag{4.9}$$

In a more convenient way for experimental applications, the series resistors model, formerly expressed through Eq. (4.9), can be rewritten as:

$$\frac{\Delta R}{R_{\mathrm{i},0}} = a'\epsilon^{-b} - \lambda\epsilon + c', \tag{4.10}$$

where a' represents the relative sensing at the contact resistance and c' is the relative series materials resistance. This last term is only retained for completeness since in practical applications it assumes negligible values, considering that $R_{\mathrm{i},0} >> R_{\mathrm{c},\infty}$. The herein proposed innovative electromechanical model is therefore capable of taking into account an extra sensitivity at the electrodes that can support the detection of changes in the strained state of smart bricks when dealing with small loads, such as prestressing or dead ones. Conversely, according to Eq. (4.10), at relatively high compressive states, the strain-sensing behavior of the smart bricks is totally dependent on the contribution of the piezoresistivity, i.e. on the gauge factor λ, since the contact resistance tends to vanish.

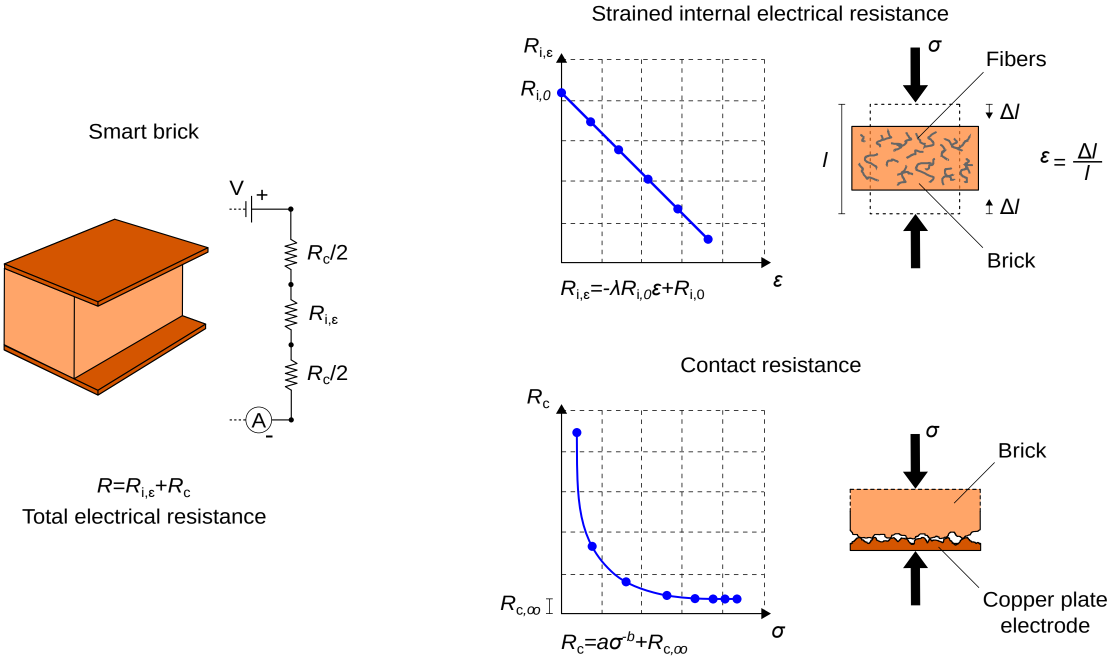

Figure 4.9: Illustrative scheme of the series resistors model describing the strain-sensing behavior of the smart bricks.

4.3 Characterization of the smart bricks: Methodology

This section illustrates the methodologies of the experiments performed to achieve a comprehensive characterization of smart bricks made with stainless steel microfibers. In particular, their electrical, electromechanical, physical and mechanical properties are investigated. The influence of the environmental effects, due to changes in temperature and humidity, on the electrical outputs of the novel sensors is also studied.

4.3.1 Electrical tests

The methodology pursued for the assessment of the percolative behavior of smart bricks is herein illustrated. Tests proving the benefits experienced in the use of external copper plate electrodes for conducting electrical measurements are also described.

4.3.1.1 Percolative behavior

Smart bricks are made of a composite dielectric material that possesses a percolative behavior herein investigated through the assessment of the internal electrical conductivity of the novel sensors as the content of stainless steel microfibers used for their production varies. It is worth noting that, according to the percolation theory, the definition of the percolation curve of the smart bricks is of the utmost importance for the enhancement of their piezoresistivity and therefore for the optimization of their production process. In order to investigate a percolation curve of a broad range, smart bricks with a content of steel fibers equal to 0.00%, 0.25%, 0.50%, 1.00%, 1.50%, 3.00%, and 5.00%, were produced and instrumented with conductive resin stripe electrodes, as described in Section 4.2.1. It is worth remarking that the use of such an electrode typology allows performing measurements of the internal electrical conductivity of the novel sensors with negligible contact resistance.

Electrical measurements were performed by following the methodology described in Section 4.2.2.1, hence the internal electrical conductivity of the bricks, $1/\rho$, was computed according to the following equation:

$$\frac{1}{\rho} = \frac{l}{A \cdot V/I(t)|_{t=\tilde{t}}}, \tag{4.11}$$

where l is the gap between the conductive resin stripe electrodes, A is the cross-section of the smart brick, V is the applied constant voltage in the positive part of the square wave (+10 V), I is the current intensity value measured at a fixed time $\tilde{t}$, in this case, equal to 144 s.

4.3.1.2 Use of the external copper plate electrodes

The use of the external copper plate electrodes instead of the embedded stainless steel wires, initially proposed for instrumenting smart bricks by Downey et al. (2017b), was investigated by performing electrical tests on two series of sensors made by following the manufacturing process described in Section 4.2.1. In particular, contents of steel fibers (equal to 0.00%, 0.25%, 0.50%, 1.00%, 1.5%, 2.0%, as explained later in Section 4.4.1.1) comprised within the percolation thresholds identified by studying the electrical behavior of the novel sensors according to the Section 4.3.1.1, were taken into account for this study. A series of sensors was therefore equipped with embedded wire electrodes, while the other was instrumented with copper plates electrodes. Each smart brick was subjected to a prestressing load of 0.5 kN by using a hand-operated hydraulic press. Electrical measurements were carried out as reported in Section 4.2.2.1, hence the percentage variation in the total electrical resistance of the investigated formulations of smart bricks was assessed.

4.3.2 Electromechanical tests

Two types of experiments are exemplified in this section: First, axial compression tests are carried out on single smart bricks to validate the series resistors model and to carry out the characterization of the strain-sensing behavior of the novel sensors as the content of stainless steel microfibers used for their production varies. Second, further compression tests are performed to investigate the effectiveness of the smart bricks in measuring strain under increasing compression loads by benchmarking their outputs against those provided by RSGs mounted on each tested sample.

4.3.2.1 Validation of the series resistors model by testing single smart bricks

Smart bricks instrumented with external copper plate electrodes were subjected to axial compression tests to validate the use of the series resistors model, previously proposed in Section 4.2.3, for retrieving strain measurements by means of the post-processing of the electrical outputs from the novel sensors. In particular, taking into account the results obtained from the assessment of the percolation curve of the smart bricks according to the methodology reported in Section 4.3.1.1, this study involved sensors produced with contents of steel fibers comprised within the first percolation threshold (i.e. 0.25% and 0.50% as described later in Section 4.4.1.1) by following the manufacturing process in Section 4.2.1. Plain samples were also tested as benchmark. Electromechanical tests were carried out with the experimental setup shown in Fig. 4.10(a), by applying the load history, reported in Fig. 4.10(b), on each sample through an electric-servo test machine, model Advantest 50-C7600 by Controls, mounting a servo-hydraulic control unit, model 50-C 9842.

The electrical measurements were conducted by following the approach illustrated in Section 4.2.2.1, while three LVDTs were employed to acquire displacements from which the strain applied to each sensor were retrieved through simple data post-processing. The theoretical model proposed for describing the strain-sensing behavior of the smart bricks was validated by carrying out a fitting procedure of the parameters in Eq. (4.10) on the experimental data collected by performing the experiments. Therefore, the strain-sensing behavior of each investigated formulation of smart bricks was evaluated by assessing the quality of such fitting and the entity of the obtained parameters, whose estimation procedure consisted of two-step. Initially, data of the total electrical resistance of smart bricks versus the applied strain acquired above 1.5 MPa, i.e. at relatively high compressive states where contact resistance is negligible, were fitted by performing linear regressions (Fig. 4.11(a)). Herein, the strain-sensing capability of the novel sensors was characterized by

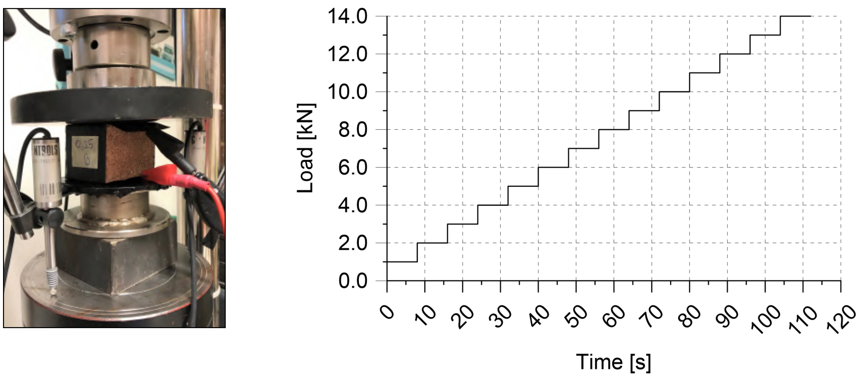

(a) (b)

Figure 4.10: Electromechanical tests carried out on smart bricks for the validation of the series resistors model: (a) Laboratory setup of an axial compression test on a smart brick; (b) Load history applied on each sample.

assessing the slope coefficient of the interpolating linear function, which in this case represented the gauge factor, λ, and the coefficient of determination, R^2, which pointed out the linearity of the response of the sensors. Performed linear regression analysis also permitted the estimation of $R_{i,0} + R_{c,\infty}$, that is the intercept of the linear trend when the smart brick is unstrained. Since the experience shows that $R_{i,0} >> R_{c,\infty}$, this fitting also allowed determining the unstrained internal electrical resistance of smart bricks, $R_{i,0}$. A second step consisted of a curve-fitting procedure performed on data of the relative change in the total electrical resistance of smart bricks versus the applied strain collected in the entire investigated compressive range (Fig. 4.11(b)). The relative sensing at the contact resistance, a' and the relative series materials resistance, c', were therefore estimated. It is worth noting that both a' and c' were imposed to be positive in the curve-fitting procedure, while the parameter b was considered constant and equal to 3 for each investigated formulation of smart bricks, owing to a separate check. Completing the calibration procedure, the strain-sensing behavior of each tested smart bricks was fully characterized, permitting the definition of three equations corresponding to the investigated contents of steel fibers, whose parameters were obtained by computing the average value of the terms contained in Eq. (4.10) for each formulation of smart bricks. The coefficient of determination of the curve-fitting procedure, R^2, was adopted to evaluate the effectiveness of the series resistors model in replicating the trends of the experimental data. Fitting procedures and data post-processing were carried out in Python environment by adopting the SciPy and NumPy packages (Jones et al. 2001; Oliphant 2006).

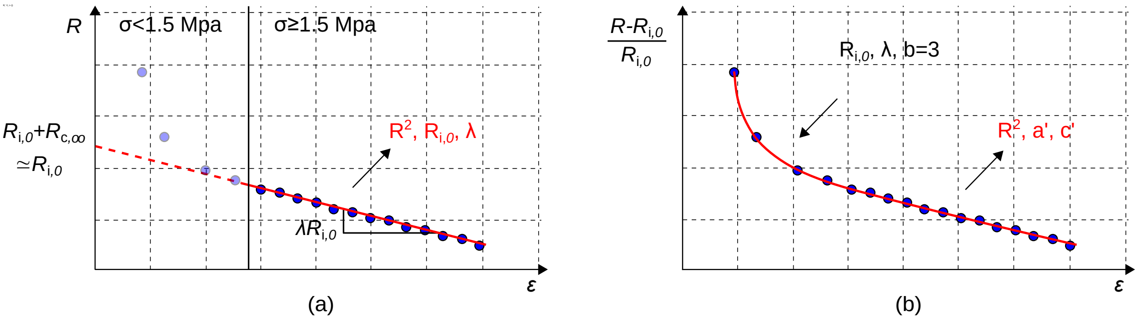

Figure 4.11: Exemplification of the calibration procedure of the series resistors model performed in two steps: (a) Step one, post-processing of data acquired above 1.5 MPa by means of the linear regression analysis; (b) Step two, curve-fitting procedure carried out on data acquired within the entire investigated compressive range.

4.3.2.2 Effectiveness of smart bricks in strain measurements

The effectiveness of smart bricks in measuring strain under increasing compression loads was studied by carrying out electromechanical tests on samples instrumented with RSGs so as comparing the outputs from the novel sensors with those from a well-known strain-sensing device. A content of filler equal to 0.50% was chosen for manufacturing smart bricks for this investigation by following the production process reported in Section 4.2.1. The tested samples were therefore equipped with external copper plate electrodes and further instrumented with two RSGs, model Kyowa KFG-20-120-C1-11L1M2R, characterized by a gauge factor equal to 2.11 and bonded onto the front and rear surfaces of each brick, respectively. Axial compression tests were performed by following the methodology previously reported in Section 4.3.2.1, by using the laboratory setup depicted in Fig. 4.12(a) and by applying the load history plotted in Fig. 4.12(b). Strain measurements of each tested smart brick were estimated by post-processing the electrical outputs through Eq. (4.10), hence benchmarked against the average strain computed from the corresponding couple of RSGs. It is worth noting that Eq. (4.10) was calibrated according to the strain-sensing capabilities of each tested smart brick by means of the procedure described in Section 4.3.2.1. A data acquisition card, model NI PXIe-4330, hosted within the chassis NI PXI-1073 and set to a sampling rate of 10 Hz, was employed to acquire measurements from RSGs.

4.3.3 Physical and mechanical properties

Physical and mechanical properties of smart bricks made with stainless steel microfibers are investigated with the methodologies hereinafter illustrated. In particular, Computed

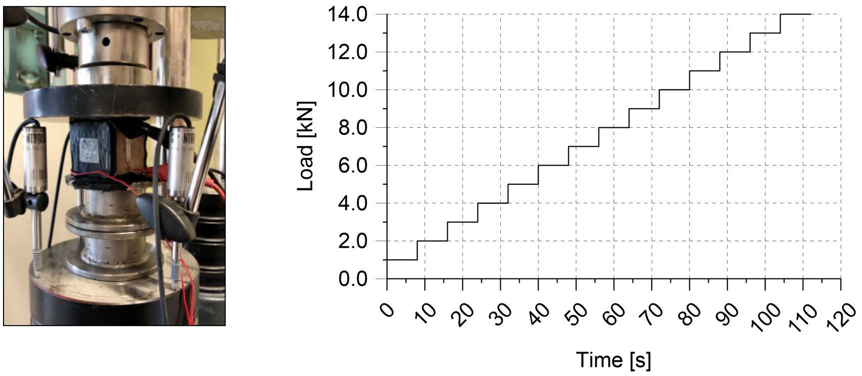

(a) (b)

Figure 4.12: Electromechanical tests carried out on smart bricks to study their effectiveness in strain measurements: (a) Laboratory setup of an axial compression test on a smart brick instrumented with a couple of RSGs; (b) Load history applied on each sample.

Tomography (CT) scans are carried out to examine the internal structure of the smart bricks evaluating the dispersion of the steel fibers within the clay matrices, while compression and three-point bending tests are performed to assess the influence of various contents of the electrically conductive filler to the mechanical properties of the novel sensors.

4.3.3.1 Computed tomography scan

This non-invasive imaging technique permits the analysis of 3D volumes of heterogeneous materials by means of the reconstruction of X-Ray projections of the scanned sample, in which dense constituents, such as the steel-based ones, can be identified owing to their marked X-Ray attenuation (Heijs et al. 1995; Carrara et al. 2018). Samples of smart bricks were therefore subjected to CT scanning to investigate their internal structure evaluating the dispersion of the stainless steel microfibers within the doped clay matrices. Tests were carried out on cylindrical samples of diameter of 7 mm retrieved by drilling the horizontal surface of smart bricks made with contents of steel fibers comprised within the first percolation threshold identified according to the methodology reported in Section 4.3.1.1 (i.e. 0.25% and 0.50% as described later in Section 4.4.1.1). Doped samples were produced by following the procedure in Section 4.2.1, as well as the plain brick scanned for reference (Fig. 4.13(a)). Experiments were carried out at the Laboratories of the Technische Universität Braunschweig by using a CT scanner, model EasyTom Nano by RX Solutions (Fig. 4.13(b)), with the setup reported in Table 4.1.
Data analysis was performed by employing a dedicated commercial software, named Avizo

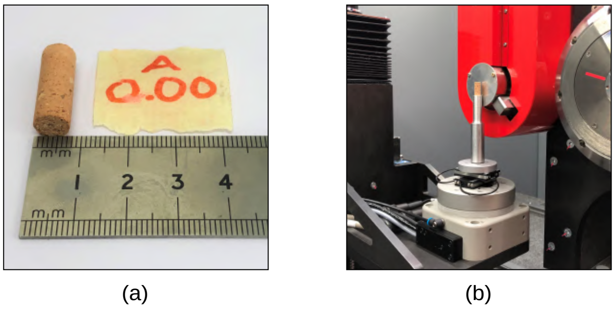
(a) (b)

Fig. 4.13: X-Ray CT scan of smart bricks: (a) Example of a tested sample (the plain brick); (b) Setup of a sample in the CT scanner.

Table 4.1: Setting of the CT scanner employed to examined samples of smart bricks.

Voltage [kV]	Current [μA]	Number of images	Voxel size [μm]	Filter
140	71	1440	5	0.1 mm Aluminum

(Scientific 2018), which allowed the visual assessment of 16-bit grayscale pictures of the 2D orthogonal projections of each scanned sample, along with its 3D volume reconstruction. Exploiting the software library OpenCV (Bradski 2000), a custom Python procedure was specifically developed to statistically characterize, at a first level of approximation, the presence of the steel-based filler within the cylindrical samples by counting bright single pixels present inside the pictures of the 2D horizontal scans, attributable to well-dispersed steel fibers, after removing clusters of pixels, which represented metallic inclusions in the clay or agglomerations of fibers, according to the following two-step procedure: considering the original 16-bit grayscale pictures scaled to 8-bit, pixels with an intensity value over 20 and grouped inside a perimeter equal to or greater than 1000 pixels were deleted in a first iteration. Afterward, clusters with a perimeter over 5 pixels and characterized by a pixel intensity value equal to or greater than 200 were deleted through a second iteration. Bright single pixels were finally counted from post-processed pictures by taking only into account pixels with an intensity value equal to or larger than 200. It is worth noting that the procedure was applied on five equally spaced projections for each scanned sample, considering equally sized pictures of their 2D scans. The dispersion of the steel fibers within each scanned sample was evaluated through the computation of a distribution index, I_f, defined as follows:

$$I_\mathrm{f} = \frac{1}{n}\sum_{i=1}^{n}\frac{p_i}{p_i'}\cdot 100 \tag{4.12}$$

where n is the number of 2D horizontal projections taken into account for each examined sample (in this case, n=5), while p and p' are the number of pixels, without counting clusters and counting clusters, respectively, present inside the i-th projection. According to Eq. (4.12), large values of the index point out a better dispersion of the steel fibers with respect to the other metallic inclusions.

4.3.3.2 Compression tests

Displacement-controlled compression tests were performed for determining the secant elastic modulus and the compressive strength of smart bricks made, according to the production process reported in Section 4.2.1, with contents of stainless steel microfibers comprised within the first percolation threshold (i.e. 0.25% and 0.50% as described later in Section 4.4.1.1). This was identified by following the methodology reported in Section 4.3.1.1. Samples made of plain clay were also tested as benchmark. Compression tests were carried out with a constant displacement rate of 5 μm/s measured by using three LVDTs. Friction at the interfaces between plates of the test machine and smart bricks was reduced by employing polytetrafluoroethylene (PTFE) sheets. Measurements of relative displacement were used for retrieving strain applied to each sample, allowing the definition of the compressive stress versus strain curves. The secant elastic modulus of each tested smart brick was determined by considering a stress equal to the 40% of the compressive strength and its corresponding value of the axial strain, according to the Italian Technical Standards for Constructions (*Circolare esplicativa del 02.02.2009 contenente "Istruzioni per l'applicazione delle nuove norme tecniche per le costruzioni di cui al D.M. 17.01.2018"* 2009).

4.3.3.3 Three-point bending tests

Displacement-controlled three-point bending tests were performed for determining the fracture energy for the opening mode of fracture of smart bricks made according to the production process reported in Section 4.2.1 with sizes of 40x40x160 mm^3 and without the addition of electrodes. Tests involved sensors containing amounts of stainless steel microfibers comprised within the first percolation threshold (i.e. 0.25% and 0.50% as described later in Section 4.4.1.1) determined by carrying out the electrical tests illustrated in Section 4.3.1.1, along with samples made of plain clay. Bending tests were carried out following the methodology reported in RILEM (1985), by applying a downward load on the center of each sample. These were positioned within the testing machine with a span of 100 mm. A constant displacement rate of 2 mm/min, measured by using three LVDTs, was considered for reaching the maximum applied load within 30-60 s since the beginning of the test. According to the adopted Technical Standards, a notch of depth of 20 mm and width of 4 mm was made at the centerline of the samples before the drying phase. Relative displacements at the center of each sample were automatically measured by the testing machine. It is worth noting that the determination of the fracture energy for the opening mode of fracture of smart bricks is of the utmost importance in particular for the calibration of the CDP model adopted in this work to numerically reproduce the behavior of the masonry and its components.

4.3.4 Environmental effects on the electrical outputs of the smart bricks

Especially in the case of long-term acquisitions, it is of the utmost importance to understand how environmental effects induce changes in the total electrical resistance of the smart bricks by producing noise in their electrical outputs. This phenomenon makes challenging distinguishing if changes in the total electrical resistance are due to modifications in the structural response of the monitored construction or to variations in the climatic conditions. Experiments to determine the influence of environmental effects, due to changes in temperature and humidity, on the electrical outputs of smart bricks made with stainless steel microfibers were therefore carried out by testing masonry subassemblies, consisting of three bricks arranged in column with mortar layers, under outdoor climatic conditions. This structural setting is particularly effective for testing smart bricks without the application of prestressing loads on the sensors. Indeed, while the smart brick to be tested was positioned in the central row of the subassembly, the other bricks, placed above and below the sensor, respectively, ensured the stabilization of the external copper plate electrodes. Since conventional clay bricks were employed to build the structural setting, the smart brick was produced with standard dimensions of 250x120x55 mm^3 by following the manufacturing process reported in Section 4.2.1. For practical reasons, only a smart brick made with a content of stainless steel microfibers equal to 0.25%, with respect to the weight of fresh clay, was produced and tested. Layers of lime mortar were used to arrange the bricks. A further masonry subassembly, built by using three conventional clay bricks, was also tested as benchmark. In this case, the brick placed in the middle of the structural setting was turned into a sensor, hence it was instrumented with external copper plate electrodes and insulated from the other masonry components avoiding current flow propagation (Fig. 4.14(a)). Electrical measurements were carried out by using the methodology described in Section 4.2.2.1, while temperature and humidity were acquired through a Tinytag data logger, model TGP-4017, placed in the proximity of the tested sensors (Fig. 4.14(b)).
Data were continuously acquired for 24 hours by performing six measurements per hour.

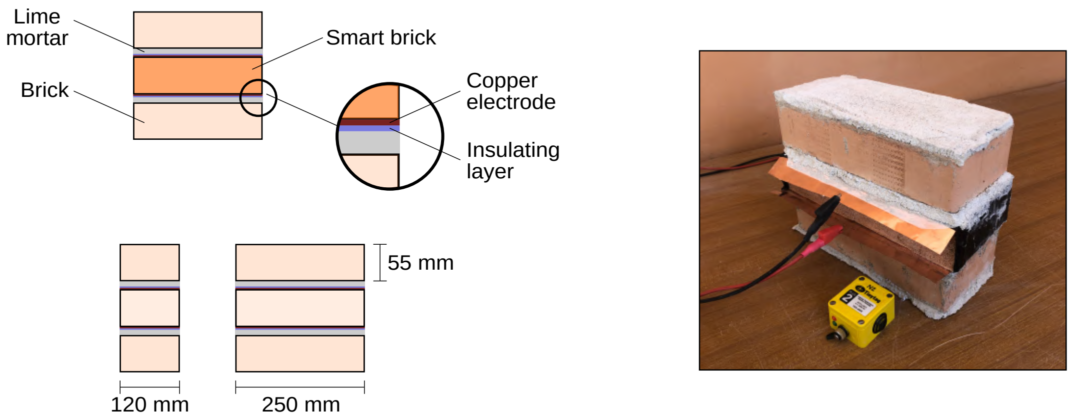

(a)

(b)

Fig. 4.14: Investigation on the influence of the environmental effects, due to changes in temperature and humidity, on the electrical outputs of the smart bricks: (a) Exemplification of the tested subassemblies; (b) Setup for outdoor measurements.

The mean values of the total electrical resistance, temperature, and relative humidity were computed at each hourly interval. Exemplifying a compensation of the electrical outputs from environmental effects, a simple linear regressive model was adopted to remove the noise due to the changes in temperature from the total electrical resistance of the smart bricks (Ubertini et al. 2017b). Accordingly, such a regressive model was invoked to predict the dependent variables, y_i, representing the predicted values of the total electrical resistance of a smart brick, considering the independent variables, x_i, hence the recorded values of the temperature, as follows:

$$y_i = b_0 + b_1 x_i, \tag{4.13}$$

where b_0 and b_1 are the predicted weights that minimize the sum of squared residuals. The error term of the statistical model, e_i, was computed by considering the following relationship:

$$e_i = \hat{y}_i - y_i, \tag{4.14}$$

where $\hat{y}_i$ is the value of the total electrical resistance acquired from the smart brick. It is worth noting that the obtained residuals are unaffected by environmental effects and can be therefore used as indicator of the structural integrity of the monitored construction by associating large variations in their trend to modifications in the structural response of the construction being monitored.

4.4 Characterization of the smart bricks: Results

This section collects the results obtained by carrying out the experiments proposed in this work to achieve a comprehensive characterization of the electrical, electromechanical, physical, and mechanical properties of smart bricks made with stainless steel microfibers. Results from the investigation on the environmental effects on the electrical outputs of the novel sensors were also presented.

4.4.1 Electrical tests

Results obtained from the investigation carried out on the percolative behavior of the smart bricks are discussed below, along with those found by performing electrical measurements with both external and embedded electrodes from the novel sensors.

4.4.1.1 Percolative behavior

Measurements of the internal electrical conductivity of smart bricks made with different contents of stainless steel microfibers and equipped with resin stripe electrodes are plotted in Fig. 4.15. As expected, the conductivity of the novel sensors is boosted by increasing the content of steel fibers within the clay matrices. Although the plotted trend always grows, above 1.50% of filler content, continuous conductive networks were reasonably well-formed and further additions of steel fibers only produced a slight increase in the electrical outputs. Overall, observing the entire curve, it can be noted that the percolation of smart bricks seems to be characterized by a double threshold (Sumita et al. 1991; Wen and Chung 2007). Indeed, a first percolation threshold can be identified between 0.25% and 0.50%, while a second one between 1.50% and 3.00%. In such a percolative behavior, the first threshold is commonly attributable to the amount of filler dispersed within the matrix, while the second threshold is due to the electrical continuity of the matrix itself. Therefore, even considering the results obtained by performing CT scans according to the methodology presented in Section 4.3.3.1, the second percolation threshold, in this case, can be conceivably attributed to the metallic inclusions intrinsically dispersed within the clay matrices and randomly connected with the steel fibers developing internal continuous electrically conductive chains (see Section 4.4.3.1). As a result, once a certain number of continuous conductive paths were formed, the electrical properties of smart bricks were further boosted. It should be noted that the assessment of the percolative behavior, i.e.

of the percolation curve, was exploited in this work for supporting the optimization of the production process of the smart bricks since the contents of filler comprised within the first percolation threshold were selected for performing further investigations concerning the strain-sensing capabilities of the novel sensors and for carrying out studies on their physical and mechanical properties.

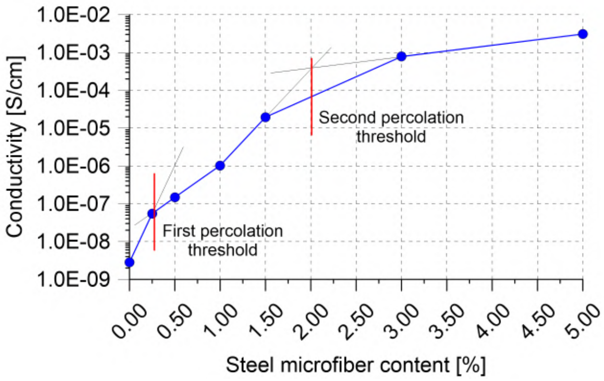

Figure 4.15: Percolation curve of smart bricks doped with stainless steel microfibers.

4.4.1.2 Use of the external copper plate electrodes

Results of the percentage variation in the total electrical resistance of smart bricks computed from measurements performed with both embedded and external electrodes are shown in Fig. 4.16. Measurements conducted by using external copper plate electrodes demonstrate that smart bricks become more conductive by increasing the content of steel fibers within the clay matrices. On the contrary, the trend representing the outputs provided by the embedded stainless steel wire electrodes indicates that the percentage variation of the resistance increased at each increment of conductive filler dispersed within the matrices. Such a phenomenon can be attributed to the development of a contact resistance between the surface of wire electrodes and the doped clay. Indeed, taking into account the production process of the bricks presented in Section 4.2.1, the experience demonstrates that the addition of steel fibers within the clay matrices slight reduces the workability of the composite material. Accordingly, the embedding of wire electrodes in the wet bricks before the drying phase produces holes bigger than expected and that increase with the decreasing of workability, leading to a faulty contact between electrodes and the surrounding doped material that does not allow to perform accurate electrical measurements. Therefore, considering that the use of steel wire electrodes embedded in smart bricks doped with steel fibers poses questions concerning their reliability, this work promotes the employment of external copper plate electrodes for conducting electrical measurements from smart bricks made with steel fibers.

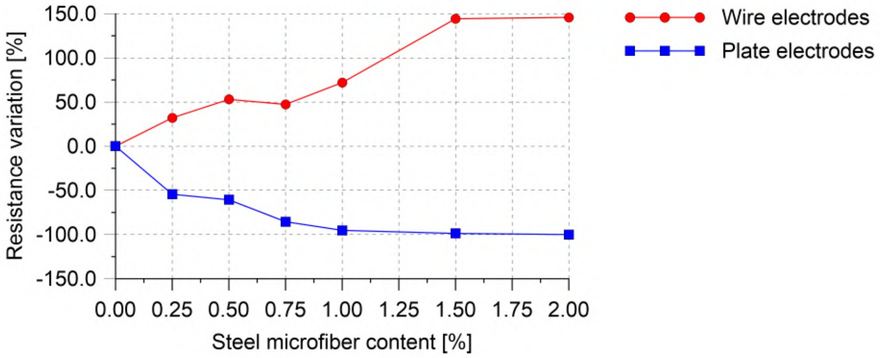

Figure 4.16: Percentage variation in the total electrical resistance of smart bricks computed from measurements performed with both embedded steel wire electrodes and external copper plate electrodes by varying the contents of dispersed steel fibers.

4.4.2 Electromechanical tests

This section outlines the results obtained by conducting electromechanical tests on smart bricks for the validation of the series resistors model and for the investigation on their effectiveness in measuring strain when subjected to increasing compression loads.

4.4.2.1 Validation of the series resistors model by testing single smart bricks

Smart bricks made of 0.25% and 0.50% of stainless steel microfibers, with respect to the weight of fresh clay, and plain bricks were tested under axial compression loads to validate the previously proposed series resistors model by exploiting a two-step calibration procedure. All the tested samples demonstrated a clear sensitivity in the investigated compressive range, as confirmed by the time histories of the total electrical resistance plotted for each sensor in Fig. 4.17. Although every increment in the applied load led to a reduction in the total electrical resistance of the samples, at low compressive states, i.e. below 1.5 MPa (5 kN), the decrease in the electrical resistance is non-linear, particularly in the case of smart bricks made with a content of steel fibers of 0.50%, with respect to the weight of fresh clay, which are the most electrically conductive bricks among the tested samples. As a result, within the compression range between 0.3 MPa and 1.5 MPa, the strain-sensing capabilities of the samples are largely due to the contribution of the contact resistance instead of their piezoresistivity. Above compression states of 1.5 MPa, trends of the total electrical resistance linearly decrease as the applied compression load increases. In this case, therefore, variations in the electrical outputs of the sensors can be attributed to their piezoresistive behavior since the contact resistance assumed negligible values.

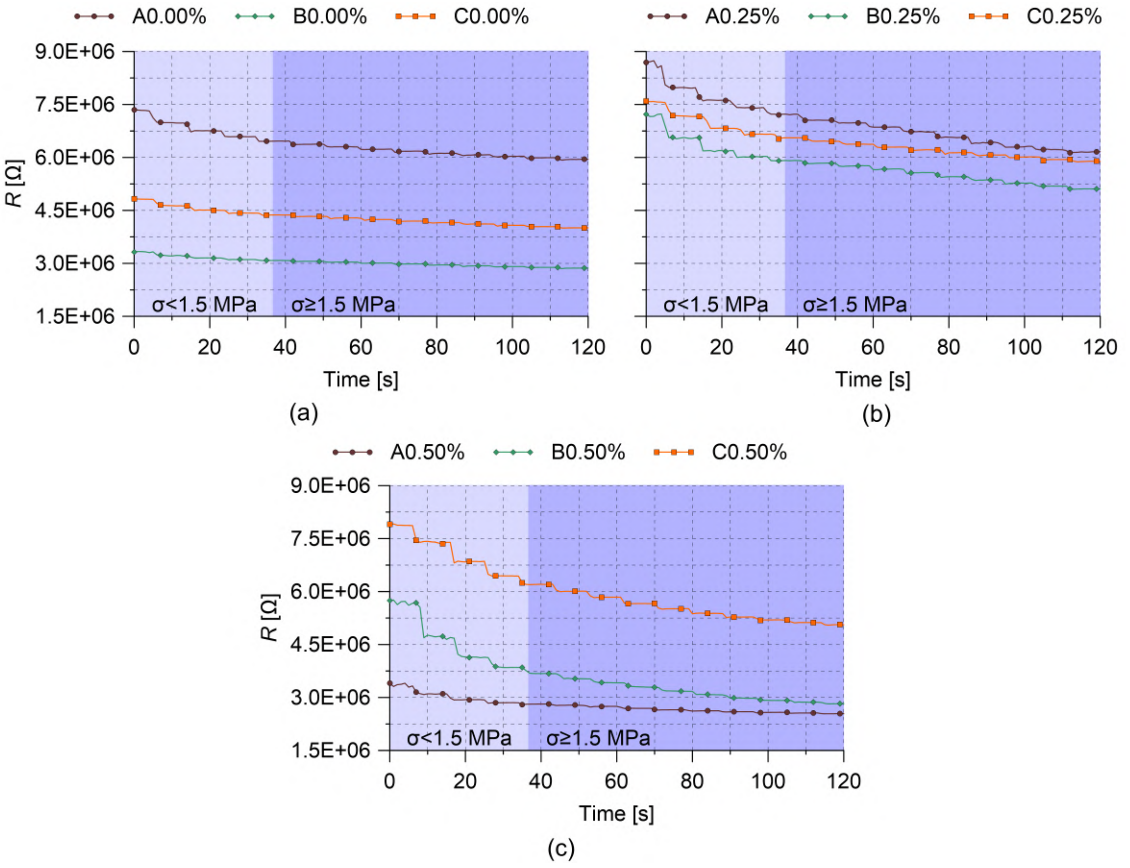

Figure 4.17: Total electrical resistance measured by the smart bricks subjected to electromechanical tests: (a) Plain samples; (b) Samples made of 0.25% of steel fibers; (c) Samples made of 0.50% of steel fibers.

Results of linear regression analysis carried out on trends of the total electrical resistance above 1.5 MPa are depicted in Fig. 4.18(a, b, c), which also reports the gauge factors computed for each tested sample and each investigated formulation (Fig. 4.18(d)).

All the sensors outputted a linear electrical response when compressive strained up to 4 MPa, especially smart bricks made of 0.25% of steel fibers, whose fitting is characterized by an average coefficient of determination, R^2, of 0.9916. The addition of the filler improved the linearity of the response of this formulation compared to that of the tested plain bricks, whose R^2 is 0.9797. On the contrary, the increase in the content of filler up to 0.50% resulted in a slight decrease in the linearity response of the corresponding formulation

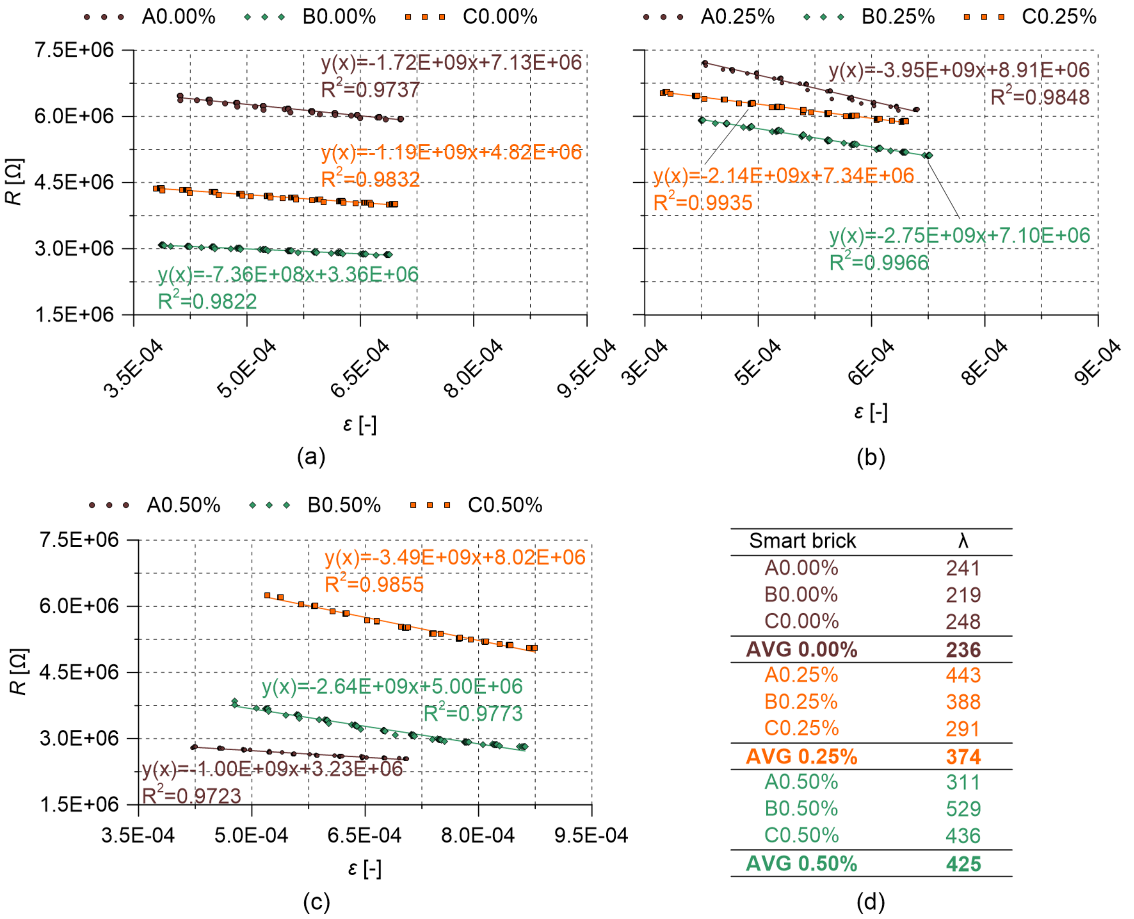

(a) (b)

Smart brick	λ
A0.00%	241
B0.00%	219
C0.00%	248
AVG 0.00%	**236**
A0.25%	443
B0.25%	388
C0.25%	291
AVG 0.25%	**374**
A0.50%	311
B0.50%	529
C0.50%	436
AVG 0.50%	**425**

(c) (d)

Figure 4.18: Total electrical resistance of smart bricks versus the applied strain measured above 1.5 MPa: (a) Plain samples; (b) Samples made of 0.25% of steel fibers; (c) Samples made of 0.50% of steel fibers; (d) Gauge factors obtained by carrying out linear regression analysis on data gathered by testing smart bricks above 1.5 MPa. AVG indicates the average gauge factor computed for each formulation of smart bricks.

of smart bricks, whose average R^2 is 0.9783. This is however comparable to the others. The percolative behavior of the novel material can be the cause of that phenomenon, in particular the proximity of the considered content of fibers with the first percolation threshold. The piezoresistive capability of smart bricks was improved by increasing the content of filler within the matrices, as demonstrated by the average values the gauge factors, 236, 374, 425, computed for sensors with 0.00%, 0.25%, 0.50% of steel fibers, respectively. Table 4.2 collects results from both linear regression analysis and curve-fitting procedures, providing a complete overview of the characterization of the series resistors model according to the investigated formulations.

Table 4.2: Results obtained from the experimental characterization of the strain-sensing behavior of the investigated formulation of smart bricks: $R_{i,0}$ is the unstrained internal electrical resistance of the smart brick, a' is the relative sensing at the contact resistance, b is the contact resistance exponential term, λ is the gauge factor, and R^2 is the coefficient of determination of the curve-fitting.

Sample	$R_{i,0}$ [MΩ]	a'	b	λ	R^2
A0.00%	7.13	6.45E-13	3	241	0.9779
B0.00%	3.36	3.53E-13	3	219	0.9781
C0.00%	4.82	4.30E-13	3	248	0.9789
AVG 0.00%	**5.11**	**4.76E-13**	**3**	**236**	**0.9783**
A0.25%	8.91	6.17E-13	3	443	0.9843
B0.25%	7.10	9.27E-13	3	388	0.9705
C0.25%	7.34	5.05E-13	3	291	0.9901
AVG 0.25%	**7.78**	**6.83E-13**	**3**	**374**	**0.9816**
A0.50%	3.23	1.40E-12	3	311	0.9552
B0.50%	5.00	6.18E-12	3	529	0.9554
C0.50%	8.02	2.93E-12	3	436	0.9862
AVG 0.50%	**5.42**	**3.50E-12**	**3**	**425**	**0.9656**

Additionally, Fig. 4.19 depicts the trends of the relative change in the total electrical resistance of the sensors versus the applied strain. Trends of the three strain-sensing behavior equations retrieved for each formulation of smart bricks, whose terms were computed by considering the average value of the parameters estimated for each amount of steel fiber considered in this study, are also reported in the plots. It is worth noting that the strain range experienced by performing the electromechanical tests was used as input data in the series resistors model to obtain strain measurements of magnitudes comparable with those of the experimental trends. The obtained average coefficients of determination confirm that the proposed theoretical model satisfactorily fitted the experimental data after completing the calibration procedure. Even more important, Fig. 4.19 points out that the sensing capability at the contact electrodes, as well as that due to the intrinsic piezoresistivity of smart bricks, can be improved by increasing the content of steel fibers within the clay matrices.

Overall, the obtained results proved that the series resistors model theoretically proposed in this work can be used for describing the strain-sensing behavior of smart bricks under compression loads. Besides, results also demonstrated that both smart bricks made of 0.25% and 0.50% of steel fibers, possessing similar enhanced sensing capabilities, can be employed for monitoring strain in masonry constructions. Therefore, from an electromechanical point of view, the choice between these two formulations only depends on the

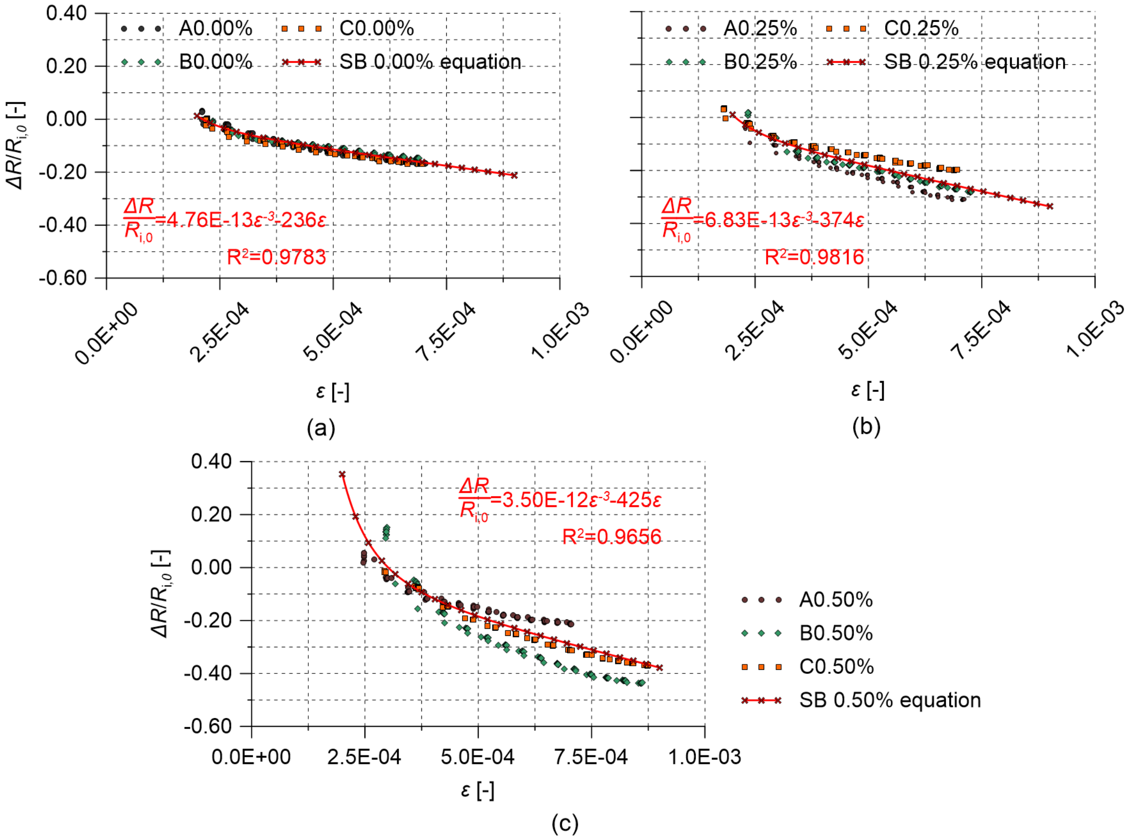

Figure 4.19: Relative change in the total electrical resistance of smart bricks versus the applied strain measured in the investigated compressive range (from 0.30 MPa to 4 MPa): (a) Plain samples; (b) Samples made of 0.25% of steel fibers; (c) Samples made of 0.50% of steel fibers.

demanded strain sensitivity.

For the sake of completeness, an example of application of the two-step calibration procedure on a smart brick of standard dimensions of 250x120x55 mm^3, made with a content of steel fibers equal to 0.25% according to the manufacturing process in Section 4.2.1, is reported in Fig. 4.20. In particular, Fig. 4.20(b) shows the time history of the total electrical resistance outputted by the tested sensor, pointing out its non-linear electrical response in correspondence of small values of compression load. As demonstrated for smart bricks produced in smaller sizes, the electrical response of the tested sensor became linear at relatively high compressive states (see Fig. 4.20(c)). Overall, the series resistors model is still effective for describing the electromechanical behavior of smart bricks of standard dimensions, as shown in Fig. 4.20(d).

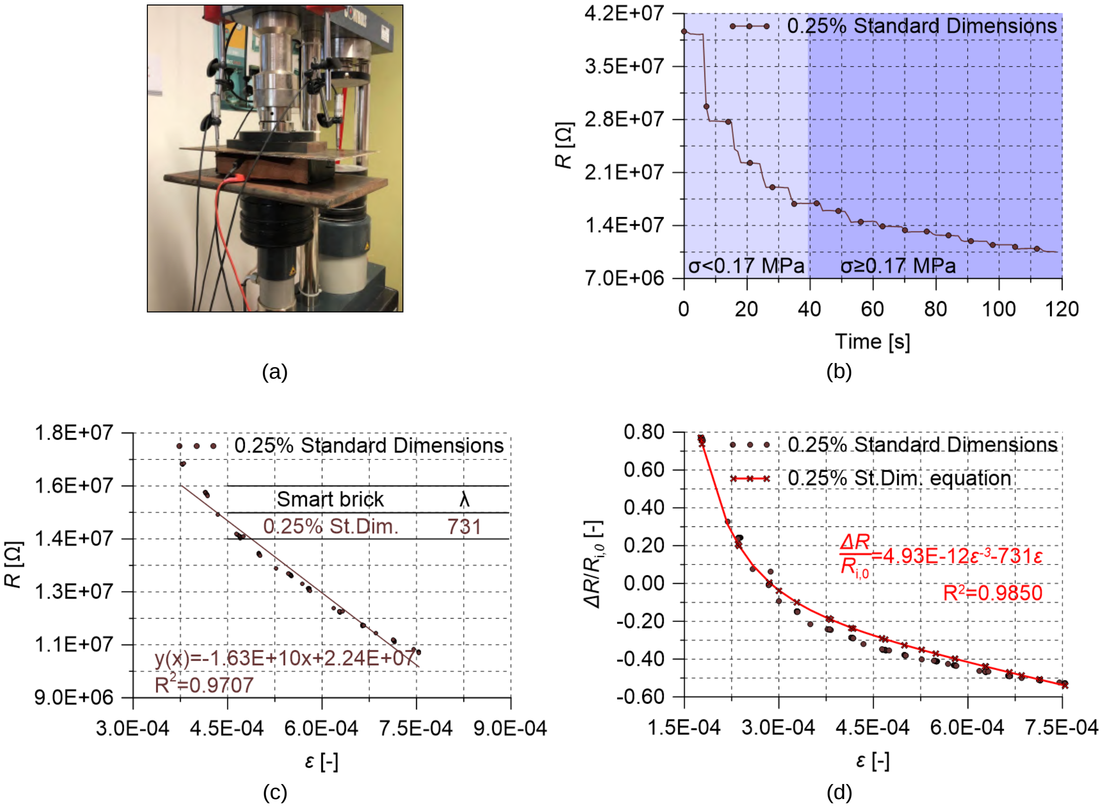

(a) (b)

(c) (d)

Figure 4.20: Results from the two-step calibration procedure applied on a smart brick of standard dimensions made with a content of steel fibers equal to 0.25%: (a) Laboratory setup of testing; (b) Time history of the total electrical resistance; (c) Linear regression analysis on data of the total electrical resistance and applied strain acquired at relatively high compressive states; (d) Curve fitting procedure on data of the relative change in the total electrical resistance and applied strain acquired in the whole compressive range.

4.4.2.2 Effectiveness of smart bricks in strain measurements

Smart bricks made with a content of stainless steel microfibers of 0.50%, with respect to the weight of fresh clay, were subjected to increasing axial compression loads to prove their effectiveness in measuring strain by comparing their outputs against those provided by couples of RSGs adhered onto their outer surfaces. Table 4.3 collects parameters of Eq. (4.10) obtained by performing the calibration procedure described in Section 4.3.2.1 and utilized for the post-processing of the electrical outputs from smart bricks to retrieve their strain measurements.

These are reported in Fig. 4.21, along with the outputs provided by RSGs and LVDTs. The novel sensors clearly detected the application of the load history by outputting an increase

Table 4.3: Results obtained from the experimental characterization of the strain-sensing behavior of smart bricks made with 0.50% of steel fibers: $R_{\mathrm{i},0}$ is the unstrained internal electrical resistance of the smart brick, a' is the relative sensing at the contact resistance, b is the contact resistance exponential term, λ is the gauge factor, and R^2 is the coefficient of determination of the curve-fitting.

Sample	$R_{\mathrm{i},0}$ [MΩ]	a'	b	λ	R^2
SB 0.50% A	5.80	6.86E-12	3	363	0.9815
SB 0.50% B	9.55	1.44E-11	3	412	0.9465
SB 0.50% D	15.9	3.40E-12	3	331	0.9527

in their compressive strain state at each load increment. Although measurements provided by the compared sensing technologies are consistent, the outputs from smart bricks are characterized by a noteworthy non-linear trend showing that non-constant changes in strain measured by the smart bricks corresponded to linear increments in the applied loads. This mechanical response is attributable to the ability of the novel sensors to take into account the non-linear mechanical behavior commonly exhibited by the conventional clay brick when strained in compression. In particular, this behavior is induced by the settlements that occurred in the internal macroporosity of the material. Indeed, as also confirmed by scanning samples of smart bricks with the CT technique as proposed in Section 4.3.3.1, the novel sensors, as well as the conventional clay bricks, are made of a porous material that when linearly stressed in compression presents non-constant settlements leading to non-linear variations in strain. Therefore, the outputs from smart bricks varied constantly according to the linear increase in the applied load only once settlements of the macropores of their internal structure stabilized by increasing the compression acting on the novel sensors. A similar behavior can be also observed in the outputs from LVDTs, which are affected by a non-linear trend comparable to that of smart bricks in correspondence of the first application of the compression load. Fig. 4.22 puts in relation measurements gathered from smart bricks and their corresponding couple of RSGs, highlighting differences in their strain-sensing behavior through a marked drift from the plotted ideal trend that outlines an equal response of the sensing technologies to the increasing compression.

An estimate of the non-linearity taken into account by the compared sensing technologies is provided in Fig. 4.23, which shows load-strain curves according to the outputs provided by smart bricks and RSGs. Reported trends were fitted by carrying out linear regression analysis and the Mean Absolute Error (MAE) was adopted to quantify the non-linearity of the responses of the sensors. The obtained results confirm that smart bricks, presenting the highest values of the MAE, are capable of providing a more accurate estimate of the applied

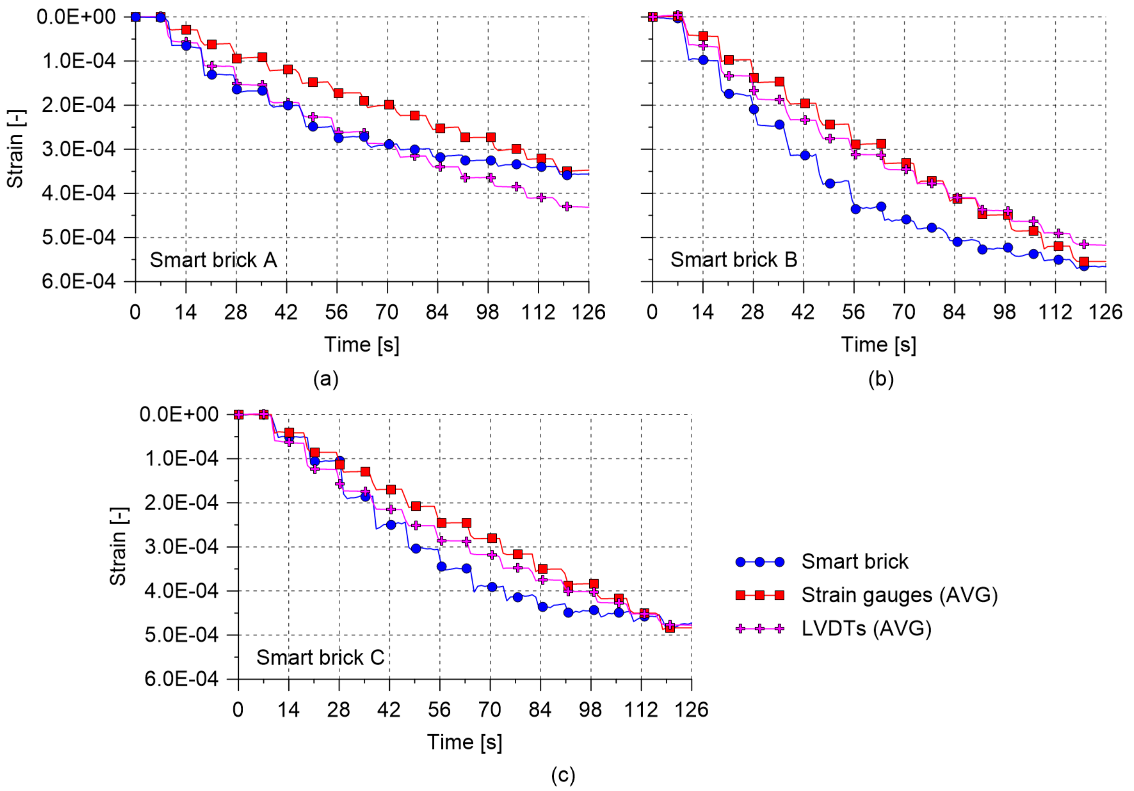

Figure 4.21: Comparison among the strain outputs provided by the tested smart bricks, their corresponding couples of RSGs, and the LVDTs, for which the average (AVG) strain is plotted: (a) Measurements obtained by testing smart brick A; (b) Measurements obtained by testing smart brick B; (c) Measurements obtained by testing smart brick C.

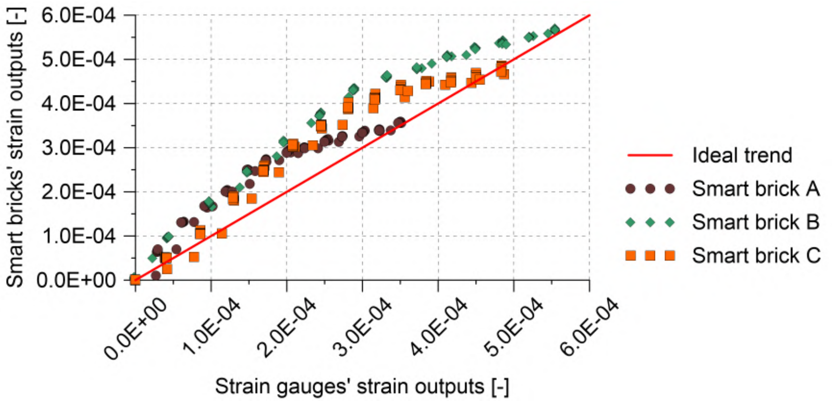

Figure 4.22: Strain outputs provided by the tested smart bricks versus the average strain measured by the corresponding couples of RSGs. The plotted ideal trend would outline an equal strain-sensing behavior between the compared sensing technologies.

strain since their outputs include such a non-linear response intrinsic of the material. On the contrary, RSGs hardly can take into account the macroporosity of the bricks and its influence in the response under compression, since their measurements are referred only to a small external portion of the surfaces of the samples. Overall, the presented study proved that smart bricks can be more effective than RSGs for monitoring strain in masonry constructions under increasing axial compression loads.

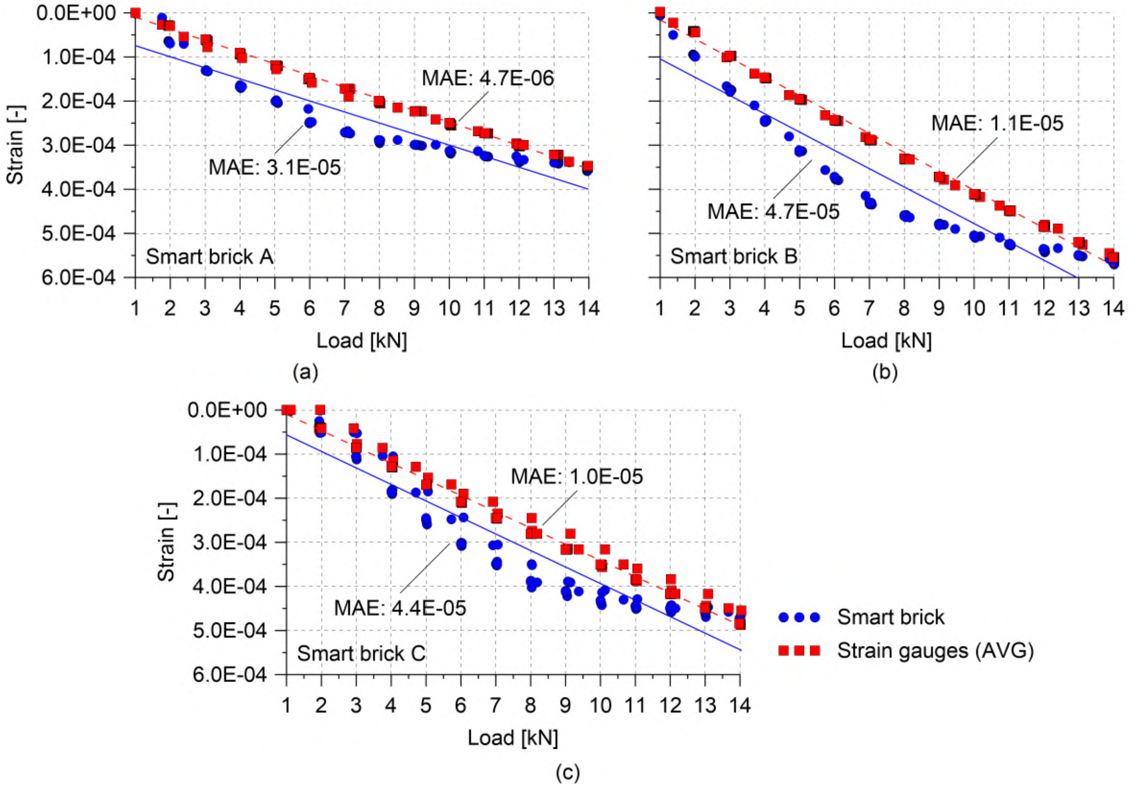

Figure 4.23: Load-strain curves with annotated the values of the Mean Absolute Error (MAE) obtained for the tested smart bricks and their corresponding couples of RSGs, for which the average (AVG) strain is considered: (a) Measurements obtained by testing smart brick A; (b) Measurements obtained by testing smart brick B; (c) Measurements obtained by testing smart bricks C.

4.4.3 Physical and mechanical properties

Results achieved by examining smart bricks with the CT scan technique, along with those obtained by subjecting samples of brick to compression and three-point bending tests are reported below.

4.4.3.1 Computed tomography scan

CT scans were performed on samples drilled from smart bricks made of 0.25% and 0.50% of stainless steel microfibers, with respect to the weight of fresh clay, to examine their internal structure by assessing the dispersion of the filler within the clay matrices. Obtained results were also compared with those from the scans of a sample retrieved from a plain brick. Fig. 4.24(a) reports pictures of the 3D volume of each cylindrical sample allowing the visual assessment of the densest constituents of the clay matrices, i.e. steel fibers and metallic inclusions randomly distributed within the reference volumes. It is worth noting that, the unsystematic connectivity observable between both constituents made challenging the statistical quantification of the well-dispersed steel fibers inside each scanned sample. In light of that, five 2D horizontal projections were analyzed for each scanned cylindrical sample by carrying out the statistical quantification of the dispersion of the filler, at a first level of approximation, through the evaluation of the bright single pixels contained within each 2D scan. It should be noted that to illustrate results obtained from the performed CT scans avoiding redundant information, only the pictures of the 2D middle projections of the samples are hereinafter discussed. In particular, Fig. 4.24(b) shows the 2D scans of each cylindrical sample with pixels of an intensity value between 13709 and 65535. Herein, darken colors denote the intrinsic internal macroporosity, which is typical of the clay-based materials (Mooney 2002), while colors from gray to white point out constituents capable of X-ray attenuation according to an increasing density. Steel fibers and metallic inclusions, being the densest components within the scanned samples, were highlighted in Fig. 4.24(c) by further adjusting the pixel intensity value with a lower and an upper bound of 65470 and 65535, respectively. Clustered pixels representing metallic inclusions were subsequently removed from the 2D projections, as shown by Fig. 4.24(d), through the application of the custom Python procedure previously introduced in Section 4.3.3.1.

The average number of bright single pixels detected for each examined cylindrical sample is reported in Fig. 4.25(a), which also shows the trend obtained by carrying out a linear regression analysis on the plotted data. The assessment of the coefficient of determination of the fitting, which is equal to 0.9882, suggests that the average number of bright single pixels, i.e. well-dispersed steel fibers, detected within the samples linearly increased with the content of filler adopted for producing the investigated sample. It should be noted that a small number of single pixels were still detectable within the projections of the plain sample due to the presence of residual pixels of metallic inclusions of small size that were not completely removed by the applied procedure. Considering that metallic inclusions of small size were reasonably present also in the post-processed scans of the doped matrices,

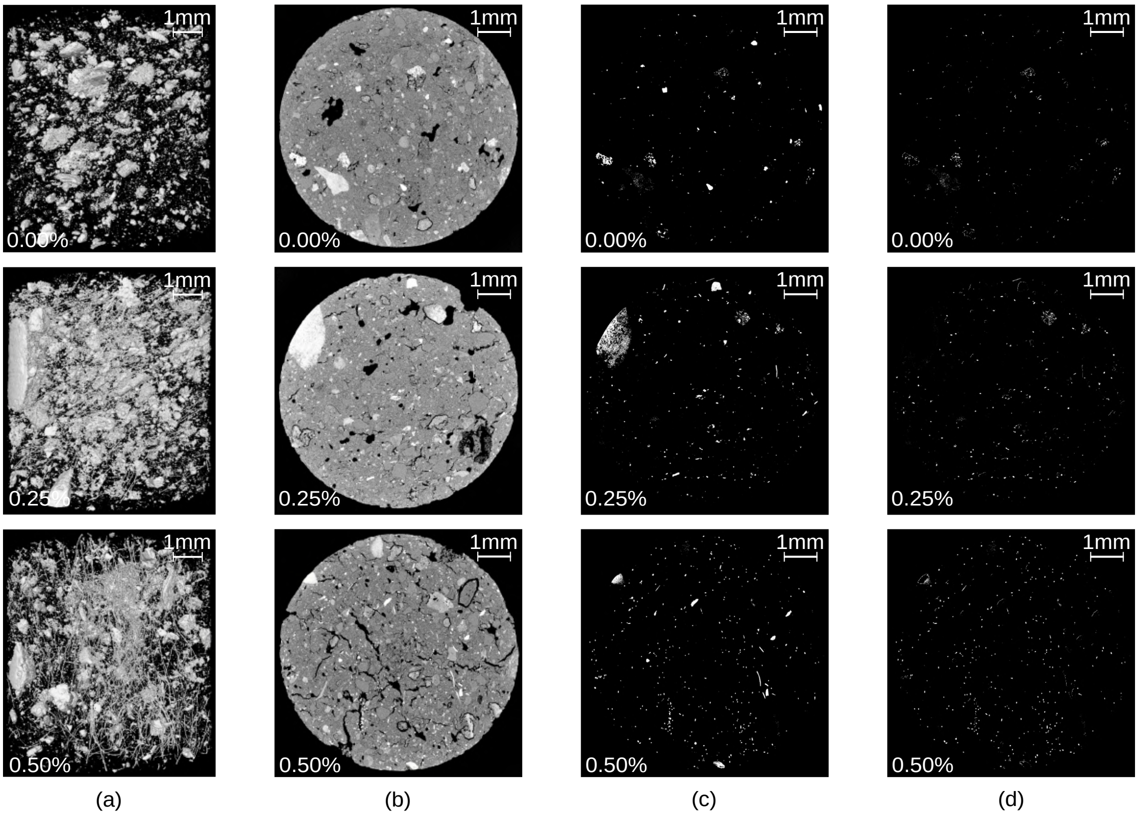

Fig. 4.24: Results obtained by carrying out CT scans on smart bricks made with different contents of stainless steel microfibers: (a) Pictures of the 3D volumes reconstructed by scanning cylindrical samples; (b) Grayscale pictures of the 2D middle horizontal projections with a pixel intensity value between 13709 and 65535; (c) Pictures of the 2D middle horizontal projections with a pixel intensity value between 65470 and 65535; (d) Pictures of 2D middle horizontal projections after the post-processing in Python environment.

the value of the intercept of the regression model, of about 86 pixels, can be assumed as the average number of bright single pixels statistically present within each examined sample and representing metallic inclusions of small size. Fig. 4.25(b) reports the trend of the distribution index computed for each formulation of smart bricks. According to its increasing values, the dispersion of the steel fibers within the samples improved by increasing the amount of filler used for producing the sensors. Due to the variability of steel fibers detectable within the scans of the doped samples, the latter are characterized by a marked standard deviation compared to that computed for the plain material, whose number of pixels identified within its projections was reasonably more uniform since only due to metallic inclusions. Overall, the obtained results demonstrated that the internal macro-porous structure of the smart bricks is similar to that of the conventional clay bricks. Results also pointed out that by increasing the amount of steel fibers used during the manufacturing process of the novel sensors, a more uniform distribution of the filler within the clay matrices can be achieved, hence more homogeneous composite materials can be obtained. Such a feature can be particularly relevant since the more homogeneous the distribution of the steel fibers the more the electrical/electromechanical response of the smart bricks is uniform.

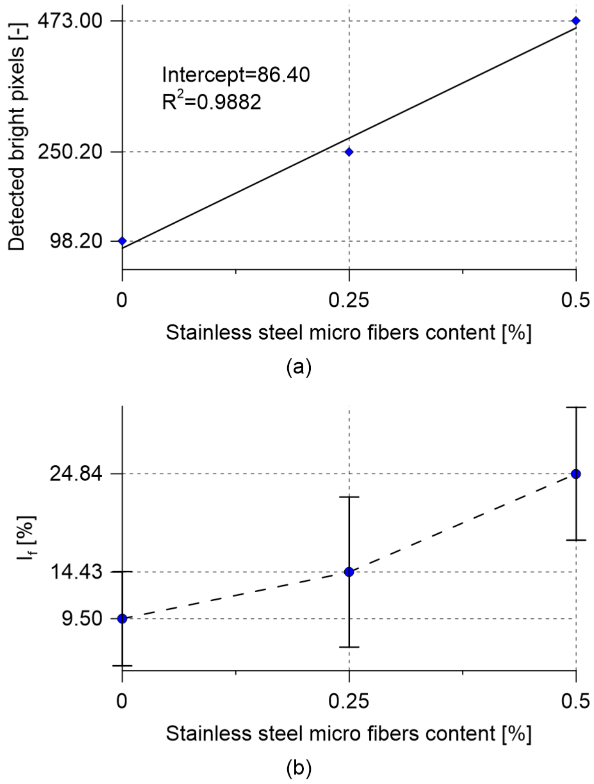

(a)

(b)

Fig. 4.25: Results obtained by carrying out CT scans on smart bricks made with different contents of stainless steel microfibers: (a) Average number of detected bright single pixels versus the content of steel fibers dispersed within the scanned samples; (b) Trend of the average distribution index versus the content of steel fibers dispersed within the scanned samples.

4.4.3.2 Compression tests

Table 4.4 collects values of the secant elastic modulus and the compressive strength determined for plain bricks and smart bricks made of a content of stainless steel microfibers of 0.25% and 0.50%, with respect to the weight of fresh clay, respectively. Due to the variability in the obtained values, Tukey's method was considered for identifying outliers within each data set. Accordingly, upper and lower thresholds were defined by exploiting the interquartile range, taking into account a value equal to one of the non-negative constant k for their computation. Values exceeded thresholds were therefore identified as outliers. It is worth noting that a more restrictive value of k (usually, $k = 1.5$, here $k = 1.0$) was considered due to the small dimension of the data set. Outliers detected with such a methodology were however retained avoiding reducing the dimension of the data set, nevertheless, median values of the investigated mechanical properties were considered since less influenced by data scattering. The obtained results show that a progressive increase in the amount of steel fibers dispersed within the clay matrices produced a slight increase in the elastic modulus and a moderate decrease in compressive strength compared to the median values computed for the plain bricks. An increase in the content of steel fibers from 0.25% to 0.50% resulted in a modest decrease in the median value of the elastic modulus. Overall, the performed experiments demonstrated that smart bricks made with an amount of steel fibers equal to 0.25% and 0.50% possess mechanical properties comparable to those of the conventional clay bricks. In light of that, the novel sensors can be fully integrated within a masonry construction for monitoring strain without interfering with its global/local structural response.

4.4.3.3 Three-point bending tests

Table 4.5 collects values of the fracture energy for the opening mode of fracture determined for samples of plain bricks and smart bricks made of a content of stainless steel microfibers of 0.25% and 0.50%, with respect to the weight of fresh clay, respectively. Possible outliers within the data set were identified by adopting Tukey's method, as explained in the previous section. Even in this case, although the scattering in the data set is limited since only a few samples are laying outside the computed Tukey's thresholds, the comparison between the investigated formulations of smart bricks was carried out maintaining all the measurements in the experimental data set and by considering the median values of the fracture energy. Results show that samples doped with an amount of steel fibers equal to 0.25% possess a moderately higher median fracture energy than the plain material, while a further increase in the content of conductive filler, from 0.25% to 0.50%, produced instead a decrease in fracture energy compared to that found for plain samples. Overall, results achieved in that study demonstrated that the addition of steel fibers to the clay matrices results in minimum modifications of the fracture energy for the opening of fracture compared to that

Table 4.4: Secant elastic modulus and compressive strength determined by performing compression tests on plain bricks and smart bricks made with a content of stainless steel micro fibers equal to 0.25% and 0.50%. Computed median (MED) values are annotated for each investigated formulation of smart bricks.

Sample	Secant elastic modulus [MPa]	Compressive strength [MPa]
A 0.00%	4015	15
B 0.00%	3275	11
C 0.00%	3201	10
D 0.00%	12208	13
E 0.00%	2365	11
MED 0.00%	**3275**	**11**
A 0.25%	4356	9
B 0.25%	7013	9
C 0.25%	12730	8
D 0.25%	5194	11
E 0.25%	5882	14
MED 0.25%	**5882**	**9**
A 0.50%	8913	8
B 0.50%	4559	9
C 0.50%	12545	9
D 0.50%	4447	9
E 0.50%	4662	9
MED 0.50%	**4662**	**9**

of the plain material. Once again, the assumption that smart bricks possess mechanical properties similar to that of the conventional clay bricks is proven.

4.4.4 Environmental effects on the electrical outputs of the smart bricks

Experiments for the investigation on the influence of the environmental effects, due to changes in temperature and humidity, on the electrical outputs of the smart bricks were conducted by testing masonry subassemblies under outdoor climatic conditions. Fig. 4.26 shows the results obtained by testing the structural setting equipped with a smart brick made of 0.25% of stainless steel microfibers with respect to the weight of fresh clay.

In particular, the hourly trends of the total electrical resistance, temperature, and relative humidity are plotted in the picture along with the correlation matrix collecting the coefficients of correlation computed between the considered data sets. At a first glance, it is possible to note that the total electrical resistance of the tested smart brick is negatively correlated with the temperature and positively correlated with the relative humidity. This

Table 4.5: Fracture energy values determined by performing three-point bending tests on samples of plain bricks and smart bricks made with a content of stainless steel micro fibers equal to 0.25% and 0.50%. Computed median (MED) values are annotated for each investigated formulation of smart bricks.

Sample	Fracture Energy [N/mm]	Sample	Fracture Energy [N/mm]
A 0.00%	0.38	A 0.50%	0.38
B 0.00%	0.42	B 0.50%	0.40
C 0.00%	0.40	C 0.50%	0.37
D 0.00%	0.40	D 0.50%	0.39
E 0.00%	0.36	E 0.50%	0.38
F 0.00%	0.40	F 0.50%	0.39
MED 0.00%	**0.40**	**MED 0.50%**	**0.39**
A 0.25%	0.42		
B 0.25%	0.37		
C 0.25%	0.42		
D 0.25%	0.43		
E 0.25%	0.43		
F 0.25%	0.42		
MED 0.25%	**0.42**		

means that an increase in the electrical outputs of the novel sensor corresponded to a reduction in the values of the temperature and an increase in the trend of the humidity. Considering the correlation between the temperature and the total electrical resistance, smart bricks show the typical behavior characterizing the insulating materials when exposed to changes in temperature, i.e. the electrical resistance of the insulator decreases by increasing the temperature. This appears reasonable, especially by taking into account that, although smart bricks made of 0.25% of steel fibers possess improved electrical properties than those of plain bricks, they are still characterized by high values of the electrical resistance. The phenomenon can be explained by considering what happens at the atomic level within a heated insulator: The flow of the current within a material is due to the movement of electrons from one atom to another under the influence of an electric field. Materials defined as insulators possess a very limited number of free electrons than conductive materials, hence, their conductivity is much lower. Heating a material induces vibrations in its atoms, which tend to free electrons. In this circumstance, freed electrons significantly contribute to increase the current flow especially in the case of insulating materials, resulting in a noticeable increase in their conductivity, and therefore in a measurable reduction in their electrical resistance (Ward 1971). A more careful assessment of the positive correlation between the total electrical resistance and the relative humidity leads to

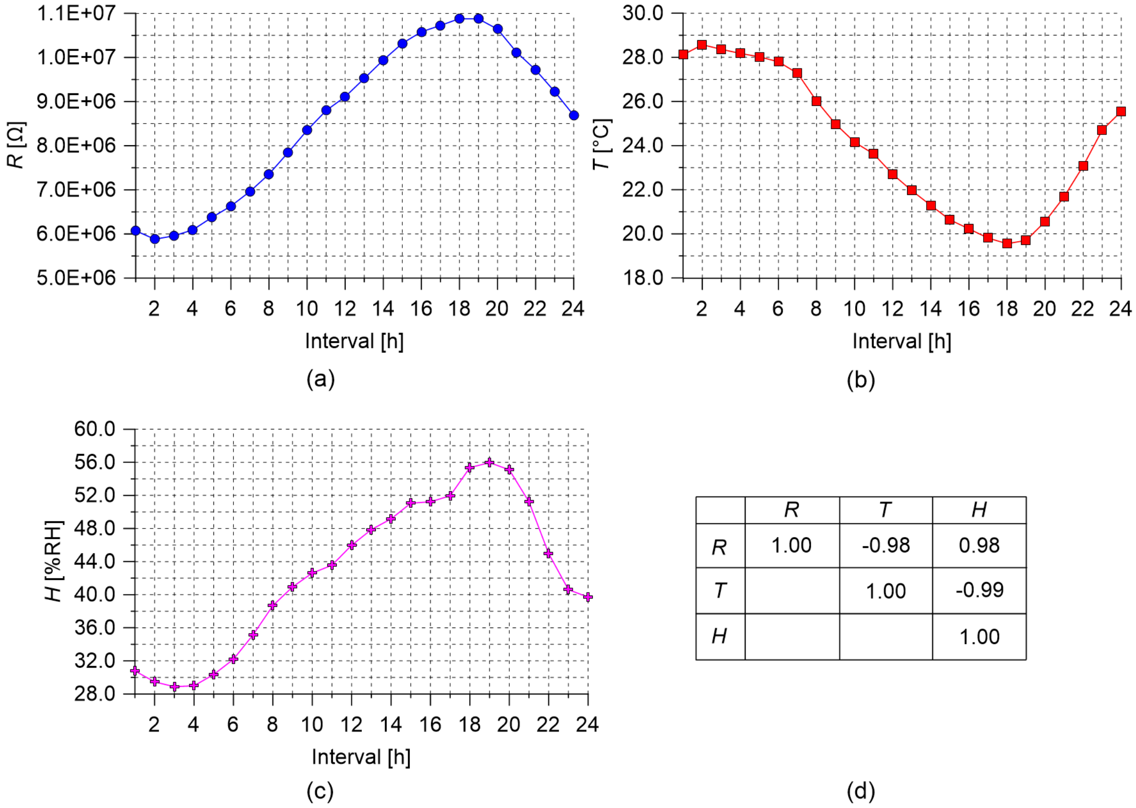

	R	*T*	*H*
R	1.00	-0.98	0.98
T		1.00	-0.99
H			1.00

(d)

Fig. 4.26: Results obtained by carrying out tests on masonry subassemblies for the investigation on the environmental effects on the electrical outputs of the smart bricks: (a) Hourly trend of the total electrical resistance acquired from the smart brick made with a content of stainless steel microfibers equal to 0.25 %; (b) Hourly trend of the temperature; (c) Hourly trend of the relative humidity; (d) Correlation matrix.

the conclusion that the influence of the changes in humidity on the electrical outputs of the smart bricks is secondary to the contribution of the temperature. This can be affirmed since, in principle, an increase in the humidity should result in a decrease in the values of the total electrical resistance of the novel sensor and not the contrary, as experienced. Conceivably, changes in the relative humidity influences the electrical outputs of the smart bricks only if the value of the relative humidity remains stable for a period equal to or longer than the time required by the water particles to infiltrate within the internal macroporous structure of the bricks. The hourly trend of the humidity is however characterized by a perfect agreement with the recorded changes in the temperature, as also confirmed by the strong negative correlation linking these two environmental parameters. Fig. 4.27 reports the results obtained by testing the subassembly equipped with a conventional clay brick turned into a sensor. The assessment of the correlation matrix demonstrates that conventional clay bricks and smart bricks react in the same way to the changes in temperature. These also influenced the trend of the relative humidity as previously discussed.

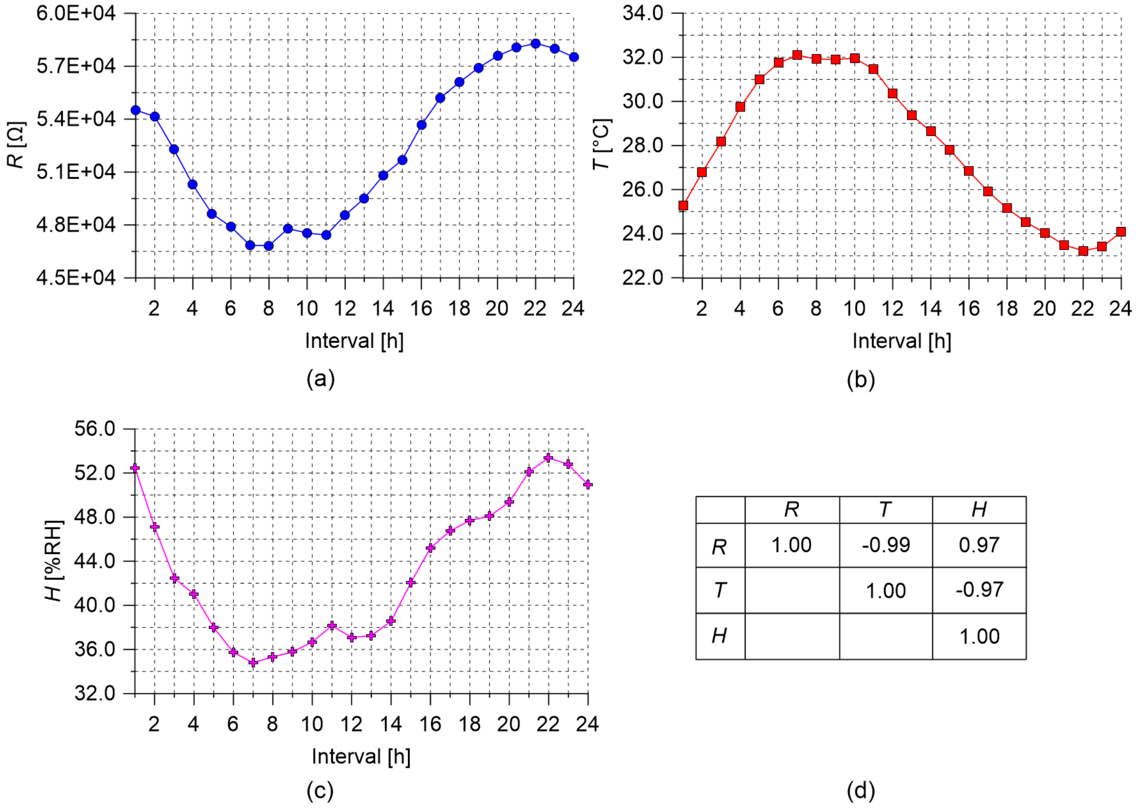

(a)

(b)

(c)

	R	*T*	*H*
R	1.00	-0.99	0.97
T		1.00	-0.97
H			1.00

(d)

Fig. 4.27: Results obtained by carrying out tests on masonry subassemblies for the investigation on the environmental effects on the electrical outputs of the smart bricks: (a) Hourly trend of the total electrical resistance acquired from the conventional clay brick turned into a sensor; (b) Hourly trend of the temperature; (c) Hourly trend of the relative humidity; (d) Correlation matrix.

The effects of the changes in temperature were removed from the trends of the total electrical resistance by leveraging on the linear correlation, shown in Fig. 4.28, between these two parameters. In particular, Fig. 4.29(a) illustrates the effectiveness of the linear regressive model in predicting the trend of the electrical output of the tested smart brick according to the recorded temperature data. The high value of the coefficient of correlation confirms the good fit between the regressive model and the experimental data, with the consequence that the computed residuals are of small magnitude. Similar results were found for the conventional clay brick turned into a sensor, as depicted in Fig. 4.29(b). Overall, experiments demonstrated that daily changes in temperature affect the total electrical resistance of the smart bricks. However, these effects can be easily removed from the trend of the electrical outputs of the novel sensors. A broader training period is necessary to properly calibrate the regressive model for monitoring purposes.

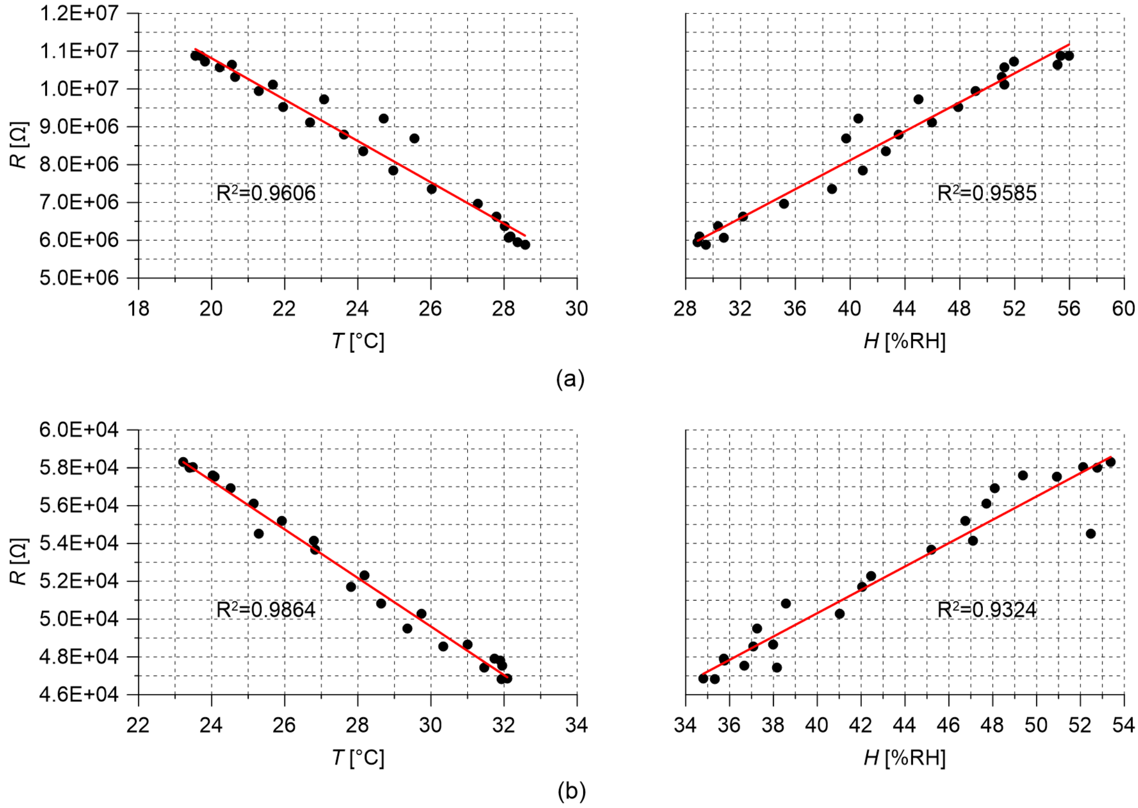

Fig. 4.28: Results obtained by carrying out tests on masonry subassemblies for the investigation on the environmental effects on the electrical outputs of the smart bricks: (a) Linear regression analyses carried out on data of the total electrical resistance, acquired from the smart brick made with a content of stainless steel microfibers equal to 0.25 %, versus temperature and relative humidity; (b) Linear regression analyses carried out on data of the total electrical resistance, acquired from the conventional clay brick turned into a sensor, versus temperature and relative humidity.

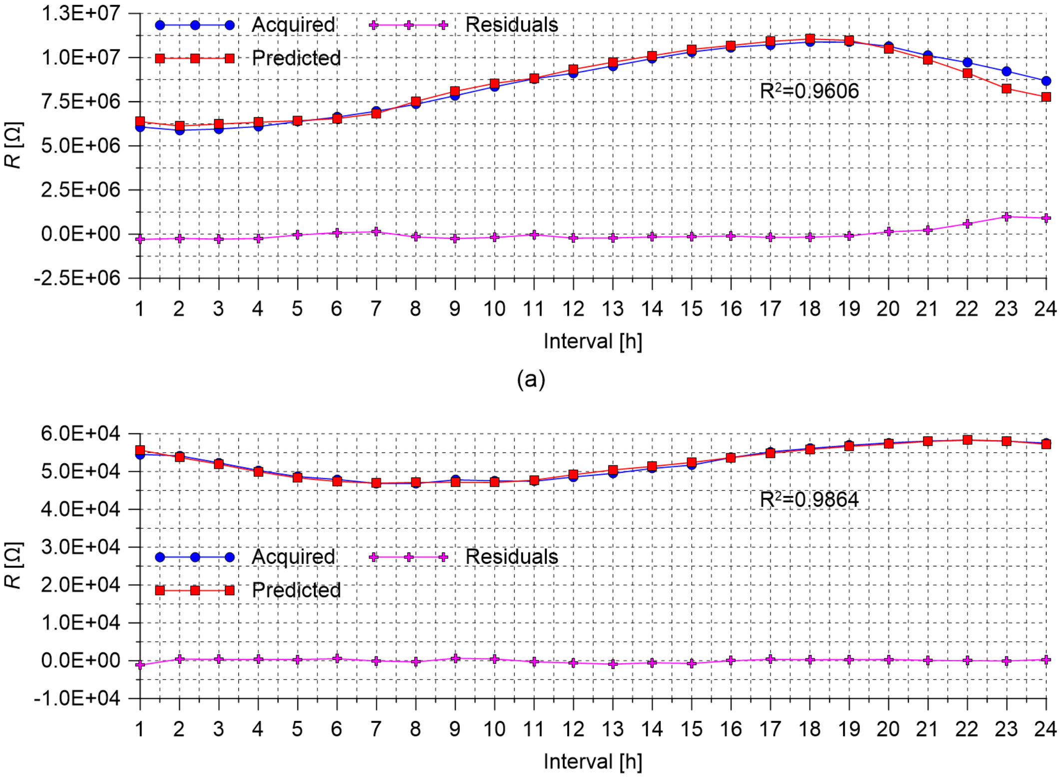

(a)

(b)

Fig. 4.29: Results obtained by carrying out tests on masonry subassemblies for the investigation on the environmental effects on the electrical outputs of the smart bricks: (a) Temperature compensation on the electrical outputs acquired from the tested smart brick; (b) Temperature compensation on the electrical outputs acquired from the tested conventional clay brick turned into a sensor.

4.5 Closing remarks

This chapter introduced novelties concerning the development of the smart brick technology, whose state-of-the-art is reviewed in Chapter 2. This innovative sensing solution for SHM of masonry constructions involves a new class of durable brick-like sensors obtained by doping fresh clay with stainless steel microfibers to improve the strain-sensing capabilities of the clay-based material. Exploiting their enhanced piezoresistivity, smart bricks are capable of providing measurable changes in their electrical resistance when strained in compression, which can be exploited for monitoring purposes if correlated, by means of a suited electromechanical model, to the changes in the compressive strain state of the sensors. Envisioning a monitoring system involving smart bricks, these can be therefore fully integrated within masonry structural elements enabling the automated revealing of modifications in their strain field, which can lead to the detection and localization of the developing damages, including those due to earthquake loading.

Stainless steel microfibers were selected as the suitable conductive filler to boost the electrical and electromechanical properties of the novel sensors due to their heat resistance and their high electrical conductivity. The use of this filler, as well as the use of the external copper plate electrodes to conduct electrical measurements, represent the first novelties introduced in the smart brick technology by this work.

A further step forward concerns the definition of a brand-new electromechanical model, called series resistors model, describing the strain-sensing behavior of the novel sensors under the application of compression loads, which once calibrated permits to retrieve strain measurements through the post-processing of the electrical outputs from the smart bricks. First of all, experiments were conducted to investigate the electrical behavior of smart bricks as the content of steel fibers dispersed within the clay matrices increases. Achieved results demonstrated that the addition of steel fibers to the clay-based material markedly improve its electrical properties. The percolative behavior of the novel sensors was also evaluated. This is characterized by a double percolation threshold, a feature that was exploited in this work to optimize the manufacturing process of the smart bricks by selecting the first percolation threshold as a reference for conducting investigations on their electromechanical, physical, and mechanical properties.

In particular, electromechanical tests were carried out to validate the series resistors model, allowing its experimental characterization according to the amount of conductive filler used for the production of the novel sensors. The obtained results confirmed the effectiveness of the innovative electromechanical model proposed for strain estimation, also demonstrating that the addition of the steel fibers to the clay-based material greatly improves its piezoresistivity, as well as the sensing at the electrodes of the smart bricks. The effectiveness of the novel sensors in measuring strain under increasing compression loads was proved by comparing their outputs against those provided by RSGs adhered to their external surfaces. In this case, the achieved results highlighted the intrinsic capability of the smart bricks in providing strain measurements that take into account the non-linear mechanical response typically exhibited by the conventional clay bricks when stressed in compression. It should be noted how useful this feature can be while monitoring strain in a typical masonry structural setting.

CT scans were performed on samples of smart bricks made with different amounts of steel fibers to assess their physical properties investigating the quality of the dispersion of the conductive filler within the clay matrices. Experiments permitted to evaluate all the constituents within the doped material of which smart bricks are made of, pointing out the presence of numerous connections between the steel fibers and the metallic inclusions in the clay that allow the formation of further conductive paths internally to the composite material. The use of a distribution index in combination with a custom image-processing procedure also permitted to statistically characterize the dispersion of the steel fibers within the scanned volumes at a first level of approximation. As main result, these experiments demonstrated that smart bricks possess an internal structure similar to that of the conventional clay bricks.

Compression and three-point bending tests were carried out to study the influence of the conductive filler in the mechanical properties of the smart bricks. In particular, the elastic modulus, the compressive strength, and the fracture energy for the opening mode of fracture were assessed. The obtained results demonstrated that a content of filler equal to 0.25% or 0.50% can be added to the clay matrices without altering the mechanical response of the bricks neither in compression nor in bending.

Masonry subassemblies were tested under outdoor climatic conditions to study the environmental effects, due to the changes in temperature and relative humidity, on the electrical outputs of the smart bricks. The obtained results demonstrated that there is a strong negative correlation between the total electrical resistance of the novel sensors and the temperature, whereby the values of the electrical outputs of the smart bricks decrease as the temperature surges. Similar results were also obtained by testing a subassembly equipped with a conventional clay brick turned into a sensor. Based on the performed tests, therefore, changes in temperature faster influence the physical structure of the bricks than the changes in humidity. This because the particles of water dispersed in the air need time to enter within the pores of the material and alter its conductivity, while daily changes in humidity occurred much faster than this infiltration time. Experiments also proved how the effects of daily changes in temperature can be removed from the electrical outputs of the smart bricks by using a linear regressive model.

Overall, this chapter provided a comprehensive characterization of the smart bricks, demonstrating that these novel sensors, made by doping fresh clay with stainless steel microfibers, can be considered to all intents and purposes as a newly conceived sensing technology for seismic SHM of masonry constructions based on strain measurements. Fig. 4.30 reports a conceptual exemplification of the data sheet of a smart brick.

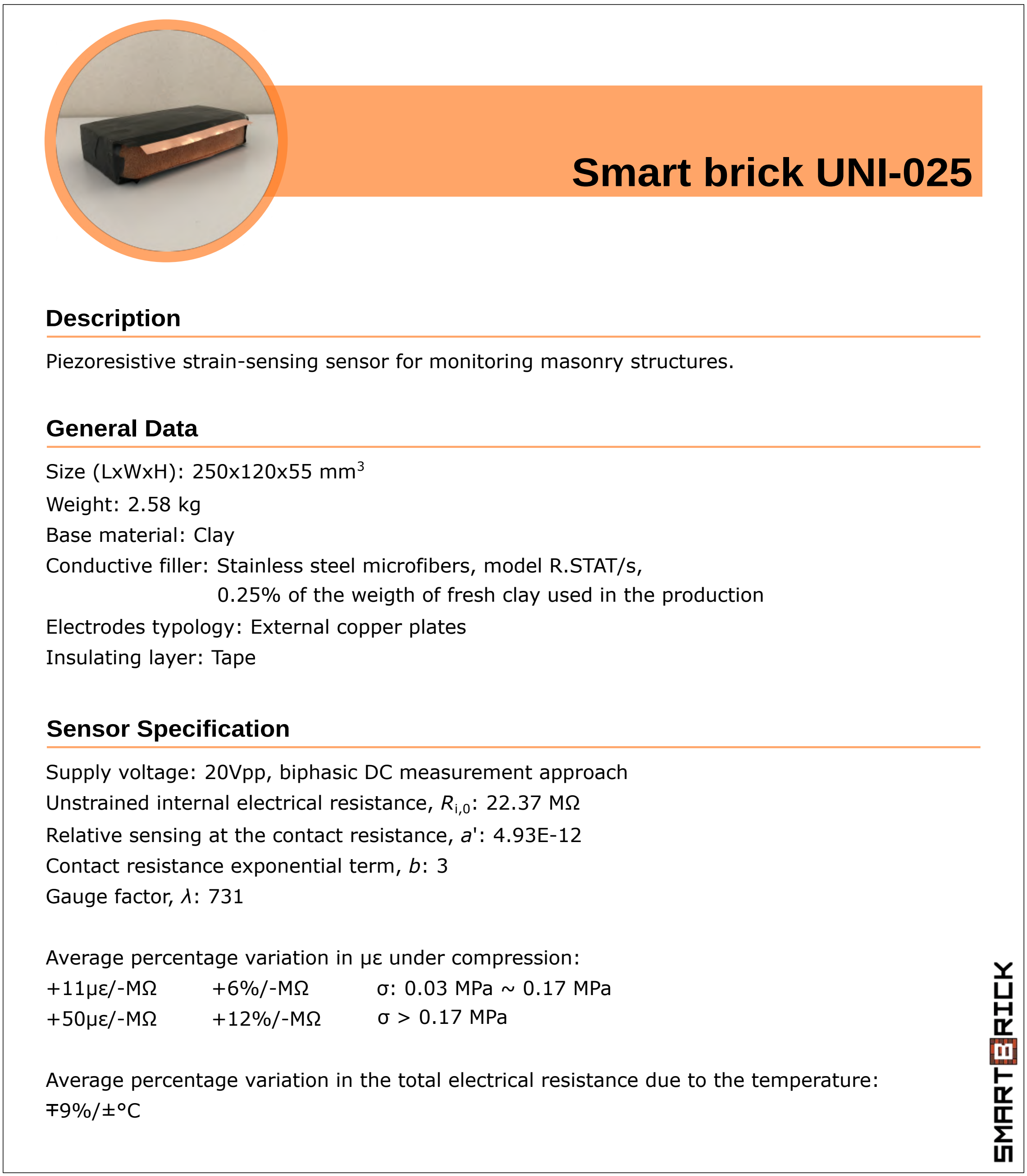

Smart brick UNI-025

Description

Piezoresistive strain-sensing sensor for monitoring masonry structures.

General Data

Size (LxWxH): 250x120x55 mm^3
Weight: 2.58 kg
Base material: Clay
Conductive filler: Stainless steel microfibers, model R.STAT/s,
0.25% of the weigth of fresh clay used in the production
Electrodes typology: External copper plates
Insulating layer: Tape

Sensor Specification

Supply voltage: 20Vpp, biphasic DC measurement approach
Unstrained internal electrical resistance, $R_{i,0}$: 22.37 MΩ
Relative sensing at the contact resistance, a': 4.93E-12
Contact resistance exponential term, b: 3
Gauge factor, λ: 731

Average percentage variation in με under compression:

+11με/-MΩ	+6%/-MΩ	σ: 0.03 MPa ~ 0.17 MPa
+50με/-MΩ	+12%/-MΩ	σ > 0.17 MPa

Average percentage variation in the total electrical resistance due to the temperature:
∓9%/±°C

Fig. 4.30: Conceptual exemplification of the data sheet of a smart brick.

Chapter 5

Applications of the smart brick technology

5.1 Introduction

Smart bricks are piezoresistive brick-like sensors representing an innovative sensing technology for SHM of masonry constructions. Their enhanced strain-sensing capabilities are based on the correlation between variations in their strain conditions and changes in their electrical outputs. In particular, an increase in the compressive strain state of a smart brick, caused by an increment in the compressive stress acting on it, results in a measurable decrease in its electrical resistance. Such an electromechanical behavior, developed through the addition of stainless steel microfibers to the clay matrices, can be exploited to reveal the internal load paths redistributions, induced by the development of damages, when smart bricks are embedded within masonry structural elements. Indeed, in principle, possessing physical and mechanical properties similar to those of the conventional clay bricks, the novel sensors can be deployed wherever within a masonry construction without altering its global/local structural response, thus overcoming most of the limiting factors shown by the off-the-shelf sensing technologies during their practical applications

(Fig. 5.1). After having thoroughly characterized the smart bricks in Chapter 4, some meaningful applications of these rising sensing devices are illustrated in this chapter, so as proving their effectiveness for SHM of full-scale masonry constructions with particular attention to the detection and localization of earthquake-induced damages.

The rest of the chapter is structured as follows. Section 5.2 illustrates proposals of damage detection and localization algorithms based on the post-processing of the strain measurements from smart bricks. Section 5.3 first reports the methodology adopted for the experimental validation of the series resistors model for retrieving strain measurements from smart bricks embedded within masonry structural elements. Later, meaningful case studies in which smart bricks are employed for monitoring the strain field in small- and full- scale masonry constructions are presented. Section 5.4 outlines the obtained results, while closing remarks and further comments are reported in Section 5.5.

Figure 5.1: Illustrations of the deployment of smart bricks of standard dimensions.

5.2 Proposal of damage detection and localization algorithms based on the strain measurements from smart bricks

Damage detection and localization in masonry constructions are currently challenging tasks of the utmost importance that demands continuous development in SHM techniques. In this regard, the smart brick technology appears as a promising alternative to the traditional SHM approaches commonly applied to masonry constructions since it exploits brick-like sensors strategically embeddable within the load-bearing structures, whose outputs can be post-processed allowing the assessment of modifications in the strain field of the monitored structural element, as well as the detection and localization of developing cracking patterns.

Envisioning the implementation of seismic systems based on the smart brick technology, strain measurements provided by the novel sensors can be post-processed according to two main strategies: a first approach, usable only in case of smart bricks deployed within dense sensor networks, consists in the post-processing of the strain measurements provided by the novel sensors through suitable spatial interpolation techniques thus enabling the reconstruction of the strain field in the structure being monitored. This approach permits to accurately point out critical areas characterized by strain concentrations/relaxations induced by the load paths redistributions that may occur internally to the construction at the formation of cracks. Therefore, in this case, damages developed on a structure can be located by means of the cross-comparison of the spatially interpolated strain measurements (5.2(a)). A second approach consists of comparing actual strain measurements provided by smart bricks with baseline data referring to a reference condition of the structure being monitored, for instance, when it was in a sound state. According to this technique, adoptable indifferently in the case of smart bricks deployed in both coarse and dense sensor networks, damages developed on a structure can be detected and located by assessing in time changes in strain revealed by each singular sensor (5.2(b)).

It is worth noting that this section is aimed only to provide a preliminary conceptualization of the use of smart bricks for strain monitoring purposes. The damage detection and localization strategies briefly proposed herein are later described in detail and applied in the case studies presented in the following sections. For the sake of clarity, it should be also noted that no temperature and humidity compensation was carried out in the proposed case studies since measurements from smart bricks were acquired within a limited time span in which environmental conditions were monitored and stable.

5.3 SHM applications: Methodology

This section reports the experimental and numerical methodologies adopted in the case studies proposed in this work to prove the effectiveness of the smart brick technology for monitoring strain in masonry constructions.

5.3.1 Validation of the series resistors model by testing a typical structural setting

The use of the series resistors model for retrieving strain measurements through the post-processing of the electrical outputs from smart bricks subjected to increasing compression loads was investigated in Chapter 4. Herein, before presenting meaningful applications of the smart brick technology, the series resistors model is experimentally validated prov-

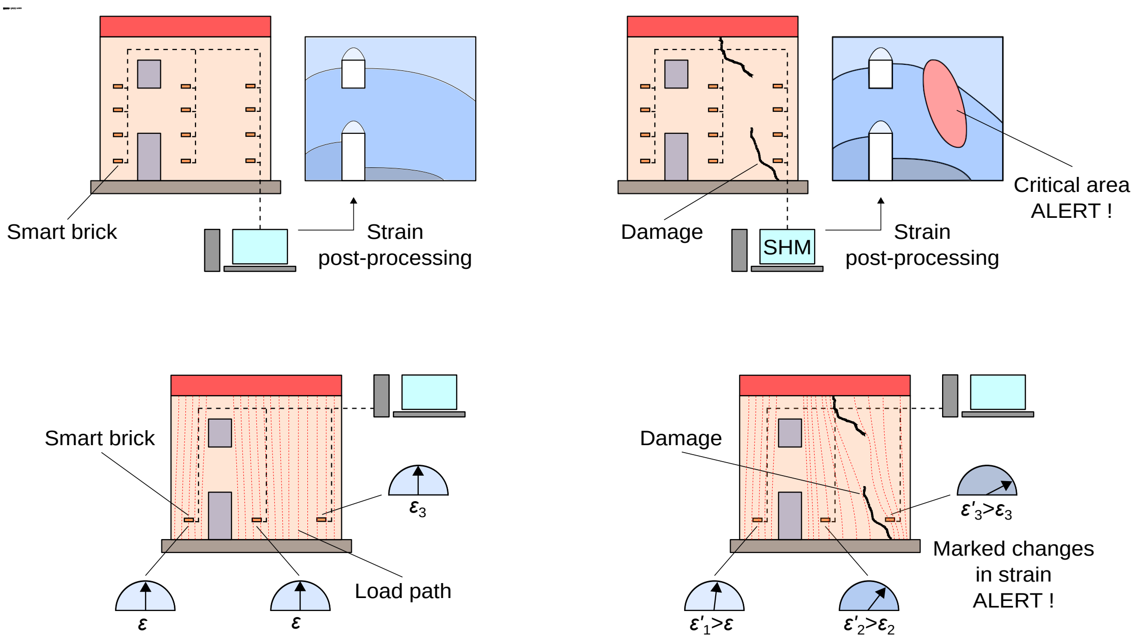

Figure 5.2: Conceptual exemplifications of SHM systems based on the smart brick technology: (a) Smart bricks deployed within a dense sensor network for the reconstruction of the strain field. Concentrations/relaxations detected in the strain distribution may be related to modifications in the load paths due to the development of cracks to the structure; (b) Smart bricks deployed within a coarse sensor network for monitoring permanent changes in strain (being ϵ the compressive strain measured from each embedded sensor). Marked changes in the strain measured by smart bricks may be related to modifications in the load paths due to the development of cracks to the structure.

ing its effectiveness in estimating strain when smart bricks are embedded within a typical structural setting. To do that, a small-scale masonry wall specimen of 370x50x390 mm^3 was subjected to eccentric axial compression loads of increasing intensity exemplifying a non-uniform redistribution of the dead loads on the structural element after an earthquake. Such a critical loading condition can be frequently observed in the case of masonry constructions designed without a proper box behavior, in which damages due to the ground motions induce unsymmetrical internal load paths redistributions that result in excessive loading on structural elements such as pier panels, vaults, and arches, which can lead to fragile collapse mechanisms if a second seismic event strikes the damaged construction after the main shake. The wall specimen, built and tested by exploiting the facilities of the Laboratory of Structural Dynamics of the University of Perugia (UniPg LabDyn), consisted of 28 plain bricks and 7 smart bricks, arranged in five columns and seven rows by using R3 class cement mortar joints of thickness of approximately 5 mm, as depicted in Fig. 5.3(a).

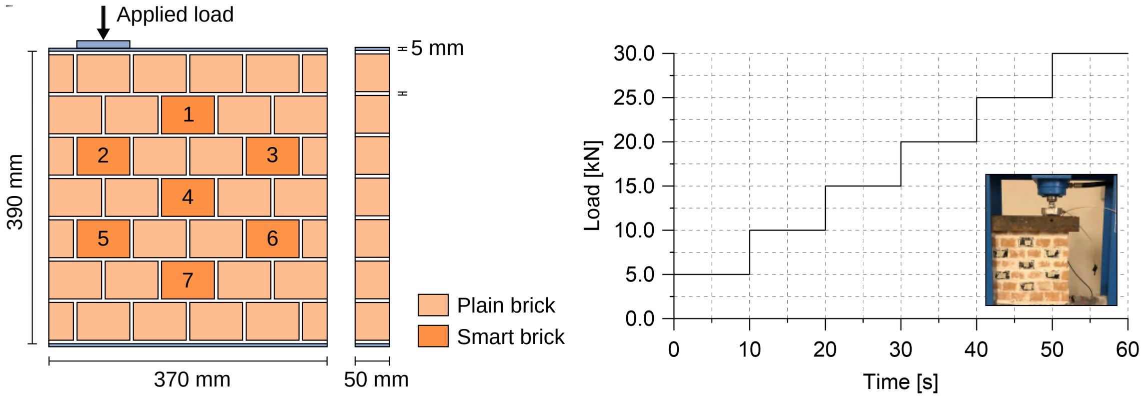

(a)

Figure 5.3: Electromechanical tests on a small-scale masonry wall specimen equipped with smart bricks made with a content of stainless steel microfibers equal to 0.25%: (a) Illustration of the tested wall specimen and smart bricks deployment; (b) Adopted load history and laboratory setup.

Smart bricks were manufactured according to the production process described in Section 4.2.1 by adopting a content of steel fibers equal to 0.25% and external copper plate electrodes to perform electrical measurements through the methodology reported in Section 4.2.2.1. Plain bricks were fabricated by following the same production process without the addition of any electrically conductive filler nor electrodes. Tests were conducted by first damaging the wall specimen through the application of a centered axial compression load, whose magnitude was increased up to the formation of a visually detectable cracking pattern. After that, the structural element was eccentrically stressed by applying the load history plotted in Fig. 5.3(b) on its left side considering a distance from its centerline of about 110 mm, hence maintaining each load step constant for 10 s allowing data gathering from the embedded smart bricks. The novel sensors were therefore employed for monitoring changes in strain due to the development of cracks in an existing cracking pattern. A hand-operated hydraulic press operating on a steel member of thickness of 5 mm, placed with a dry contact on the top of the wall, was used for load distribution. Strain measurements were retrieved by post-processing the total electrical resistance from smart bricks through Eq. (4.10) specialized according to the strain-sensing capabilities of bricks made of 0.25% of steel fibers by using the parameters collected in Table 5.1. These were determined by testing single smart bricks in Section 4.4.2.1 by following the calibration procedure illustrated in Section 4.3.2.1. Such a common set of parameters was considered since the employed smart bricks were not individually characterized before their embedding within the wall specimen. Strain estimation was carried out through the dedicated software "SHM-Smartbricks".

Table 5.1: Parameters of Eq. (4.10) adopted for retrieving strain measurements from smart bricks (0.25% of stainless steel microfibers) embedded within the small-scale masonry wall specimen: $R_{\mathrm{i},0}$ is the unstrained internal electrical resistance of the smart brick, a' is the relative sensing at the contact resistance, b is the contact resistance exponential term, and λ is the gauge factor.

Sample	$R_{\mathrm{i},0}$ [MΩ]	a'	b	λ
Embedded smart bricks	7.78	6.83E-13	3	374

5.3.2 Use of smart bricks deployed within a dense sensor network

Similarly to the first case study, the following application of the smart brick technology deals with a small-scale masonry wall specimen equipped with the novel sensors and eccentrically loaded in its plane. This time, however, the main objective of the investigation is to demonstrate the effectiveness of smart bricks for strain field reconstruction and damage detection and localization when embedded within a dense sensor network in masonry structural elements subjected to critical loading conditions caused by earthquake-induced damages. In particular, strain measurements provided by the novel sensors were compared with those outputted by RSGs directly attached on their outer surfaces. This was done to benchmark the outputs from smart bricks against those provided by one of the most widely adopted traditional devices for monitoring strain in masonry constructions during practical applications. Furthermore, a 3D mechanical model, discretized with the FE method, was built to numerically simulate the test by interpreting the outputs from smart bricks, while a procedure, exploiting a kriging interpolator, was developed and used for the post-processing of the strain measurements retrieved from the sensor arrays allowing the reconstruction of the strain field in the wall specimen being monitored.

5.3.2.1 Experimental testing

The tested structural element was a small-scale masonry wall specimen of 370x50x390 mm^3 built at the UniPg LabDyn by arranging 35 bricks in five columns and seven rows by using M15 class cement mortar layers of about 5 mm of thickness. Seven smart bricks, manufactured according to the procedure described in Section 4.2.1 by using a content of stainless steel microfibers equal to 0.50% and external copper plate electrodes, were deployed within the thickness of the wall, by forming a dense sensor network, for monitoring changes in strain. Additionally, each embedded smart sensor was also instrumented with a couple of RSGs, model Kyowa KFG-20-120-C1-11L1M2R, characterized by a gauge factor of 2.11 and directly bonded onto the centerline of the opposite vertical surfaces of each smart brick. Further building details and sensors deployment are exemplified in Fig. 5.4(a). The wall specimen was eccentrically loaded in compression in its plane by applying the load history plotted in Fig. 5.4(b) on its right side, considering a distance from its center of approximately 110 mm. A 5 mm thick steel beam, placed on the top of the masonry structural element with a dry contact, was adopted for load distribution. Each load increment was kept constant for 10 s, thus allowing raw sensor data acquisition.

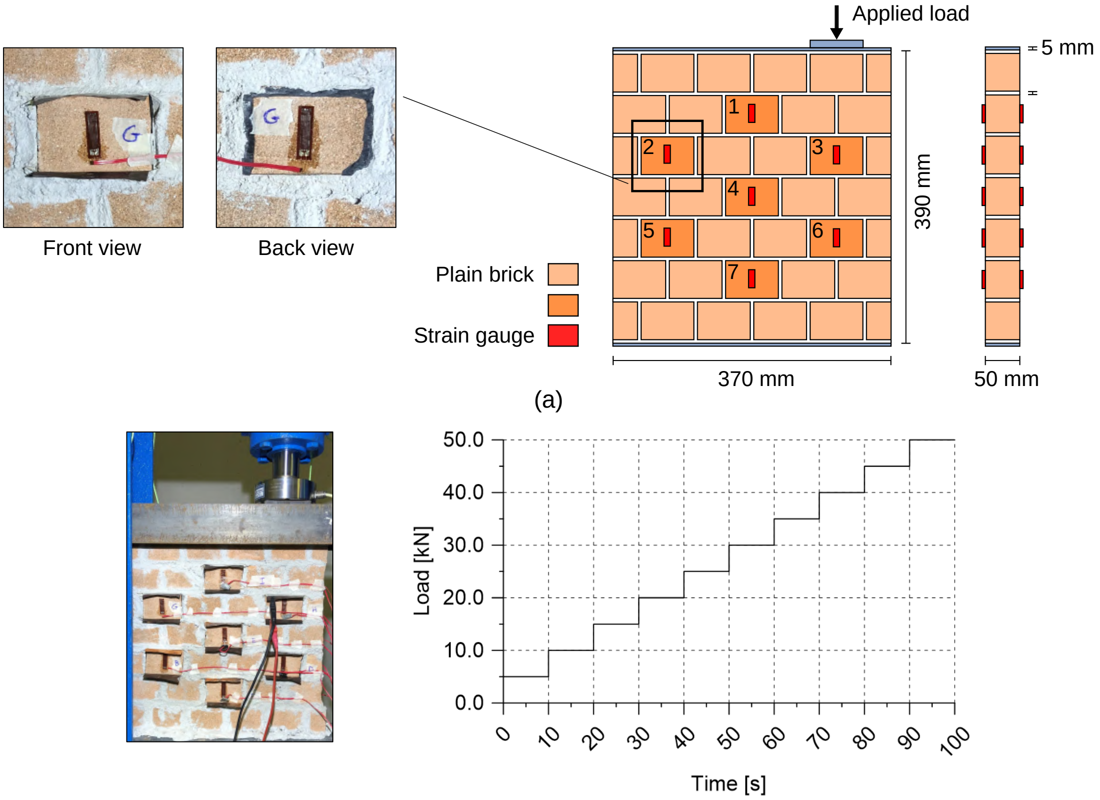

(a)

(b)

Figure 5.4: Electromechanical tests on a small-scale wall specimen equipped with smart bricks made of 0.50% of stainless steel microfibers: (a) Illustration of the tested wall specimen and sensors deployment; (b) Adopted load history and laboratory setup.

In particular, the electrical outputs from smart bricks were gathered by following the methodology reported in Section 4.2.2.1, hence post-processed for strain estimation by means of Eq. (4.10) characterized by the parameters reported in Table 5.2. Contemporary, RSGs were connected to a dedicated data acquisition system, model IMC Cronos-PL 16, through 5-pin DSUB connection terminals, model ACC/DSUB-B2, using a quarter-bridge configuration with a nominal gauge resistance of 120 Ω and a sampling frequency equal to 10 Hz. The obtained strain measurements from smart bricks were therefore compared to the average strain computed from the corresponding couple of RSGs. It is worth noting that the parameters of the series resistors model reported in Table 5.2 were determined to maintain comparable the measurements from smart bricks and RSGs in terms of magnitude, so as focusing the attention on the assessment of changes in strain provided by the two different sensing technologies at each increment of the applied load with respect to the first step of the performed load history. In light of that, the coefficients a' and λ were determined by means of a post-embedded calibration procedure, based on the least square method, matching strain retrieved from smart brick 6 with the average one computed from its corresponding couple of RSGs for an applied load equal to 5 kN. The tuned parameters were selected within a data set containing the results obtained in Section 4.4.2.1 and 4.4.2.2 by testing smart bricks made of 0.50% of steel fibers, while the value of the unstrained internal electrical resistance, $R_{i,0}$, was set equal to the median extracted from the experimental data set. Smart brick 6 was considered for the calibration of the parameters a' and λ since embedded within the portion of the tested structural element expected to be most strained in compression without being positioned too close to the application point of the load. The post-processing of data acquired from smart bricks was carried out through the dedicated software "SHM-Smartbricks", while a custom script developed in Python environment was adopted for processing the data from RSGs.

Table 5.2: Parameters of Eq. (4.10) adopted for retrieving strain measurements from smart bricks (0.50% of stainless steel microfibers) embedded within the small-scale masonry wall specimen: $R_{\mathrm{i},0}$ is the unstrained internal electrical resistance of the smart brick, a' is the relative sensing at the contact resistance, b is the contact resistance exponential term, and λ is the gauge factor.

Sample	$R_{\mathrm{i},0}$ [MΩ]	a'	b	λ
Embedded smart bricks	6.91	1.71E-11	3	529

5.3.2.2 Mechanical model and numerical simulations

Tests carried out on the small-scale masonry wall specimen were numerically simulated through the definition of a non-linear 3D mechanical model, discretized with the FE method in Abaqus environment (see Fig. 5.5), so as interpreting the strain measurements provided by the smart bricks and the RSGs employed for monitoring the structural element. A micromechanical modeling strategy was considered to properly define the mechanical behavior of the masonry components, i.e. plain bricks, mortar layers, and smart bricks, achieving a reasonable level of accuracy in the numerical outputs provided by the FE simulation.

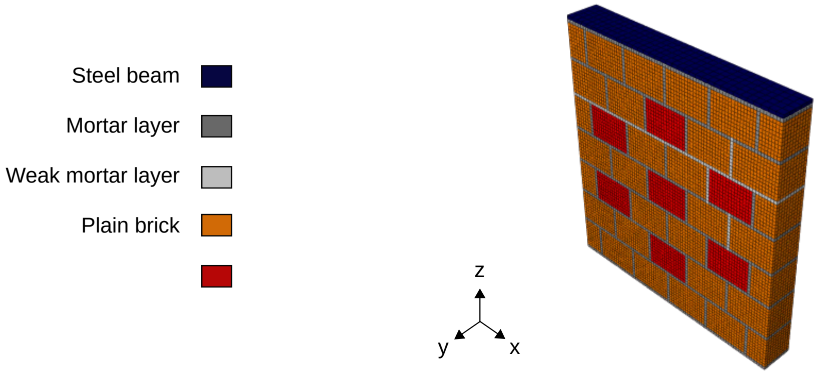

Figure 5.5: Illustration of the micromechanical model reproducing the small-scale masonry wall specimen.

Since the wall specimen was eccentrically loaded in its plane without the application of any horizontal force, hence horizontal slips between the masonry components were conceivably limited, the brick-mortar interaction was neglected, thus simplifying the mechanical model and avoiding also an unnecessary computational effort in the FE simulation, as well as the introduction of further mechanical parameters not experimentally estimated in this work. The nonlinear mechanical behavior of the masonry components was reproduced by adopting the CDP model (see Section 3.3). The 3D model consisted of 68651 nodes and 60840 linear brick elements, type C3D8R, with reduced integration to control shear and volumetric locking (Zienkiewicz et al. 1977). The mesh size was 5.0 mm as the thickness of the layers of mortar. The steel beam used for load distribution was included in the 3D model by discretizing its geometry with C3D8R elements characterized by a mesh size of 10.0 mm. The contact interface comprised between the top surface of the wall and the bottom surface of the steel member was modeled with a surface-to-surface contact interaction specialized with a unilateral contact normal behavior and a frictional tangential behavior. This was set with a friction coefficient equal to 0.6 (Wael and Drysdale 2004), while the bottom surface of the steel beam was chosen as the master surface of the contact interface. An increasing pressure was applied on the steel beam to simulate the loading during the experiment, while pins were set along the three main directions to restrain the 3D model. Table 5.3 outlines the mechanical parameters used to define the behavior of the masonry components and the steel member. In particular, flow potential eccentricity, e, dilatation angle, ψ, ratio of initial equibiaxial compressive yield stress to initial uniaxial compressive yield stress, σ_{bo}/σ_{co}, and ratio of the second stress invariant to the tensile meridian, K_c, were selected from Lubliner et al. (1989), being settings typically used for quasi-brittle materials when dealing with the CDP model. The elastic modulus of the mortar was set reducing by 5% that reported by the manufacturer in the data sheet since a higher amount of water was used for the production of the binding agent to achieve the desired workability. Accordingly, the empirical relation $\sigma_{c0} = E/1000$ was considered for determining its compressive strength. Elastic modulus and compressive strength of smart bricks and plain bricks were obtained from the experiments carried out in Section 4.4.3.2, while the tensile strength of all the masonry components was computed as $\sigma_{t0} = \sigma_{c0}/10$. Values of the fracture energy of smart bricks and plain bricks were taken from Section 4.4.3.2, while that of the mortar was similarly determined by conducting three-point bending tests on samples made with M15 class cement mortar according to the methodology reported in RILEM (1985). A viscosity parameter, $\mu = 0.0001$, was set to resolve convergence issues in the softening branch. The maximum value of the damage parameter d_t for each damageable material was set equal to 0.80 in correspondence of the cracking displacement at which complete loss of strength takes place, u_{t0}.

Such a mechanical model was used to interpret the outputs from the physical sensors instrumenting the wall specimen once the experimental and the numerical cracking patterns were comparable. To do that, the introduction of weak mortar layers in the 3D model was needed, hence the tensile strength of the mortar was reduced by 60% in correspondence of the cracks experimentally developed on the structural element. Besides, the tensile strength of smart bricks was sensibly increased, always to maintain the experimental and the numerical cracking patterns comparable. These parameters, along with the elastic modulus of the mortar, were tuned by preliminary carrying out a sensitivity analysis to assess their influence on the value of the strain retrieved from the smart bricks numerically represented in the 3D model. This was addressed through the methodology proposed in Jørgensen and Bendoricchio (2001). Accordingly, FE simulations were carried out by varying individually the selected parameters by ±10%, hence strain measurements from smart bricks 3 and 6, retrieved for a load applied on the 3D model equal to 5 kN, were considered as reference outputs. The obtained results, reported in Table 5.4, show that the elastic modulus of the mortar was the only parameter affecting the value of the strain extracted from the 3D model. A Python script was properly defined to extract and post-process outputs obtained from the numerical simulation. The mean value of the elastic

Table 5.3: Parameters of the CDP model used to simulate the non-linear mechanical behavior of the construction materials utilized for building the small-scale masonry wall specimen: flow potential eccentricity, e, dilatation angle, ψ, ratio of initial equibiaxial compressive yield stress to initial uniaxial compressive yield stress, σ_{bo}/σ_{co}, ratio of the second stress invariant on the tensile meridian, K_c, elastic modulus, E, Poisson's coefficient, ν, compressive strength, σ_{c0}, tensile strength, σ_{to}, fracture energy, G_f, viscosity parameter, μ, compressive damage parameter (DAMAGEC), d_c, inelastic strain, ϵ_c^{in}, tensile damage parameter (DAMAGET), d_t, and cracking displacement, u_t^{ck}.

General parameters for quasi-brittle materials			
e [-]	ψ [°]	σ_{bo}/σ_{co} [-]	K_c [-]
0.1	10	1.16	2/3
Mortar layers			
$E = 14250$ MPa	ν=0.15	$\sigma_{c0} = 14.25$ MPa	$\sigma_{t0} = 1.43$ MPa
$G_f = 0.013$ N/mm	$\mu = 0.0001$		
$d_c[-]$	ϵ_c^{in} [-]	d_t [-]	u_t^{ck} [mm]
0.00	0.00	0.00	0.00
		0.80	0.02
Weak mortar layers			
$E = 14250$ MPa	ν=0.15	$\sigma_{c0} = 14.25$ MPa	$\sigma_{t0} = 0.57$ MPa
$G_f = 0.013$ N/mm	$\mu = 0.0001$		
$d_c[-]$	ϵ_c^{in} [-]	d_t [-]	u_t^{ck} [mm]
0.00	0.00	0.00	0.00
		0.80	0.05
Plain bricks			
$E = 3275$ MPa	ν=0.15	$\sigma_{c0} = 11.3$ MPa	$\sigma_{t0} = 1.13$ MPa
$G_f = 0.40$ N/mm	$\mu = 0.0001$		
$d_c[-]$	ϵ_c^{in} [-]	d_t [-]	u_t^{ck} [mm]
0.00	0.00	0.00	0.00
		0.80	0.71
Smart bricks			
$E = 4662$ MPa	ν=0.15	$\sigma_{c0} = 8.75$ MPa	$\sigma_{t0} = 1.76$ MPa
$G_f = 0.39$ N/mm	$\mu = 0.0001$		
$d_c[-]$	ϵ_c^{in} [-]	d_t [-]	u_t^{ck} [mm]
0.00	0.00	0.00	0.00
		0.80	0.44
Steel beam			
$E = 210000$ MPa	ν=0.30		

axial strain extracted at the integration points of the solid elements used for the numerical discretization of the smart bricks was computed, hence compared with the corresponding measurements provided by the physical sensors.

Table 5.4: Results from the sensitivity analysis carried out on the 3D model of the small-scale masonry wall specimen: tensile strength, σ_{to} and elastic modulus, E.

	Influence on the outputs [%]	
Parameter	Strain smart brick 3	Strain smart brick 6
σ_{t0} smart brick	0	0
σ_{t0} mortar	0	0
E mortar	-9.72	-9.24

5.3.2.3 Strain field reconstruction

The Ordinary Kriging (OK) approach is implemented in the smart brick technology enabling strain field reconstruction in masonry through the spatial interpolation of the outputs from the smart bricks embedded within strategic locations of the load-bearing structures by forming dense sensors networks. In particular, in this case study, the strain measurements from smart bricks and RSGs instrumenting the wall specimen were adopted as training data for the OK interpolator with the aim to reconstruct the strain field maps of the tested structural element. Kriging is a method of spatial interpolation born from Geostatistics (Krige 1951; Matheron 1963). Nowadays, the kriging interpolator is employed in a broad range of SHM applications for the post-processing of data from dense sensor networks (Laflamme et al. 2016a; Sadoughi et al. 2018b; Qin et al. 2018). Knowing the values of an arbitrary function at specific locations, the kriging permits to evaluate its unknown value at a further point within the computation domain, by taking into account a weighted average of the known observations of the function in the vicinity of the estimation point. The approach exploits interpolation coefficients, determined by adopting a semivariogram model, to correlate samples variation within a data set with the distance between them in the considered domain (Cressie 1992; Zhang and Wu 2015). The OK formulation, which assumes that the mean of the interpolating function is unknown and constant in the considered domain, was chosen among the kriging approaches available in the literature (Cressie 1992), since capable of providing a better estimation of the unknown value at an interpolation point when dealing with a limited data set to train the model. Assuming that z(x) is an arbitrary function satisfying the condition of intrinsic stationarity, whose value at a point x in the spatial domain D is known and that z(x+h) denotes its unknown value at the point x+h, where h is the distance between the two points, the interpolation coefficients can be determined through a generic formulation of a semivariogram model as follows (Cressie 1992):

$$\gamma(h) = \frac{1}{2}\mathrm{Var}[z(x) - z(x+h)], \tag{5.1}$$

Therefore, for n samples within a data set, $z(x_1)$,...$z(x_n)$, at points x_1,...x_n, the OK model predicts the value of $z(x_0)$ at the unknown point x_0 by considering the following linear function (Cressie 1992):

$$z(x_0) = \sum_{i=1}^{n} \lambda_i z(x_i), \tag{5.2}$$

where, $\{\lambda_i\}_{i=1}^{n}$ are the interpolation coefficients selected to obtain an unbiased estimation of the value of the function with a minimum value of the variance.

Spatial interpolations of sensor data were carried out by means of an open-source toolkit, named PyKrige (Murphy 2014), developed in Python environment. More in detail, changes in strain computed with respect to the reference condition (the load step of 5 kN) were computed for both smart bricks and RSGs. Afterward, the data sets were spatially interpolated for mapping changes in strain thorough the entire structural element. Lastly, the obtained maps were compared. The interpolation coefficients in Eq. (5.2) were estimated by adopting a linear variogram model whose parameters were automatically computed by the PyKrige toolkit through an L1 norm normalization scheme (Horn and Johnson 1990). The linear variogram model was chosen among those available in PyKrige, being the model that provided the lowest variance for the considered training data sets.

5.3.2.4 Damage detection and localization

A damage detection and localization procedure, based on the spatially interpolated strain measurements provided by smart bricks, was proposed as depicted in Fig. 5.6 to reveal the development of damages on the tested wall specimen. Exploiting the strain field reconstruction methodology previously described in Section 5.3.2.3, the interpolated map, obtained for a step s of the applied load history, was discretized according to a grid of 10x10 blocks of size of about half a brick and contained an equal number of interpolation points. Then, a damage index, $I_{i,s}$, retrieved from that defined by Laflamme et al. (2016b), was calculated as the ratio between the average strain computed in the i-th reference block and that in its surrounding, A_i, as follows:

$$I_{i,s} = \frac{r_{i,s}}{\sum_{j \in A_i} r_{j,s}/n_i}, \tag{5.3}$$

where $r_{j,s}$ is the average strain in the j-th block of the grid comprised in A_i, while n_i is the number of blocks located in the vicinity of the i-th reference block. The surrounding area A_i was selected by taking into account the arrangement of bricks and mortar layers composing the structural element. In particular, two consecutive blocks close to the i-th reference block were considered in all directions for the index computation, whenever was possible. Once determined, values of the damage index were mapped. Cracking patterns developed on the wall specimen due to excessive compressive strain were therefore identified through the assessment of the areas within the obtained maps marked with the highest value of the proposed damage feature, since this, as it was defined, reaches its maximum value in correspondence of the occurrence of high strain gradients due to the formation of cracks. The parameters reported in Table 5.5 were utilized for the post-processing of the electrical outputs from smart bricks through Eq. (4.10). These were retrieved by selecting the median value of each from an experimental data set obtained by testing smart bricks in Section 4.4.2.1 and 4.4.2.2. A general calibration of the strain-sensing capabilities of the employed novel sensors was therefore preferred. The damage index maps obtained for the smart bricks were benchmarked against those from the RSGs retrieved by following the same procedure.

Table 5.5: Parameters of Eq. (4.10) adopted for retrieving strain measurements from smart bricks (0.50% of stainless steel microfibers) embedded within the small-scale masonry wall specimen for damage detection and localization: $R_{\mathrm{i},0}$ is the unstrained internal electrical resistance of the smart brick, a' is the relative sensing at the contact resistance, b is the contact resistance exponential term, and λ is the gauge factor.

Sample	$R_{\mathrm{i},0}$ [MΩ]	a'	b	λ
Embedded smart bricks	6.91	4.79E-12	3	387

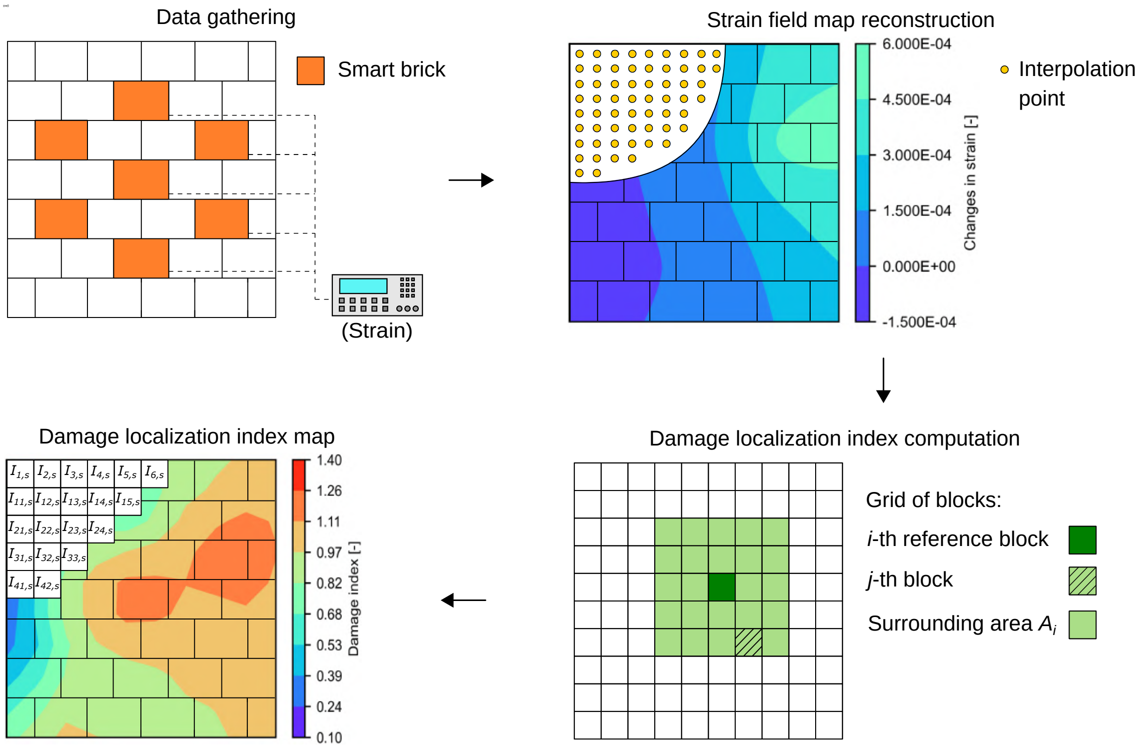

Figure 5.6: Illustration of the damage detection and localization procedure based on the kriging interpolation of the strain measurements provided by smart bricks.

5.3.3 Use of smart bricks deployed within a coarse sensor network

The effectiveness of smart bricks for detecting and locating earthquake-induced damages when deployed in a coarse sensor network within masonry constructions is investigated in this case study, in which the first full-scale experimental application of the smart brick technology for monitoring an unreinforced masonry (URM) building specimen subjected to shaking table tests is presented. In particular, the tested mock-up was progressively damaged by increasing the intensity of the shakes, hence, smart bricks were used to monitor permanent changes in strain induced by the dead load redistributions that occurred within the structure. A 3D mechanical model discretized with the FE method was built to numerically simulate the test by interpreting the outputs from smart bricks.

5.3.3.1 Experimental testing

The URM building specimen was built and tested at the Seismic Laboratory of the ENEA Casaccia Research Center by taking into account, for its design, literature examples concerning masonry buildings previously tested on the shaking table used for this experiment, a 4x4 m^2 platform with six degrees of freedom, frequency range from 0 to 50 Hz, maximum acceleration of 3.00 g, maximum velocity of 0.50 m/s, and maximum displacement of 0.25 m (Dolce et al. 2008; Dolce et al. 2009). The mock-up, shown in Fig. 5.7(a), consisted of two levels and a foundation curb of thickness of 16 cm made with concrete, class C25/28, reinforced with ten longitudinal steel bars, class B450C, of diameter of 10 mm (European Committee 1992). The slab was a 16 cm brick floor reinforced in both directions and fixed to a concrete curb of same thickness containing four steel reinforcing bars of diameter of 10 mm, while the roof was composed by HEA100 beams, made of class S275 steel, arranged in both directions and anchored to a 16 cm thick concrete curb reinforced with six steel rebars of diameter of 10 mm (European Committee 1993). Two balconies were built by anchoring four HEA100 beams to the first and second reinforced concrete curbs. The load-bearing masonry walls were built by arranged M10 cement mortar joints and hollow masonry blocks of 16x30x18 cm^3 obtained by cutting antiseismic thermal blocks of 45x30x18 cm^3, produced by an Italian brick manufacturer (cfr. Acknowledgements) (European Committee 1996). Smart bricks, made according to the methodology described in Section 4.2.1 with a content of steel fibers equal to 0.25% and equipped with external copper plate electrodes, were adopted to instrument the ground floor of the tested mock-up. In light of that, portions of hollow masonry blocks were cut and replaced with smart bricks, by ensuring the connection between the sensors and the blocks with layers of mortar, as shown in Fig. 5.7(b). The obtained masonry subassemblies were deployed as exemplified in Fig. 5.7(c), hence by placing two smart bricks per façade.

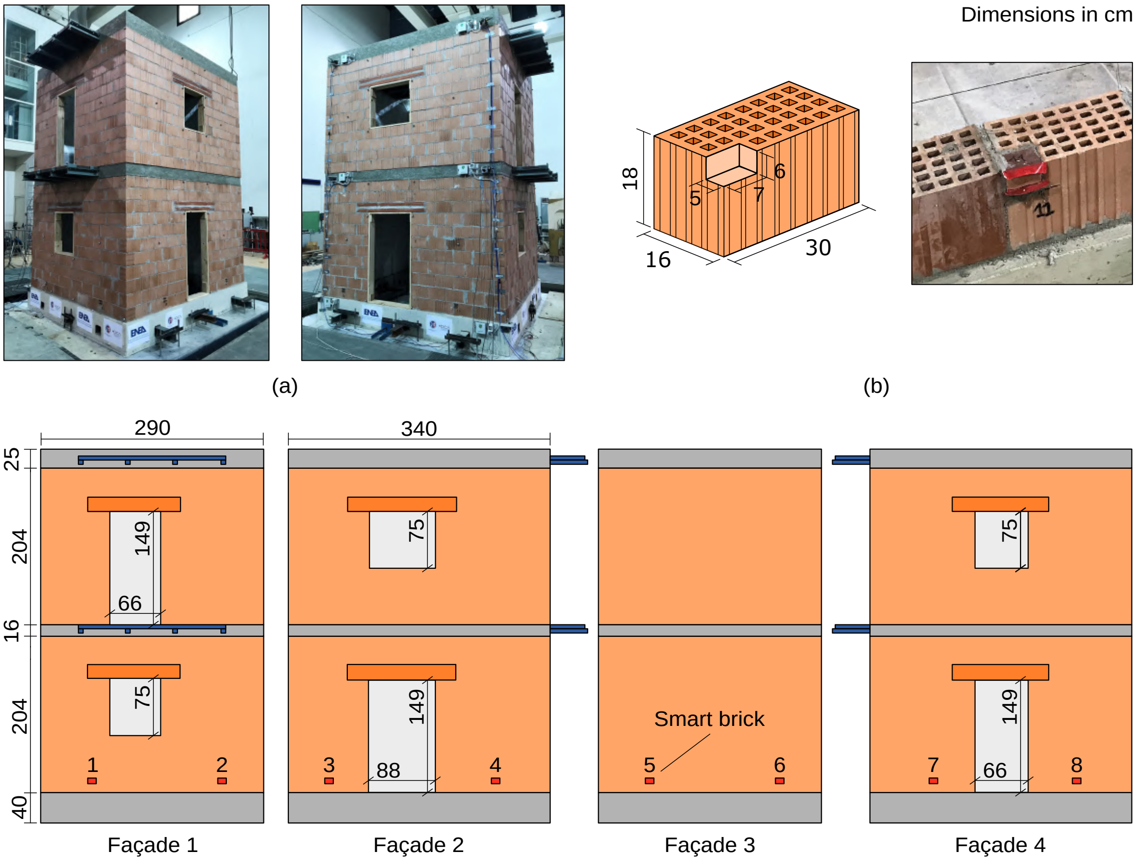

(a) (b)

(c)

Figure 5.7: Illustrations of the URM building specimen subjected to shaking table tests: (a) Pictures of the tested mock-up; (b) Conceptual illustration of a cut hollow masonry block with a picture of a smart brick during its deployment; (c) Building details of the tested specimen with annotated the positions of the smart bricks.

It is worth noting that the production of smart bricks with the same shape and geometrical dimensions of the adopted hollow masonry blocks would have been challenging at this early stage of research. Therefore, the use of such masonry subassemblies with embedded smart bricks was considered as the most feasible approach to keep simple the production of the sensors and to instrument the URM building without altering its structural response at the same time. Additional steel plates were positioned at the first slab, on the steel slab of the roof and the two balconies to increase the dead loads, whose entity is detailed in Table 5.6.

Table 5.6: Structural masses of the URM building specimen.

Mass	[10^3 kg]
Foundation	1.38
Structure	13.40
Additional	5.80
Total	20.58
Total without foundation	19.20

The URM building specimen was also instrumented by mounting ten uniaxial accelerometers, model PCB 3711B112G, on the concrete curb of the foundation, first floor, and roof, to measure accelerations along the three main orthogonal directions x, y, and z. Tests were conducted by anchoring the mock-up to the shaking table using post-tensioned steel rods and providing seismic inputs of increasing intensity according to the test sequence reported in Table 5.8. Progressive damages were therefore induced to the structure. These were carefully detected by carrying out visual inspections after the execution of each ground motion. The adopted seismic input corresponded to the waveform of the Norcia Mw 6.5 earthquake (October 30^{th} 2016 at 06:40 UTC, epicenter coordinate latitude 42.84° and longitude 13.11°) recorded by the NRC seismic station located in Norcia and comprised in the Italian Strong Motion Network (RAN) (Gorini et al. 2010). Records of its three acceleration components, acquired during the execution of E2 earthquake by using the accelerometers mounted on the foundation concrete curb, are reported in Fig. 5.8. A Gaussian white-noise acceleration input, characterized by a standard deviation of 0.05 g, was performed before and after each main shake for dynamic investigations (Pepi et al. 2019; Cavalagli et al. 2020).

5.3.3.2 Damage detection and localization

The electrical outputs were acquired from smart bricks after the execution of the main shakes, i.e. the earthquakes E1, E2, and E3, and after the white-noise inputs, WN1, WN2, and WN4, by following the methodology illustrated in Section 4.2.2.1. Strain estimation was carried out by using the series resistors model (Eq. (4.10)) specialized with the set of parameters collected in Table 5.8. These were determined in Section 4.4.2.1 by testing smart bricks made with a content of steel fibers equal to 0.25%. Such a common set of parameters was considered since the employed smart bricks were not individually characterized before their installation within the URM building specimen. Damages progressively

Table 5.7: Seismic sequence adopted to test the URM building specimen (I_A^x, I_A^y, I_A^z are the components of the Arias Intensity ground motion parameter, computed for the three orthogonal directions (Stafford et al. 2009)).

Stage	Identification Code	Description	I_A^x [cm/s]	I_A^y [cm/s]	I_A^z [cm/s]
1	WN1	Step 1: white-noise			
	E1	Step 2: E1 earthquake	73.28	76.63	95.10
	WN2	Step 3: white-noise			
2	E2	Step 4: E2 earthquake	610.63	308.09	281.20
	WN3	Step 5: white-noise			
3	E3	Step 6: E3 earthquake	614.86	363.41	368.96
	WN4	Step 7: white-noise			

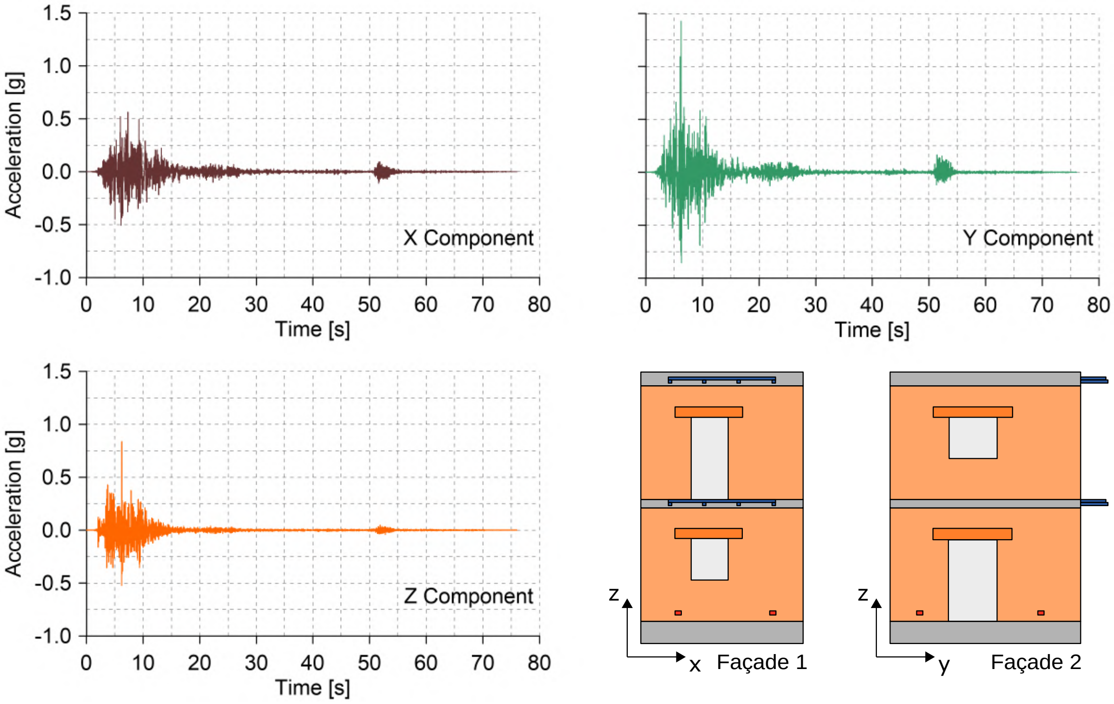

Figure 5.8: Records of the three acceleration components of E2 earthquake acquired by the accelerometers mounted on the foundation concrete curb of the URM building specimen.

developed to the tested mock-up were detected and located by assessing changes in strain through the definition of global and local damage indexes, I_{brick}, based on the damage feature proposed by García-Macías and Ubertini (2019), as follows:

$$I^s_{\text{brick}} = \frac{1}{n}\sum_i |\epsilon^s_{\text{brick},i} - \epsilon^0_{\text{brick},i}|, \tag{5.4}$$

where n is the number of smart bricks considered in the index computation ($n = 8$ for the global damage index, $n = 2$ for the local damage index), $\epsilon^s_{\text{brick},i}$ is the value of the strain retrieved from the i-th smart brick at the step, s, of the performed seismic sequence, while $\epsilon^0_{\text{brick},i}$ is that obtained at the reference condition, WN1. It is worth noting that the execution of the white-noise WN1 produced a redistribution in the dead loads of the tested mock-up without developing any visible damage, hence, this step was chosen as reference condition since more representative of the coupled structural system consisting in the mock-up and the shaking table. Eq. (5.4) therefore points out the average variation in the strain measurements from smart bricks under dead loads with respect to the reference condition at which the URM specimen was considered in a sound state. A value of the index equal to zero computed for a step, s, of the performed seismic sequence means that the tested mock-up was undamaged at the considered stage, whereas values of the index greater than zero denote the occurrence of permanent strain variations that may indicate the development of damages to the structure depending on their magnitude (i.e. marked changes in strain are attributable to the development of cracks).

Table 5.8: Parameters of Eq. (4.10) adopted for retrieving strain measurements from smart bricks (0.25% of stainless steel microfibers) embedded within the URM building specimen: $R_{\text{i},0}$ is the unstrained smart brick's internal electrical resistance, a' represents the relative sensing at the contact resistance, b is the exponential term, and λ is the gauge factor.

Sample	$R_{\text{i},0}$ [MΩ]	a'	b	λ
Embedded smart bricks	7.78	6.83E-13	3	374

5.3.3.3 Mechanical model and numerical simulations

The shaking table test was numerically simulated to interpret the strain measurements provided by the smart bricks instrumenting the ground floor of the URM building specimen. In light of that, a macromechanical model (see Fig. 5.9), discretized with the FE method and characterized by 106709 nodes and 76699 linear brick elements, type C3D8R, with reduced integration and a mesh size of 50 mm, was built in Abaqus environment.

Reduced integration was considered to control shear and volumetric locking (Zienkiewicz et al. 1977), while such a mesh size was chosen to represent smart bricks embedded within the load-bearing walls at about a third of their thickness while maintaining a reasonable computational efficiency. Parts of the tested mock-up were first modeled separately by

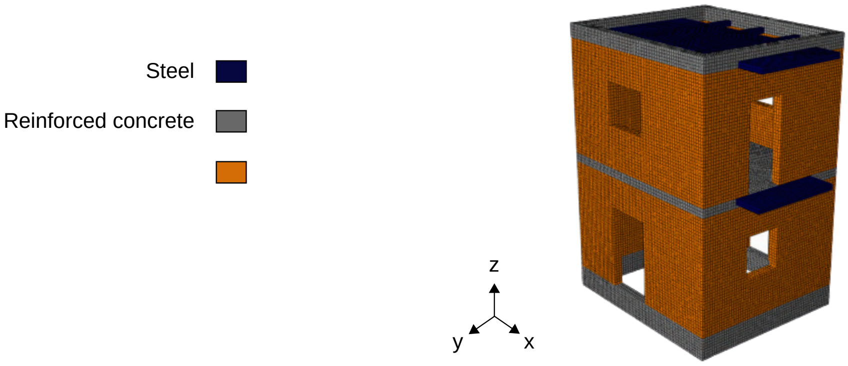

Figure 5.9: Illustration of the macromechanical model reproducing the URM building specimen.

assigning the corresponding mechanical properties to each one, hence, merged according to the global geometry. Structural elements not affected by any damage after the execution of the seismic sequence were defined in the model as homogeneous isotropic linear elastic materials, thus their mechanical behavior was described by providing the elastic modulus, E, and the Poisson's coefficient, ν. Accordingly, E = 20000 MPa and ν=0.2 were set for reinforced concrete elements, while E = 210000 MPa and ν=0.3 for steel members. The masonry was modeled as a homogeneous isotropic material, hence the CDP model was considered to describe its non-linear mechanical behavior, in particular, to simulate damages that occurred to the load-bearing walls as degradation of the elastic stiffness of the masonry (see Section 3.3). Following, a brief recap concerning the nature of the mechanical parameters adopted in the plastic-damage model is provided (see Table 5.9). The elastic modulus, E, the Poisson's coefficient, ν, and the compressive strength, σ_{c0} were determined by homogenizing the mechanical properties of employed masonry blocks and cement mortar, provided by the manufactures, according to the Italian Technical Standard. The tensile strength, σ_{to}, was determined by considering the empirical relation, $\sigma_{to} = \sigma_{co}/10$, while the fracture energy, G$_f$, was defined by taking into account the investigations carried out in Pluijm, van der (1992). Dilatation angle, ψ, flow potential eccentricity, e, ratio of initial equibiaxial compressive yield stress to initial uniaxial compressive yield stress, σ_{bo}/σ_{co}, and ratio of the second stress invariant to the tensile meridian, K_c, were taken from the study proposed by Lubliner et al. (1989) and correspond to values typically used for quasi-brittle materials. Considering that the cracking patterns detected on the URM building were conceivably caused by an excess in the shear forces acted in the structure during the shakes, the compressive damage parameter, d_c, and the inelastic strain in compression, ϵ_c^{in}, were set equal to zero, while the tensile damage parameter, d_t and the cracking displacement, u_t^{ck}, were retrieved from the work proposed by Zizi et al. (2017). It should be noted that the tensile strength of the masonry was numerically adjusted, with respect to its initial value, by carrying out a calibration procedure of the 3D model to obtain a numerical cracking pattern comparable to that observed by testing the URM building specimen. In particular, the tensile strength was increased by about 70%. A Rayleigh damping set to 5% was considered to reduce spurious oscillations occurring in the high-frequency domain that can trigger instability of the computation process (Honda and Sawada 1992). No viscosity regularization of the constitutive laws of the CDP model was adopted, while the standard settings for the stiffness recovery were considered. Measurements recorded by the accelerometers mounted on the reinforced concrete foundation curb of the tested structure were used to reproduce the experimental seismic sequence reported in Table 5.8.

Table 5.9: Parameters of the CDP model used to simulate the non-linear mechanical behavior of the load-bearing masonry walls: Elastic modulus, E, Poisson coefficient, ν, compressive strength, σ_{c0}, tensile strength, σ_{to}, fracture energy, G_f, viscosity parameter, μ, dilatation angle, ψ, flow potential eccentricity, e, ratio of initial equibiaxial compressive yield stress to initial uniaxial compressive yield stress, σ_{bo}/σ_{co}, ratio of the second stress invariant on the tensile meridian, K_c, compressive damage parameter (DAMAGEC), d_c, inelastic strain, ϵ_c^{in}, tensile damage parameter (DAMAGET), d_t, and cracking displacement, u_t^{ck}.

Elastic constants of the model	
$E = 3000$ MPa	$\nu = 0.2$
Non-linear parameters of the model	
$\sigma_{c0} = 3.50$ MPa	$\sigma_{to} = 0.60$ MPa
G$_f$ = 0.06 N/mm	$\mu = 0$
$\psi = 10°$	$\epsilon = 0.1$
$\sigma_{bo}/\sigma_{co} = 1.16$	$K_c = 0.667$
Damage in compression	
d_c	ϵ_c^{in}
0.00	0.00
Damage in tension	
d_t	u_t^{ck} [mm]
0.00	0.00
0.40	0.02
0.60	0.04
0.80	0.1

A custom Python subroutine was defined to retrieve strain measurements from the integration points of the solid elements of the 3D model located at the same position of the smart bricks embedded within the URM building specimen. Global and local damage indexes were defined to estimate the severity of the damage that occurred to the 3D model interpreting the experimental results obtained by post-processing the outputs from the physical sensors. Therefore, by considering a step, s, of the simulated seismic sequence, global and local damage indexes, I^s_{FEM}, were calculated as follows:

$$I^s_{\mathrm{FEM}} = \frac{1}{n}\sum_i |\epsilon^s_{\mathrm{FEM},i} - \epsilon^0_{\mathrm{FEM},i}|, \tag{5.5}$$

where n is the number of solid elements in the 3D model considered in the index computation ($n = 8$ for the global damage index, $n = 2$ for the local damage index), $\epsilon^s_{\mathrm{FEM},i}$ is the value of the strain extracted from the i-th brick element and referred at the considered step, s, of the simulated seismic sequence, while $\epsilon^0_{\mathrm{FEM},i}$ is that obtained at the reference condition (WN1).

A frequency response analysis was also carried out after each step of the simulated seismic sequence to evaluate the influence of the damages progressively developed on the 3D model on its modal features. In particular, by considering that a reduction in the stiffness of the model, due to damage in tension, results in a decrease in its eigenvalues, the decay in the natural frequencies of the 3D model was computed with respect to the reference condition WN1. Subsequently, a global damage index, $I^s_{\mathrm{freq\ FEM}}$, was defined for a considered step, s, of the simulated seismic sequence, as follows:

$$I^s_{\mathrm{freq\ FEM}} = \frac{1}{n}\sum_i |\omega^s_{\mathrm{FEM},i} - \omega^0_{\mathrm{FEM},i}|, \tag{5.6}$$

where n is the number of modes of vibration of the 3D model considered for the index computation ($n = 20$), $\omega^s_{\mathrm{FEM},i}$ is the value of the numerical natural frequency at the step, s, of the simulated seismic sequence for the i-th mode of vibration of the model and $\omega^0_{\mathrm{FEM},i}$ is that obtained from the assumed reference condition (WN1).

5.4 SHM applications: Results

This section outlines the results achieved by employing smart bricks for monitoring strain in the proposed case studies.

5.4.1 Validation of the series resistors model by testing a typical structural setting

A small-scale masonry wall specimen equipped with smart bricks was tested to axial compression loads to demonstrate the effectiveness of the series resistors model in estimating strain by using the electrical outputs from the novel sensors when embedded within a typical structural setting. The wall specimen was pre-damaged by applying a centered axial compression load, hence smart bricks were used for monitoring developments in the existing cracking pattern induced by eccentrically loading in compression the structural element. Fig. 5.10(a) shows vertical cracks that were formed on cement mortar joints by testing the wall specimen. Cracks named c_1, c_2, and c_3 were developed by increasing the compression load applied centrally to the wall specimen up to 30 kN. Their symmetrical position, with respect to the centerline of the wall, denotes a homogeneous redistribution of the load paths throughout the structural element. The performed eccentric axial compression test produced an increase in the width of the existing openings and the formation of new cracks, namely c_4, c_5, c_6, and c_7, which developed in the middle area of the structural element. Their initiation was heard and visually detected after the application of the load step of 20 kN, hence, a further increase in the applied load, up to 30 kN, only produced an increment in their thickness. Strain measurements retrieved from the embedded smart bricks are plotted in Fig. 5.10(b). Smart bricks named 2, 5, 7 were the most strained in compression at the end of the test, thus confirming the consistency of the reported results with the investigated case study. The novel sensors detected cracks initiation at 20 kN by means of sudden changes in their strain outputs. In particular, after the formation of the central cracks, c_4, c_5, c_6, and c_7, compressive strain increased faster than before within the area surrounding smart bricks 2, 5, and 7, as demonstrated by their trends. On the other hand, smart bricks 1, 4, and 6 revealed a slower increase in strain compared to their initial tendencies. Additionally, the formed cracking pattern induced a progressive decompression in smart brick 3. Overall, the obtained results demonstrated that the series resistors model can be used for strain estimation when smart bricks are embedded within a typical structural setting. It is worth noting that this investigation also exemplified a first application of the smart brick technology for damage detection, by pointing out that the outputs from the novel sensors are effectively influenced by the internal load paths redistributions due to the formation of cracks.

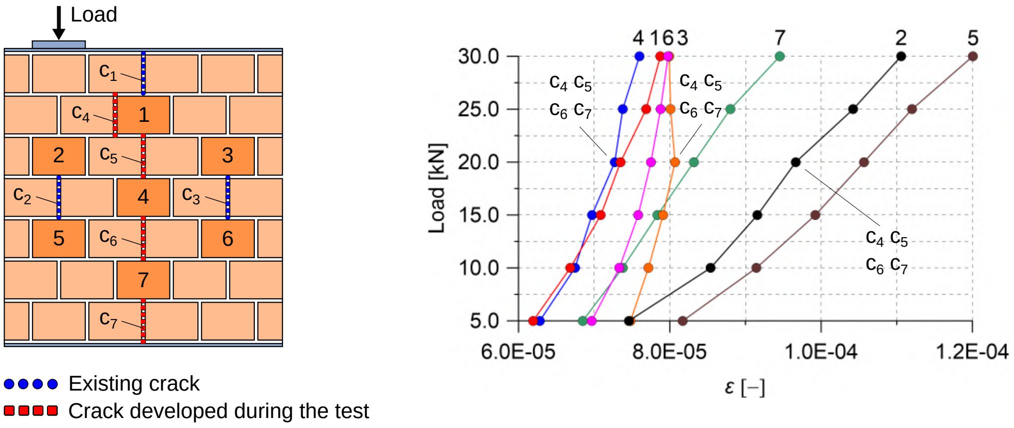

(a) (b)

Figure 5.10: Results from compression tests carried out on a small-scale masonry wall specimen equipped with smart bricks (0.25% of stainless steel microfibers): (a) Illustration of the cracks formed on the structural element; (b) Applied loads versus strain estimated through the post-processing of the electrical outputs from smart bricks gathered during the execution of the eccentric axial compression test.

5.4.2 Use of smart bricks deployed within a dense sensor network

A small-scale masonry wall specimen was instrumented with smart bricks and RSGs, deployed in a dense sensor network, to monitor changes in strain under eccentric axial compression loads. Results obtained in this case study are reported as follows.

5.4.2.1 Experimental and numerical cracking patterns

The experimental and numerical cracking patterns detected on the wall specimen and the 3D model, respectively, are illustrated in Fig. 5.11. The application of a load equal to 15 kN on the tested structural element produced the development of cracks of initial small thickness, named c_1, c_2, and c_3. Crack c_4 formed later by increasing the applied load to 25 kN, while crack c_5 was detected at the completion of the load history. The wall specimen was still capable of maintaining its structural integrity at the end of the test despite affected by a severe damage state. Damaged areas on the 3D model were identified through the assessment of the parameter d_t. A cracking pattern comparable with that experimentally observed by testing the wall specimen was obtained on the 3D model only at the end of the FE simulation, although weak mortar layers were used to facilitate the reproduction of the openings developed during the experiment. The early development of damages on the tested structural element, not corresponding to what happened to the 3D model, can be conceivably associated with irregularities in the arrangement of bricks and mortar layers that induced stress concentrations within the wall specimen, whose numerical simulation is for obvious reasons particularly challenging.

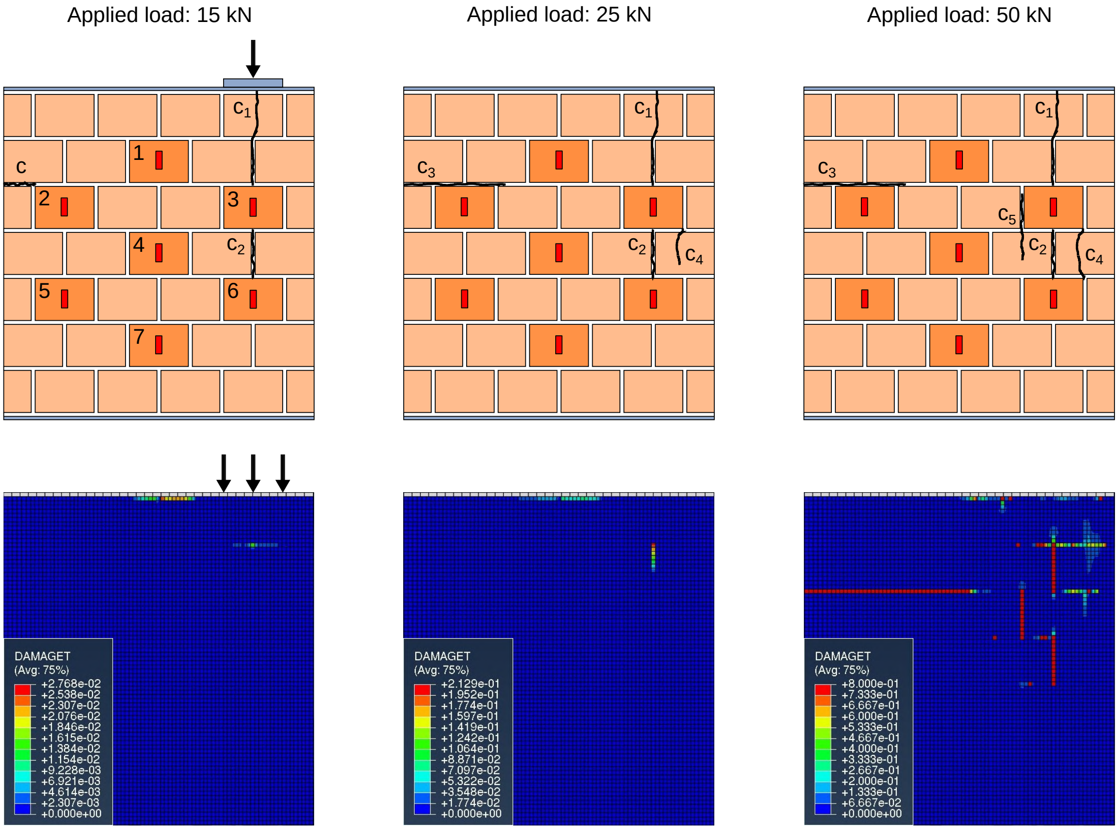

Figure 5.11: Experimental and numerical cracking patterns detected on the small-scale masonry wall specimen and its 3D model, respectively.

5.4.2.2 Experimental and numerical strain outputs

Changes in strain computed from the outputs provided by the adopted physical sensors are depicted in Fig. 5.12, together with those retrieved from the FE simulation. On the whole, the reported trends indicate a satisfactory consistency among the obtained results. The development of cracks c_1, c_2, and c_3 was clearly detected by smart brick 3 through a marked variation in its compressive strain condition. Similarly, the formation of crack c_4 was revealed by smart brick 6, since embedded in its surrounding. The couples of RSGs corresponding to smart bricks 3 and 6 detected the formation of cracks c_1, c_2, and c_3 in a similar fashion, nevertheless changes in strain outputted by the traditional devices were of lower magnitude compared to those shown by smart bricks. The development of cracks during the execution of the load history induced load paths redistributions internally to the central part of the wall specimen that affected the strain state of the smart bricks 1, 4, and 7. Indeed, these sensors outputted non-constant increasing compressive strain while the load increased linearly. RSGs instrumenting that area were less affected by the load paths redistributions that took place, as confirmed by their outputs which do not show particular changes in their trends. The compression state that acted on smart bricks 2 and 5 decreased due to the onset of tensile stresses in the left part of the wall specimen during the test. These were induced by the application of the compression load externally to the centroid of the tested structural element. In this case, smart brick 2 and its corresponding RSGs well revealed the decompression that occurred in that area by outputting changes in strain of similar magnitude. Smart brick 5, unlike its corresponding couple of RSGs, shown instead a marked reduction in its compressive strain condition only in correspondence of the formation of crack c_4. Although experimental and numerical trends similarly indicate the portions of the tested structural element affected by strain concentrations or relaxations, differences in the magnitude between experimental and numerical changes in strain were detected. These can be reasonably associated with the delay in the onset of damaged areas in the 3D model, compared to the cracks that early developed on the wall specimen during the experiment. However, both the physical and numerical smart bricks embedded in the central area of the wall specimen and the 3D model, respectively, pointed out the occurrence of internal load paths redistributions in their surrounding, which were only slight revealed by the RSGs adhered in that portion of the tested structural element.

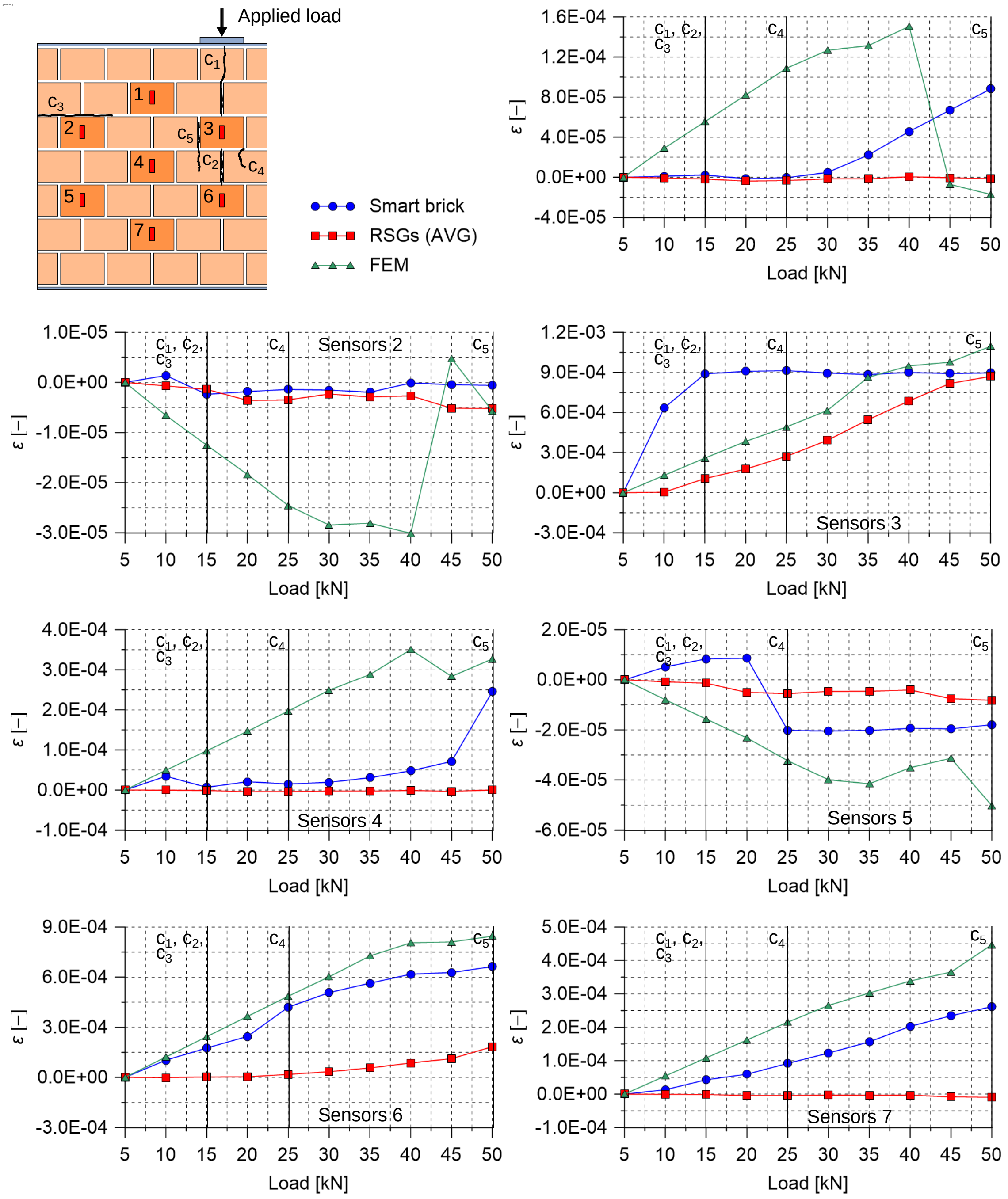

Figure 5.12: Changes in strain computed for smart bricks and RSGs instrumenting the small-scale masonry wall specimen. The numerical outputs from the 3D model were also reported.

5.4.2.3 Reconstruction of the strain field

The outputs from smart bricks and RSGs were post-processed by means of the OK interpolator to reconstruct the strain field of the tested structural element at each step of the applied load history with respect to the reference condition, i.e. the application of a load equal to 5 kN. The obtained results are depicted in Fig. 5.13 and 5.14, which report strain field maps from smart bricks and RSGs, respectively, computed by using the same colormap to simplify the comparison between these different sensing technologies. The reported maps clearly show where the compression load was applied and how its increase modified the strain field of the wall specimen, from the first glance. Indeed, portions of the wall specimen strained in compression are well identifiable in both the maps from smart bricks and RSGs. It should be noted, however, that maps obtained from the novel sensors outline a more detailed evolution of the changes in strain during the execution of the test. Smart bricks, being embedded within the thickness of the masonry, were more sensitive to the internal load paths redistributions that occurred within the wall specimen at each increment of the applied load, while RSGs, externally attached to the bricks, were conceivably able to reveal only changes in strain of lower magnitude. Maps obtained by carrying out the FE simulation, which are plotted in Fig. 5.15, show strain fields that are similar to those reconstructed by using smart bricks, thus supporting the more homogeneous distribution of the strain within the wall specimen pointed out by the novel sensors. Along these lines, also the assessment of the changes in strain in the middle cross-section of the wall specimen, shown in Fig. 5.16, confirmed the greater strain sensitivity owned by the smart bricks with respect to that of the RSGs. Indeed, the outputs from the novel sensors and those from the 3D model are characterized by a good agreement between themselves, while those from RSGs remark the modest strain-sensing capabilities shown by the traditional sensors in comparison with those exhibited by smart bricks. The scattered trend visible in the strain profiles from the FE simulation in correspondence of the application of high compression loads on the wall specimen is due to the non-linear mechanical behavior characterizing the adopted 3D model that was therefore capable of taking into account the development of damages, as well as of simulating the internal load paths redistributions. On the contrary, being the strain profile of smart bricks and RSGs extracted from strain field maps retrieved by carrying out a linear interpolation of the training data sets in the computation domain, their changes in strain are not affected by a similar scattered trend.

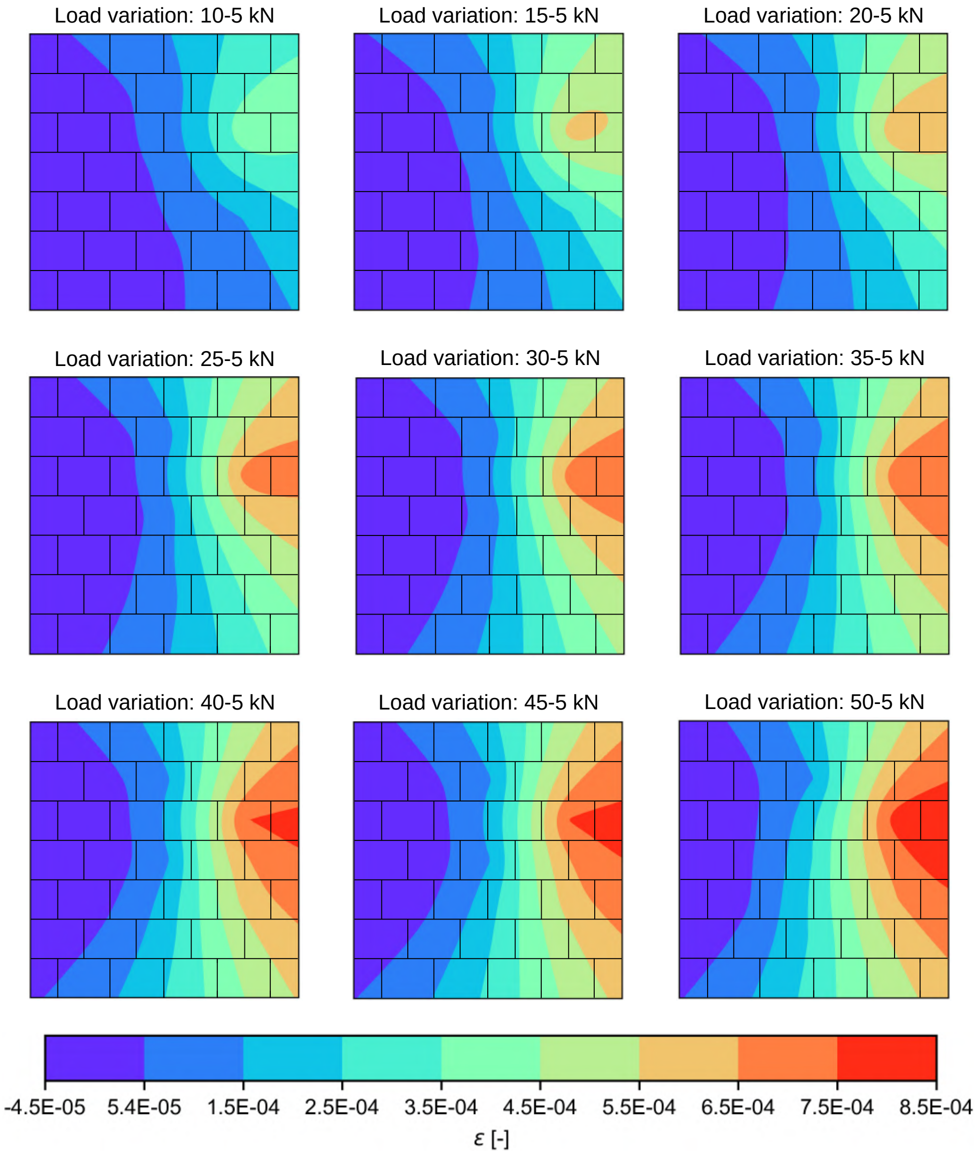

Load variation: 10-5 kN

Load variation: 15-5 kN

Load variation: 20-5 kN

Load variation: 25-5 kN

Load variation: 30-5 kN

Load variation: 35-5 kN

Load variation: 40-5 kN

Load variation: 45-5 kN

Load variation: 50-5 kN

Figure 5.13: Strain field maps retrieved through the post-processing of the outputs from the smart bricks instrumenting the small-scale masonry wall specimen.

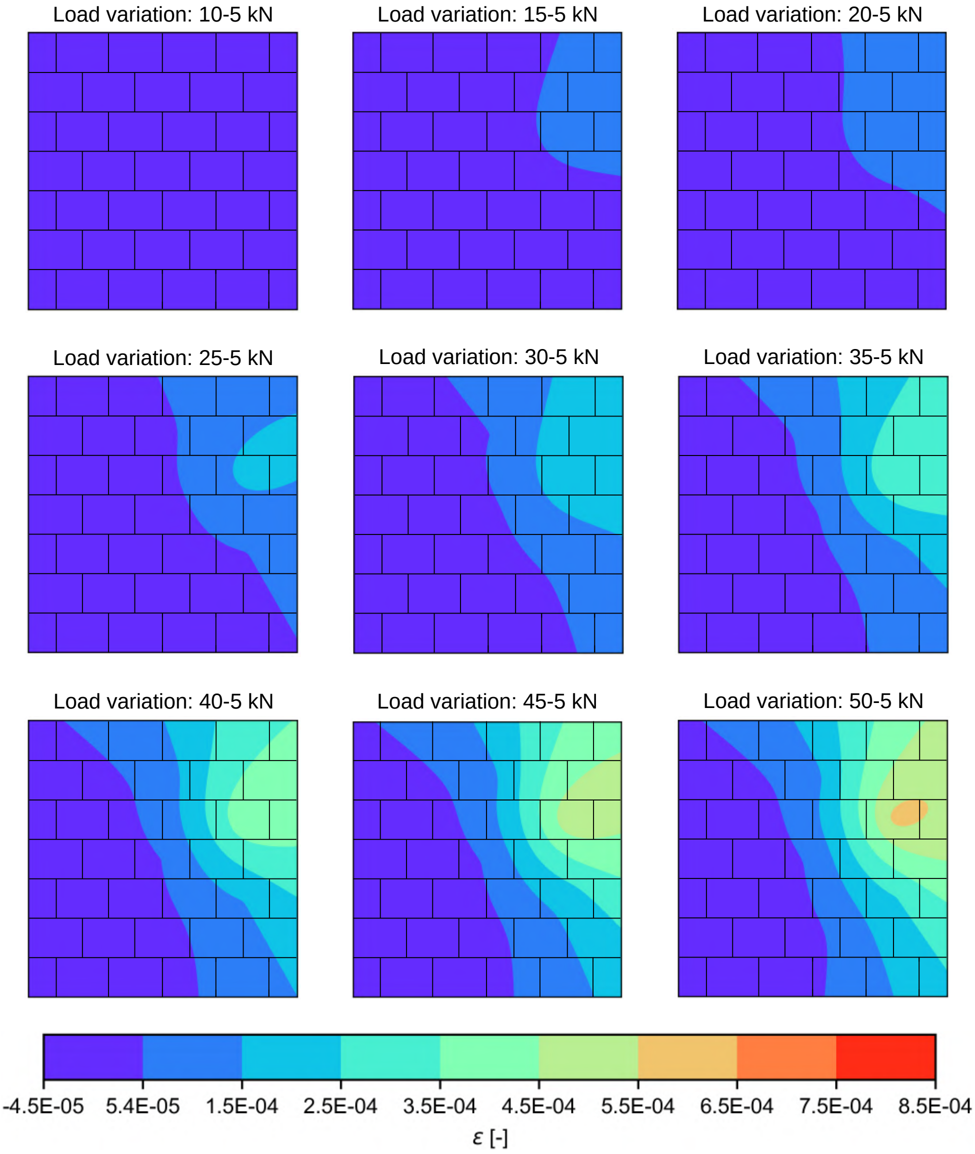

Figure 5.14: Strain field maps retrieved through the post-processing of the outputs from the RSGs instrumenting the small-scale masonry wall specimen.

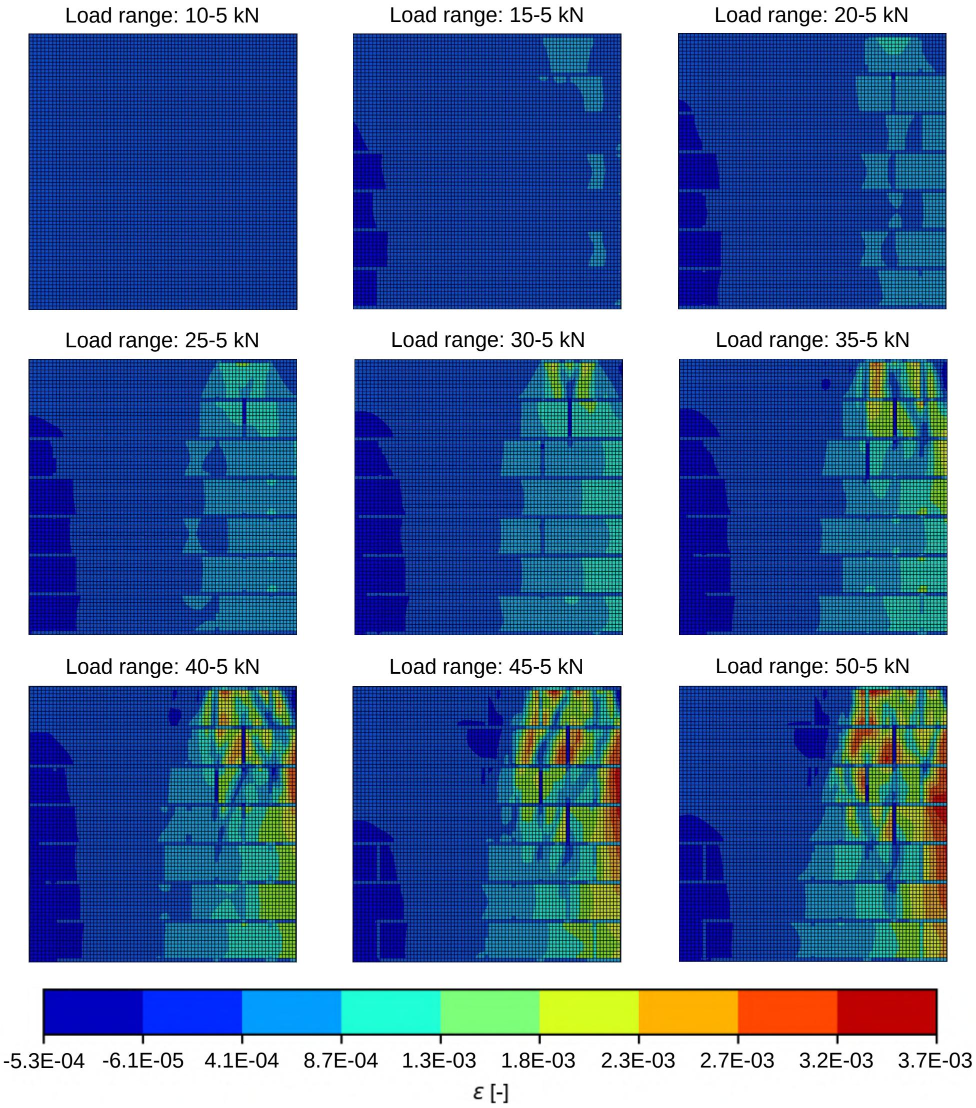

Figure 5.15: Numerical strain field maps obtained from the FE simulation carried out on the 3D model of the small-scale masonry wall specimen.

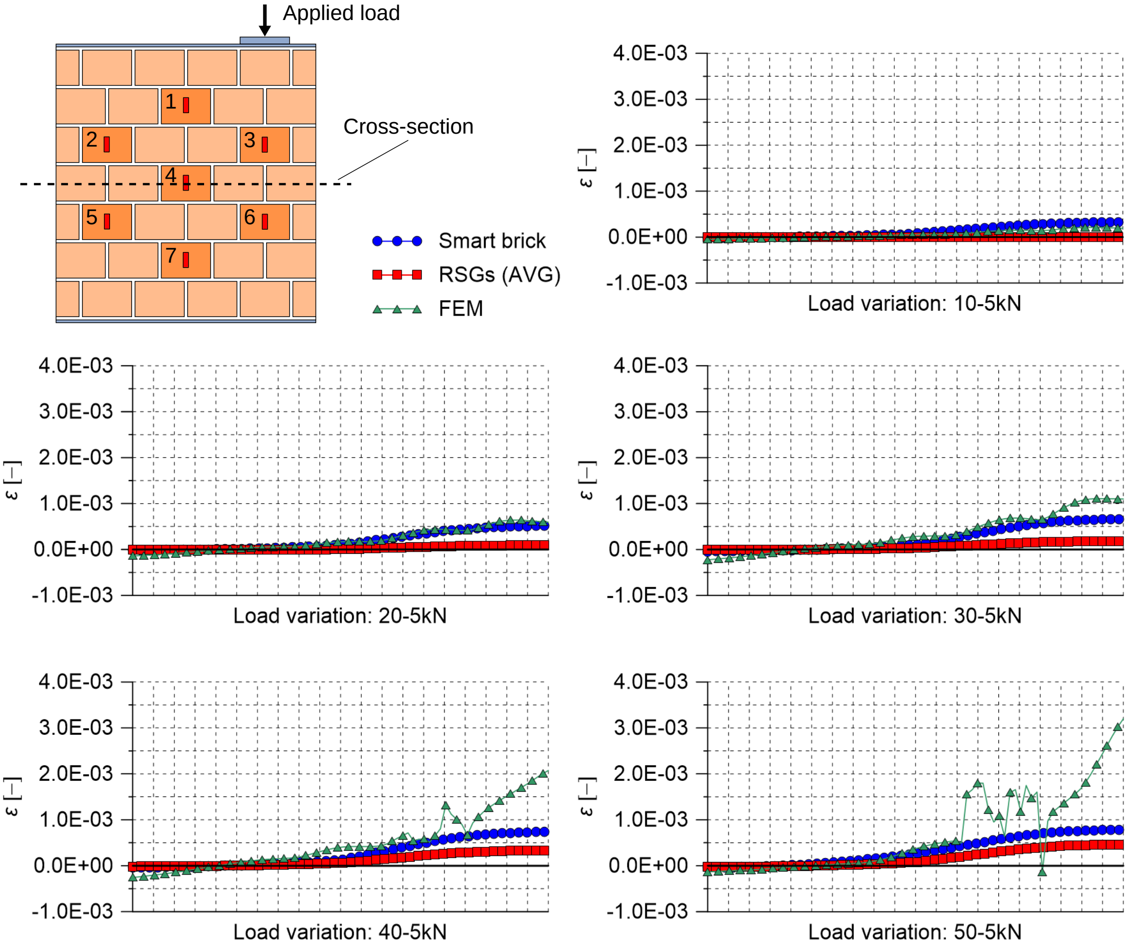

Figure 5.16: Trends of the changes in strain in the middle cross-section of the small-scale masonry wall specimen retrieved from the strain field maps reconstructed by using the outputs from smart bricks, RSGs and FE simulation.

5.4.2.4 Damage detection and localization

Damage index maps obtained by post-processing the measurements from smart bricks and RSGs according to the proposed damage detection and localization procedure are reported in Fig. 5.17 and 5.18, respectively, by using a common colormap to keep simple the comparison between the results. All the maps from smart bricks point out the occurrence of high strain gradients on the right part of the wall specimen, which can be therefore considered a critical area of the tested structural element that may be subjected to damage, as the index was defined. On the whole, this is coherent to what happened to the wall specimen during the experiment. The maximum value of the damage index was computed in correspondence of the formation of cracks c_1 and c_2 under the application of a load equal to 15 kN. Indeed, the largest strain gradients reasonably occurred at this load step since c_1 and c_2 were the first cracks developed on the wall specimen. Following, the formation of crack c_4 produced a noticeable increase in the index value in its proximity. After that, the development of crack c_5 in correspondence of the application of a load equal to 50 kN did not produce noteworthy strain gradients since the right part of the tested structural element was already severely damaged. Similarly, the opening of crack c_3, due to concentrations of direct tensile stress, was undetectable in any plot, since its opening produced strain gradients of lower magnitude in comparison to those that occurred in the right portion of the wall specimen strongly strained in compression. Therefore, after the load step corresponding to the application of 25 kN, the damage index slightly increased its value in the area surrounding the damaged part of the wall specimen as the applied compression load increased. Overall, damage index maps obtained from smart bricks satisfactorily allow the detection and localization of the cracking pattern developed on the tested structural element. On the contrary, maps retrieved by means of the post-processing of the outputs from RSGs are not equally effective for the identification of the occurred damages. This is due to the modest sensitivity shown by the RSGs to the changes in strain induced by the load paths redistributions that took place throughout the wall specimen by increasing the applied compression load.

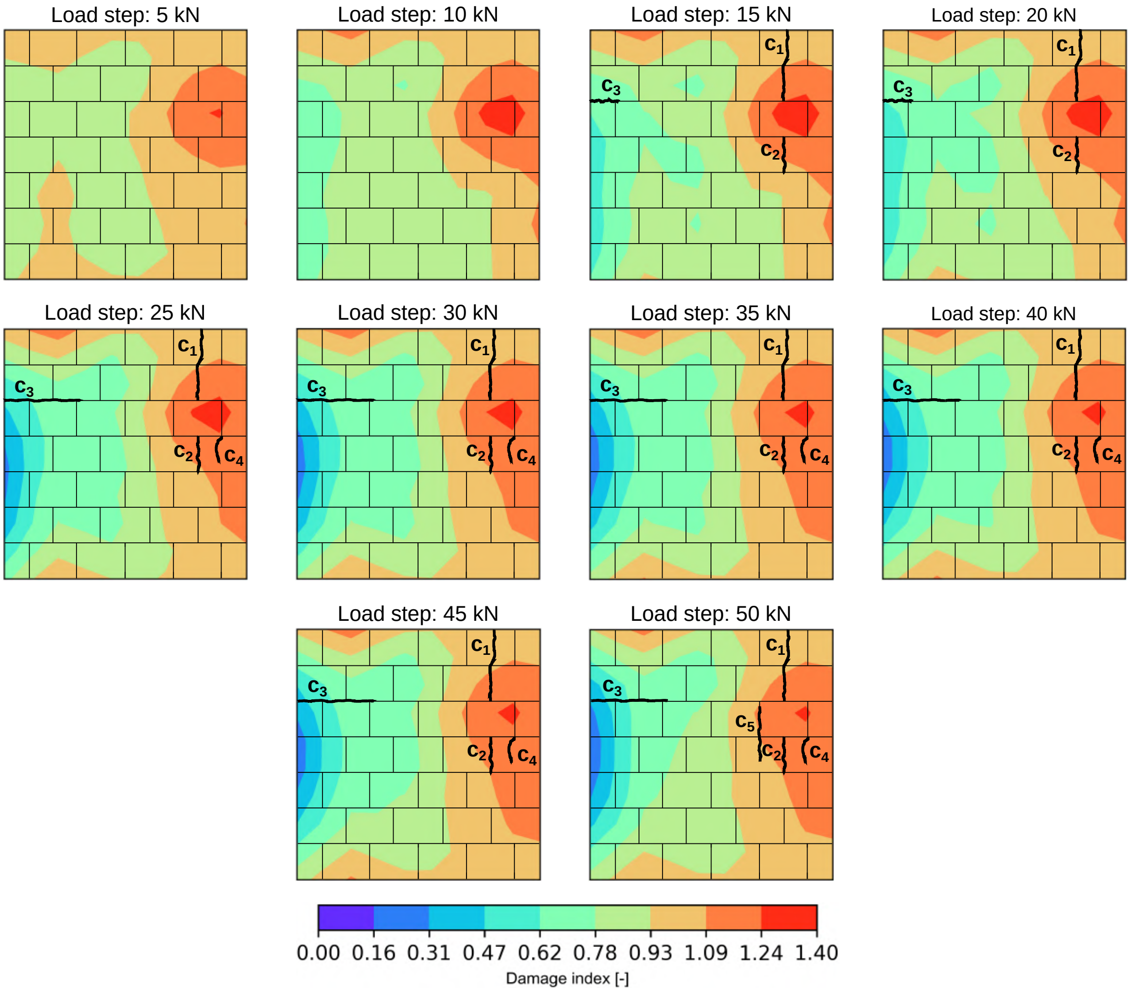

Figure 5.17: Damage index maps retrieved through the post-processing of the outputs from the smart bricks instrumenting the small-scale masonry wall specimen.

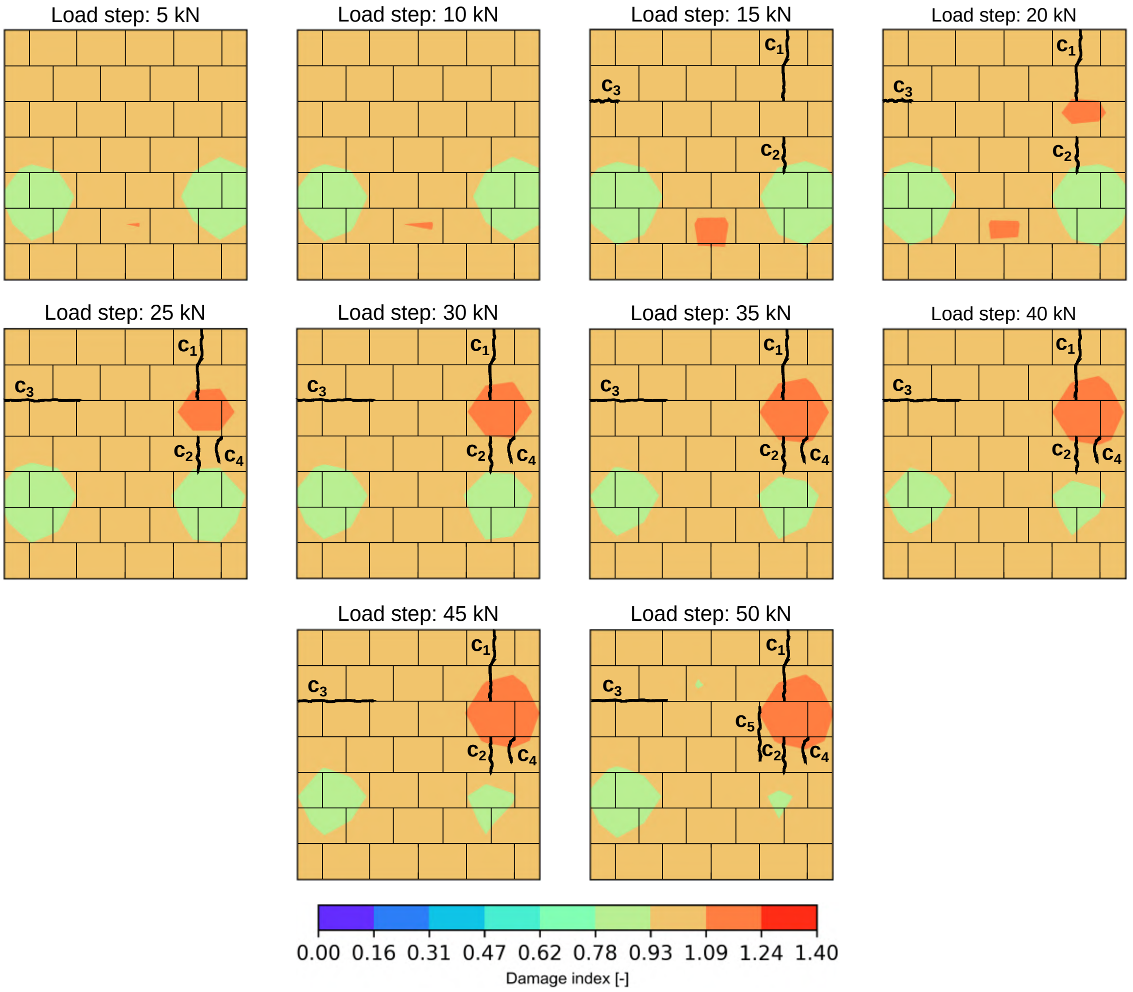

Figure 5.18: Damage index maps retrieved through the post-processing of the outputs from the RSGs instrumenting the small-scale masonry wall specimen.

5.4.3 Use of smart bricks deployed within a coarse sensor network

An URM building specimen, monitored by smart bricks deployed within a coarse sensor network, was subjected to shaking table tests by progressively increasing the seismic intensity of the shakes to induce growing damages to the structure. Results obtained in this case study are reported as follows.

5.4.3.1 Experimental and numerical cracking patterns

Developed cracking patterns, visually detected at the end of the ground motions, E1, E2, and E3, are depicted in Fig. 5.19. As expected, the performed white-noise inputs did not produce any visible damage on the building specimen, which maintained its sound state even after the execution of E1 earthquake (Fig. 5.19(a)). E2 earthquake induced the development of slight cracking patterns in façade 1 and 2, while cracks of similar severity, but less widespread, were also formed in façade 3 and 4. In both cases, damages were mainly located in the proximity of the openings of the corners, such as cracks C2, C3, and C7, or in the vicinity of the edges of the building, such as cracks C1, C4, C5, and C6 (Fig. 5.19(b)). The execution of E3 earthquake contributed to increase the existing cracking patterns by also producing the formation of new and extensive damages in façade 4 (Fig. 5.19(c)). It should be noted, however, that the tested mock-up was structurally sound and far from the collapse condition after the completion of the seismic sequence. Indeed, although damages affected diffuse areas of the construction, their severity was such that the integrity of the load-bearing structure was not compromised, as also demonstrated by the execution of the last white-noise input, WN4, which did not produce any modifications in the already formed cracking pattern. The performed shaking table test was numerically reproduced by defining a macromechanical 3D model of the URM building specimen. Damages that occurred to the mechanical model were detected through the assessment of the parameter d_t. The cracking patterns obtained by running the numerical simulation are illustrated in Fig. 5.20. Overall, they reasonably match the experimental cracking patterns reported in Fig. 5.19, even if some differences, in terms of crack initiation and propagation, can be detected. These were conceivably expected since considered unavoidable consequences of the macromechanical modeling approach adopted for the definition of the 3D model. Fig. 5.20(a) shows that no damage occurred to the model after the execution of the first seismic input, E1 earthquake, while the simulation of E2 earthquake produced damage initiation as shown in Fig. 5.20(b). It is worth noting that most of the damages developed at the portions of the 3D model close to the corners of the openings and in the neighborhood of the edges of the façades, as also experimentally experienced. Nevertheless, the mechanical model was also affected by diffuse damage developed in the vicinity of the concrete foundation curb that was not experimentally detected on the building specimen. The simulation of E3 earthquake induced the growth of the existing damaged areas of the model.

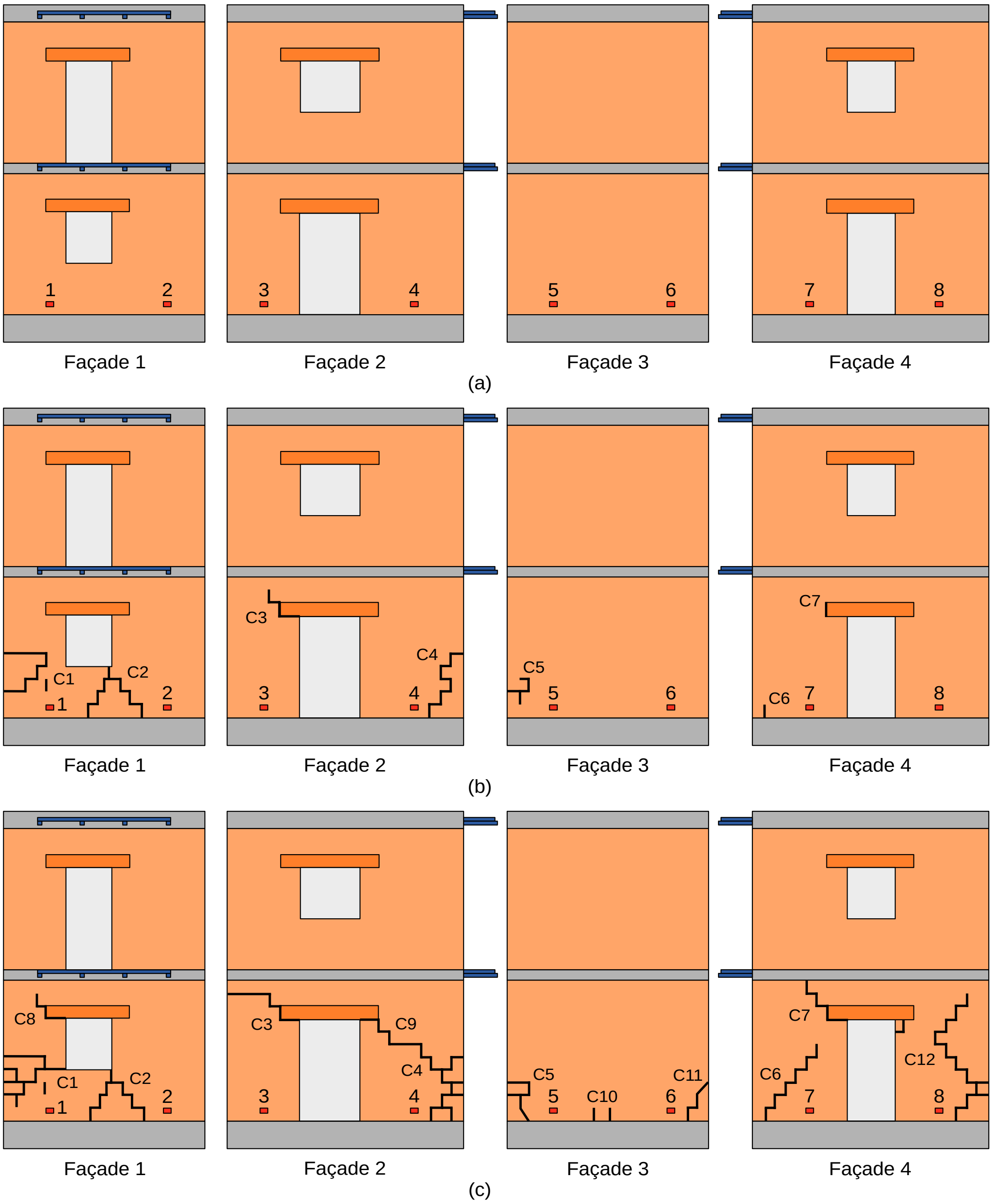

(a)

(b)

(c)

Fig. 5.19: Cracking patterns visually detected on the URM building specimen after the execution of the main shakes of the performed seismic sequence: (a) Cracks developed due to E1 earthquake; (b) Cracks developed due to E2 earthquake; (c) Cracks developed due to E3 earthquake.

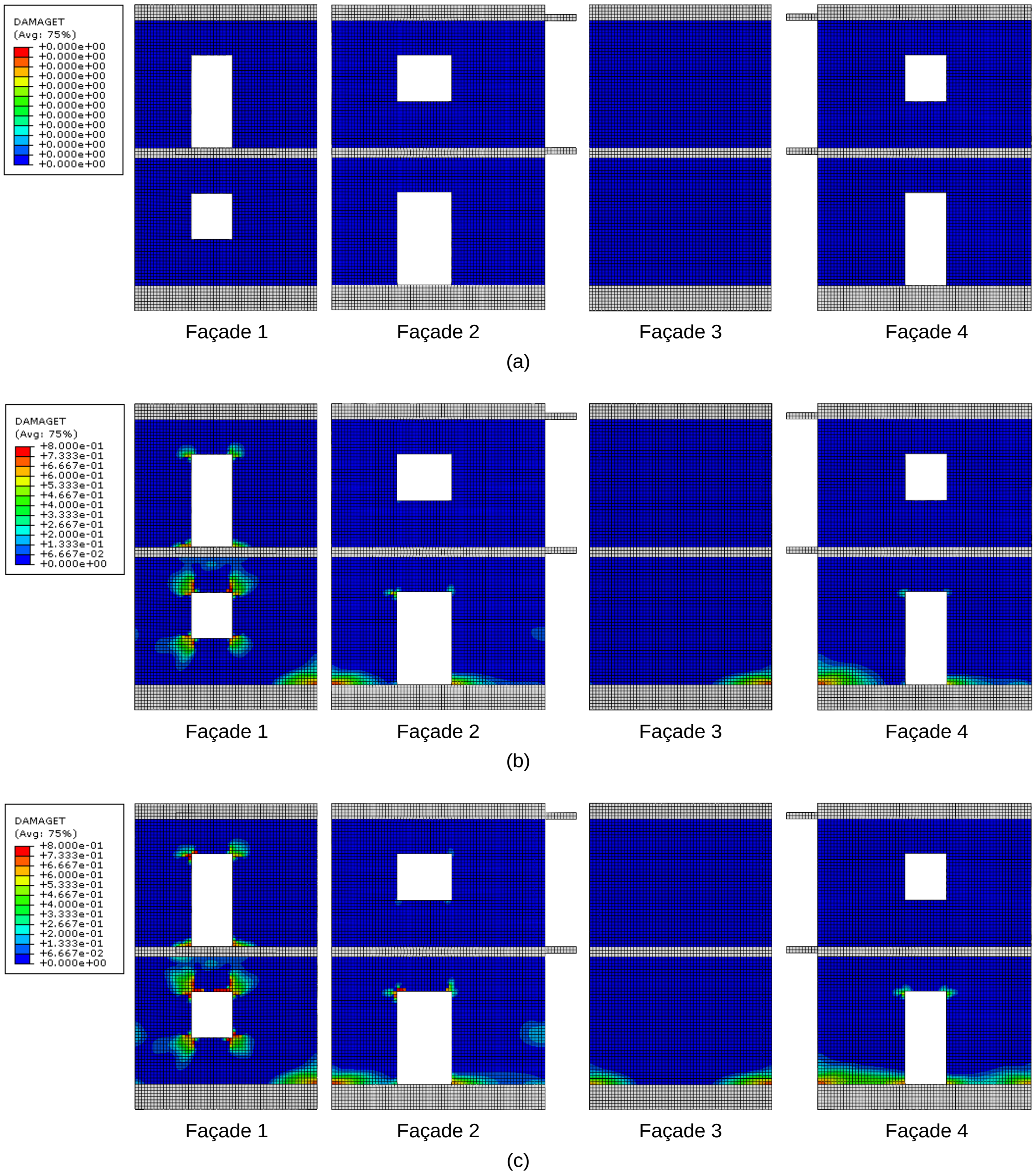

Fig. 5.20: Damages occurred to the 3D model by simulating the shaking table tests: (a) Damage produced by performing the records of E1 earthquake; (b) Damage produced by performing the records of E2 earthquake; (c) Damage produced by performing the records of E3 earthquake.

5.4.3.2 Experimental and numerical strain outputs

Fig. 5.21 reports changes in strain computed for the smart bricks embedded within the URM building specimen and for their corresponding solid elements forming the 3D model. It should be noted that a negative change in strain means that a reduction in the compressive strain occurred at the considered step of the performed seismic sequence with respect to the reference condition, WN1. Overall, the reported results demonstrated a fairly good match between the experimental and numerical trends, thus confirming the effectiveness of smart bricks in revealing the load paths redistributions that occurred internally to the URM building specimen due to the development of progressive damages. In particular, smart bricks revealed marked changes in strain in correspondence of the formation of the major cracking patterns visually detected after the execution of E2 and E3 earthquake. The performed white-noise inputs induced only slight variations in the measurements outputted by the novel sensors, indicating the occurrence of load paths redistributions of modest severity that are conceivably attributable to settlements due to pre-existing or newly formed irregularities in the bond pattern of the masonry. Solid elements of the 3D model were reasonably less influenced by such a phenomenon since settlements in the masonry are difficult to be numerically reproduced with the adopted macromechanical approach. The model was indeed affected by internal load paths redistributions only at the formation of damages due to the strongest seismic inputs. Differences between the experimental and numerical trends are observable in the plots regarding sensors 3, 4, 6, and 7, in which smart bricks present clear opposing trends with respect to those of their corresponding solid elements. These are likely due to a non-perfect match between the experimental and numerical cracking patterns developed in the façades where these sensors were inserted.

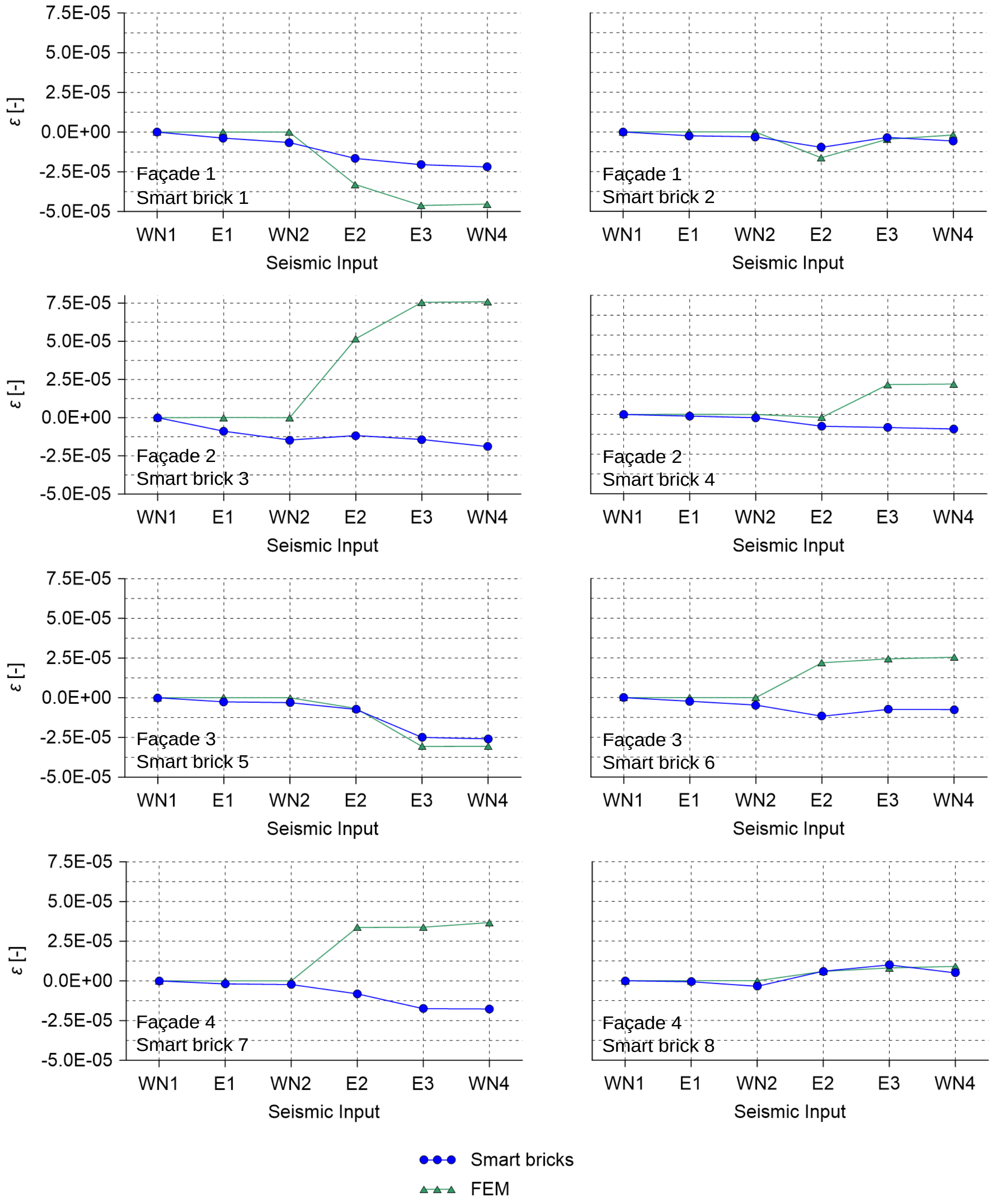

Fig. 5.21: Changes in strain computed for the smart bricks instrumenting the first floor of the URM building specimen and their corresponding solid elements within the 3D model. A negative variation in strain denotes a reduction in the dead load acting on the sensor.

5.4.3.3 Damage detection and localization

Changes in strain measured by smart bricks and their corresponding solid elements were therefore employed to detect and locate earthquake-induced damages on the URM building. In particular, trends of the experimental and numerical global damage indexes are represented in Fig. 5.22(a), with annotated the grade of severity of the damages visually detected after performing each seismic input according to "the classification of damage of masonry buildings" proposed in the European Macroseismic Scale 1998 (EMS98) (Grünthal 1998). Damages developed on the building specimen were rated with a maximum severity comprises between grade 2 and 3 of the EMS98, since grade 3 identifies widespread cracks of large extension and thickness, while cracks formed on the tested mock-up were of small thickness and detectable through a careful visual inspection even after the execution of E3 earthquake. Such a classification, therefore, confirms that the tested mock-up was far from its collapse condition after the completion of the performed seismic sequence, a circumstance that would correspond to the grade 5 of the EMS98. Reported trends of the damage indexes are consistent with the obtained experimental and numerical cracking patterns, indicating that damages progressively developed on the URM building specimen/3D model as the intensity of the seismic inputs increased. Results, therefore, prove the effectiveness of smart bricks for the global monitoring of the structural integrity of masonry constructions, since the post-processing of their strain measurements, by means of a simple algorithm, allowed the early detection of earthquake-induced damages on the tested mock-up. Experimental and numerical local damage indexes, computed for each façade and plotted in Fig. 5.22(b), complete the assessment of the health state of the monitored structure by adding further information concerning the localization of the damages. In particular, the local damage indexes computed with the outputs from smart bricks point out that façade 1 was the most damaged part of the building after performing E2 earthquake through a marked increase in the value of the local damage index corresponding to this circumstance. Similarly, the formation of a new cracking pattern in façade 4 after the execution of E3 earthquake can be well revealed by observing the trend of the index computed from smart bricks embedded in that area, which shows a noticeable increment at the step E3 of the performed seismic sequence. Overall, trends of the experimental local damage indexes denote that smart bricks effectively detected the load paths redistributions that occurred within the façades at each seismic input. Their more than acceptable agreement with the reported numerical trends highlights that smart bricks deployed within coarse sensor networks can be satisfactorily used to perform damage localization in masonry constructions under seismic loading.

Results achieved by computing the frequency decay in the numerical vibration frequencies of the 3D model are collected in Table 5.10. Being the mechanical model not affected by any damage, no variations in frequencies were computed in correspondence of E1 earthquake and white-noise input WN2, whereas marked decays were obtained in correspondence of E2 and E3 earthquakes, as expected. In particular, the first mode of vibration was the most affected by the development of damages to the model, since it was characterized by the largest decay in frequency among the other considered modes of vibration. Data collected in Table 5.10 were used to compute the global damage index of the frequency decay in numerical vibration frequencies, whose trend is reported in Fig. 5.23 together with the normalized global damage indexes from smart bricks and their corresponding solid elements. Overall, the comparison shows a good agreement among the results, which unanimously point out that the major damages occurred after the execution of E2 and E3 earthquakes. A broader assessment of the results achieved in terms of damage detection exploiting changes in strain obtained from smart bricks and decays in numerical vibration frequencies computed from the outputs of the 3D model, which would exemplify the vibration-based monitoring of the URM building specimen, highlights that the smart brick technology is a promising alternative not only to the traditional strain-based monitoring techniques but also to those based on the monitoring of modal features since its employment permitted a clear identification of the damages occurred to the tested mock-up by means of the use of affordable and fully integrable smart sensors along with a simple algorithm for the post-processing of strain measurements.

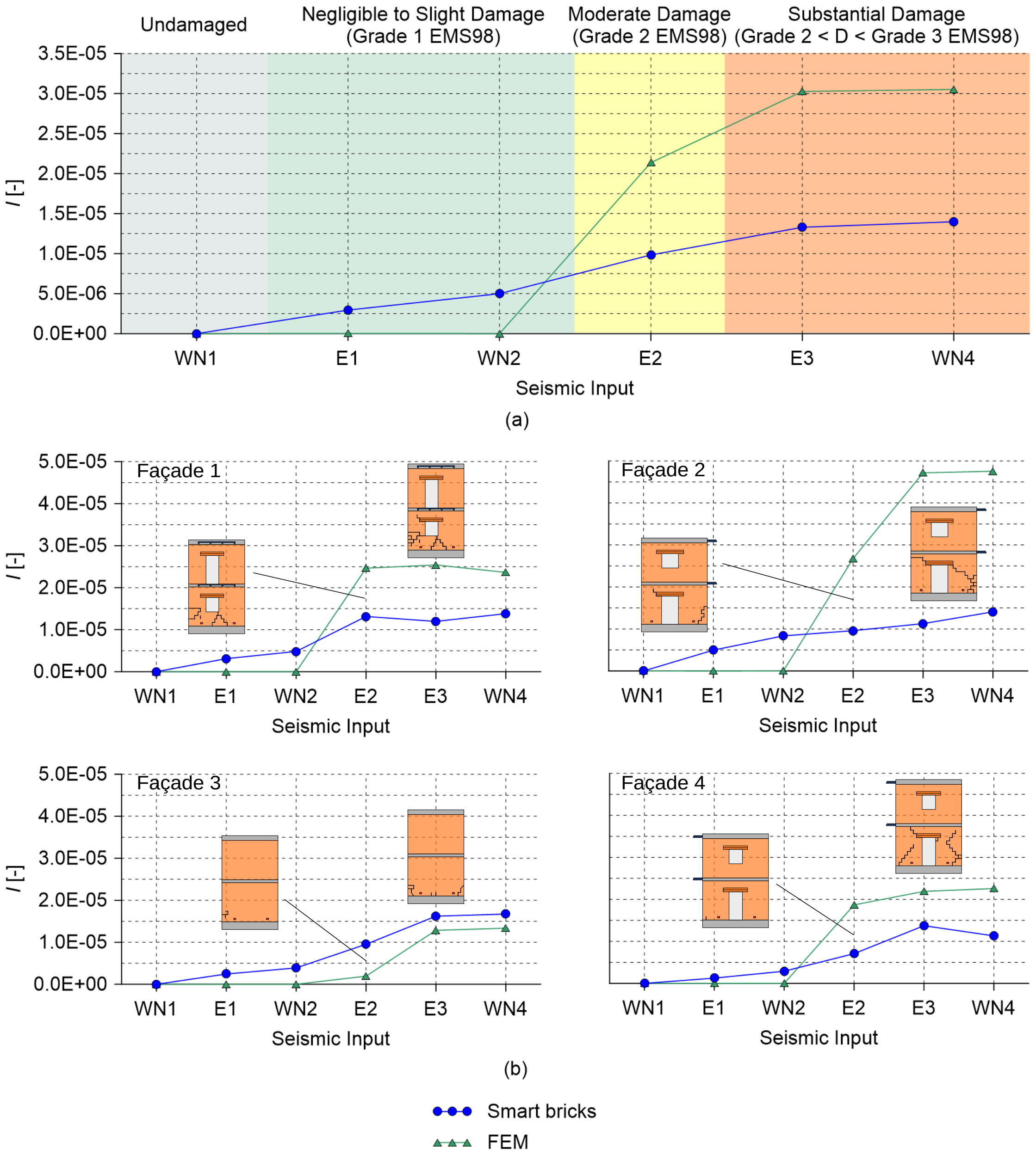

(a)

(b)

Fig. 5.22: Experimental and numerical damage indexes computed with data acquired from the smart bricks instrumenting the first floor of the URM building specimen and their corresponding solid elements within the 3D model: (a) Trends of global damage indexes. Damages occurred on the URM building specimen were classified according to the European Macroseismic Scale (EMS98, (Grünthal 1998)); (b) Trends of local damage indexes computed for each façade of the tested specimen.

Table 5.10: Results of the decay in the numerical vibration frequencies of the 3D model computed at each step of the simulated seismic sequence with respect to the reference condition WN1.

Mode	Variation E1-WN1 [%]	Variation WN2-WN1 [%]	Variation E2-WN1 [%]	Variation E3-WN1 [%]	Variation WN4-WN1 [%]
1	0.00	0.00	-0.97	-1.34	-1.35
2	0.00	0.00	-0.49	-1.15	-1.15
3	0.00	0.00	-0.58	-1.02	-1.02
4	0.00	0.00	-0.18	-0.34	-0.34
5	0.00	0.00	-0.11	-0.20	-0.20
6	0.00	0.00	-0.36	-0.79	-0.79
7	0.00	0.00	-0.61	-0.91	-0.92
8	0.00	0.00	-0.19	-0.31	-0.31
9	0.00	0.00	-0.26	-0.62	-0.62
10	0.00	0.00	-0.34	-0.60	-0.60
11	0.00	0.00	-0.42	-0.66	-0.66
12	0.00	0.00	-0.21	-0.38	-0.38
13	0.00	0.00	-0.50	-1.18	-1.18
14	0.00	0.00	-0.53	-1.04	-1.04
15	0.00	0.00	-0.30	-0.61	-0.62
16	0.00	0.00	-0.33	-0.61	-0.61
17	0.00	0.00	-0.60	-1.25	-1.25
18	0.00	0.00	-0.24	-0.40	-0.40
19	0.00	0.00	-0.39	-0.86	-0.86
20	0.00	0.00	-0.60	-1.03	-1.04

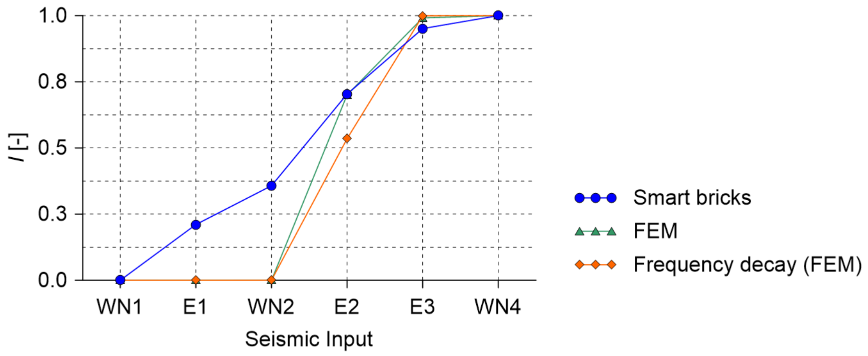

Fig. 5.23: Comparison between the experimental and numerical global damage indexes based on the assessment of strain measurements and the damage index computed by considering the decay in the numerical vibration frequencies of the 3D model.

5.5 Closing remarks

This chapter presented practical applications of the smart brick technology exemplifying the monitoring of strain in masonry constructions with such innovative strain-sensing devices, the smart bricks. In particular, the effectiveness of the novel sensors for the detection and localization of earthquake-induced damages in masonry structural elements was investigated.

A preliminary test proving the use of the series resistors model for the post-processing of the electrical outputs from smart bricks fully integrated within masonry structural settings was carried out. A small-scale masonry wall specimen instrumented with smart bricks was subjected to axial compression tests, hence the series resistors model was adopted to retrieve strain measurements from the embedded sensors. These were coherent with the simulated load case, highlighting the portion of the wall specimen where the load was applied as the most strained in compression. Moreover, changes in the trend of the strain measurements detected in correspondence of the development of cracks on the wall specimen demonstrated the effectiveness of smart bricks in revealing load paths redistributions when embedded within masonry structural elements. This key feature was exploited in the further case studies presented in this work for monitoring the development of damages on masonry structural elements through the post-processing of the strain measurements from smart bricks. In particular, two main strategies were proposed to exploit the outputs from the novel sensors for damage detection and localization purposes depending on the positioning of the sensors within the load-bearing structures.

An eccentric axial compression test performed on a small-scale masonry wall specimen demonstrated the use of the novel sensors for strain field reconstruction when deployed within masonry structural elements by forming dense sensor networks. Indeed, such a sensor array configuration permits the use of a suitable spatial interpolation method to post-process the outputs from the network, enabling a reliable reconstruction of the entire strain field in the monitored structural element. In this case, the spatially interpolated strain measurements from smart bricks were also employed to perform an effective identification of the damages that occurred to the tested structural element due to the increase in the applied compression load. The results from the novel sensors were also benchmarked against those obtained from RSGs, adhered to the embedded smart bricks, since these are probably the most common traditional strain-sensing devices used in practical applications for monitoring strain in masonry constructions. The obtained results demonstrated that smart bricks greatly outperform RSGs in damage detection and localization being the novel sensors directly embedded within the masonry, and therefore more sensitive to the modifications that occurred in the load paths within the tested structural element. The outputs from smart bricks were also interpreted with those extracted from a 3D model discretized according to the FE method to numerically reproduce the experiment. The obtained numerical results satisfactorily supported the experimental measurements provided by the embedded smart bricks.

The use of smart bricks deployed in coarse sensor networks was instead demonstrated by subjecting an URM building specimen, instrumented with the novel sensors, to shaking table tests. In this case, ground motions of increasing seismic intensity were performed to produce progressive damages to the structure. Since this time the positioning of smart bricks did not allow the spatial interpolation of their outputs, the strain measurements from the novel sensors were assessed by seeking changes in their trend with respect to a reference condition at witch the tested mock-up was considered in a sound state. The obtained experimental trends of changes in strain from the embedded smart bricks were compared with those retrieved from a 3D model simulating the experiment. Overall, smart bricks allowed the early detection and localization of the damages that occurred to the building specimen, thus confirming the effectiveness of these innovative piezoresistive brick-like sensors for the post-earthquake assessment of masonry constructions.

Chapter 6

Conclusions

This Thesis work addressed the development of the smart bricks that are nano- or micro-composite clay bricks able to work as smart strain sensors for masonry structures. The work included the design and the preparation of the novel sensors until reaching their application on masonry elements and structures for damage detection and post-earthquake assessment.

Smart bricks are designed by leveraging the concept of smart materials, hence by doping the clay, commonly used in the production process of the conventional bricks, with an electrically conductive filler specifically selected to obtain a composite material with improved electrical properties and enhanced piezoresistive capabilities. Accordingly, a modification in the strain condition of a doped brick results in a measurable change in its internal electrical resistance (e.g., an increase in the compressive strain state of a smart brick due to the application of a compression load on the sensor induces a decrease in its electrical resistance). This electromechanical behavior allows the monitoring of the strain field in masonry structural elements equipped with such novel sensors through the correlation of the changes in the strain state and the variations in the electrical outputs of the smart bricks.

The main contribution of this work is therefore the development of smart sensors suitable to achieve a feasible and effective monitoring of the structural response of masonry constructions during their service life, overcoming the issues related to the application of traditional sensing technologies, and allowing the large scale and distributed employment of innovative smart seismic SHM systems to either new or existing masonry structures. Considering the well-known vulnerability, including fragile collapse mechanisms, under earthquake loading demonstrated by ancient masonry constructions during the last decades, the smart bricks represent an effective tool for the real-time monitoring of masonry constructions, the protection of human lives, and the preservation of the integrity of the cultural heritage.

Chapter 2 reported a review of the state-of-the-art concerning the use of strain measurements for monitoring masonry constructions. Pros and cons of traditional SHM approaches based on the assessment of the changes in strain were discussed. Such techniques, in particular, outperform SHM approaches involving the evaluation of global parameters, like the modal features, for the tracking of damages locally developing in masonry constructions. Monitoring strategies employing piezoresistive strain sensors were presented as an alternative solution to the traditional strain-based SHM techniques. This innovative concept of self-sensing materials was first employed for the production of smart sensors for SHM of concrete constructions, then extended to masonry structures in more recent times. Despite the promising results reached in this field, the development of smart sensing solutions for SHM of masonry constructions is still in its infancy.

Chapter 3 presented a literature review on the modeling strategies for masonry constructions, handling the classification on the basis of the scale at which the masonry is analyzed. Modeling techniques were therefore classified by identifying two main categories: micromechanical and macromechanical approaches. While the first approaches discretize bricks, mortar layers, and their interaction according to the corresponding mechanical properties, macromechanical approaches smear out the masonry components in an equivalent continuum characterized by homogenized mechanical parameters. Pros and cons of both alternatives were critically reported. Nevertheless, the choice of a strategy rather than another often depends, as in the case of this work, on the geometrical size of the masonry construction being modeled. Micromechanical approaches are therefore employed for the modeling of masonry structural elements with a high level of accuracy, while macromechanical strategies are chosen when dealing with large structures for which approximations in the models are often necessary to ensure an adequate computational efficiency. Details concerning the computational tools and FE analysis adopted in this work to build, discretize, and analyze the mechanical models were also reported, thus supporting the computational strategies adopted in Chapter 5, in which the models developed for this work were described and employed to interpret the obtained experimental results. In particular, the plastic-damage model considered in this work to numerically simulate the nonlinear mechanical behavior of the masonry in both tension and compression was fully introduced. It should be noted that among the peculiarities of this constitutive model there is the possibility to reproduce the development of damages in the material being simulated by means of the progressive degradation of its elastic stiffness.

Chapter 4 dealt with the development of a new formulation of the smart bricks, presenting the production process of these novel sensors, the electromechanical model describing their strain-sensing behavior, and a campaign of laboratory tests aimed at achieving a comprehensive characterization of their electrical, electromechanical, physical, and mechanical properties. An investigation on the environmental effects on the electrical outputs of the novel sensors was also addressed, with a specific focus on the issue of temperature and humidity effects compensation. Considering the state-of-the-art of the smart brick technology reviewed in Chapter 2, the following novelties were introduced through this chapter in this promising approach for seismic SHM of masonry constructions:

- Stainless steel microfibers were selected as conductive filler for producing smart bricks;
- External copper plate electrodes were proposed to perform electrical measurements from smart bricks for strain-sensing purposes;
- Resin stripes electrodes were designed to measure the internal electrical properties of the smart bricks without contact resistance;
- A novel electromechanical model, called series resistors model, linking the sensing due to the piezoresistive capabilities of the smart bricks and the sensing at the contact resistance developed at the copper plate electrodes, was proposed to properly describe the strain-sensing behavior of the novel sensors.

The main results achieved in the investigations carried out for the characterization of the proposed new formulation of the smart bricks are listed below.
Concerning the electrical tests:

- The addition of steel fibers to the clay matrices enhances the electrical properties of the smart bricks with respect to those of bricks made with plain clay;

- The percolative behavior of the smart bricks is characterized by two percolation thresholds: the first due to the dispersion of the steel fibers within the clay, the second due to the conductive paths further developed between the metallic inclusions, intrinsically present in the clay, and the dispersed steel fibers;
- The external copper plate electrodes are more suitable for conducting electrical measurements with this new formulation of smart bricks compared to the previously adopted internal stainless steel electrodes.

Concerning the electromechanical tests:

- The addition of a content of steel fibers equal to 0.25% or 0.50%, with respect to the weight of fresh clay, greatly improves the electromechanical properties of the smart bricks compared to those of the bricks made with plain clay;
- The efficiency of the proposed series resistors model in describing the strain-sensing behavior of the smart bricks under increasing compression loads was proved. Experiments also demonstrated that the addition of steel fibers to the clay matrices enhances the sensing due to the piezoresistivity of the material, as well as that attributable to the contact resistance, compared to bricks made with plain clay;
- The effectiveness of smart bricks in measuring strain was demonstrated by benchmarking their outputs versus those from traditional resistive strain gauges (RSGs). From this comparison, smart bricks appear more suitable than RSGs for SHM of masonry constructions since capable of better describing the nonlinear response of the bricks under compression;
- Both formulations of smart bricks made with a content of steel fibers equal to 0.25% and 0.50%, possessing similar sensing capabilities, can be employed for monitoring strain in masonry constructions. For particular applications in which high strain-sensing capabilities are required, smart bricks made of 0.50% of steel fibers can be preferred. In other cases, smart bricks made with a content of steel fibers of 0.25% fit well.

Concerning CT scan, compression, and three-point bending tests:

- Smart bricks made with a content of steel fibers equal to 0.25% or 0.50%, with respect to the weight of fresh clay, possess an internal macroporous structure, with dispersed metallic inclusions, which is similar to that of the conventional clay bricks.

Experiments also proved that a more uniform dispersion of the steel fibers within the clay matrices can be achieved by increasing the content of filler used for the production of the novel sensors;

- Smart bricks made with a content of steel fibers equal to 0.25% or 0.50%, with respect to the weight of fresh clay, possess an elastic modulus and compressive strength that are comparable to those of the conventional clay bricks;
- Smart bricks made with a content of steel fibers equal to 0.25% or 0.50%, with respect to the weight of fresh clay, possess a fracture energy that is comparable to those of the conventional clay bricks.

Concerning environmental effects on the electrical outputs:

- A marked negative correlation was found between changes in temperature and changes in electrical resistance of the smart bricks, whereby an increase in the temperature determines a decrease in the total electrical resistance of the novel sensors;
- Daily changes in relative humidity do not significantly affect the electrical measurements acquired from the smart bricks. This is valid as long as a change in humidity remains stable for a period less than the time required by water particles to infiltrate within the internal macroporous structure of the bricks;
- Conventional clay bricks and smart bricks react in a similar way to the changes in temperature and humidity;
- Effects of the daily changes in temperature can be compensated from the total electrical resistance of the smart bricks by using a linear regressive model.

Chapter 5 presented some meaningful experimental applications of the smart brick technology investigating its effectiveness for monitoring strain in masonry structural elements or entire buildings, as well as for the detection and localization of damages due to earthquake loading. Considering the state-of-the-art of the smart brick technology reviewed in Chapter 2, the novelties introduced through this chapter in this promising approach for seismic SHM of masonry constructions are mainly focused on the methodologies adopted for the post-processing of the strain measurements from the novel sensors according to their deployment in the structure being monitored. Along these lines:

- A methodology of data post-processing was proposed considering smart bricks deployed in a dense sensor network. Here, the spatial interpolation of the strain measurements from the novel sensors allows the strain field reconstruction, as well as the detection and localization of damages;
- A methodology of data post-processing was proposed considering smart bricks deployed in a coarse sensor network. In this case, strain measurements from smart bricks are benchmarked against baseline data referring to an initial condition of the structure being monitored allowing strain monitoring along with the detection and localization of damages.

The main results achieved in the case studies reported in this chapter are listed below:

- The effectiveness of the series resistors model in retrieving strain measurements through the post-processing of the electrical outputs from smart bricks embedded within a typical structural setting was proved;
- Smart bricks deployed in a dense sensor network allowed the strain field reconstruction in a masonry wall specimen eccentrically loaded in compression in its plane, as well as the detection and localization of damages developed on the tested structural element by increasing the applied load. The comparison between the results obtained from smart bricks and those from traditional RSGs, applied in correspondence of the novel sensors embedded in the wall specimen, demonstrated the smart bricks outperform RSGs for strain field reconstruction and damage detection and localization in masonry structures. Results from smart bricks were also in a good agreement with those obtained from a mechanical model built to numerically simulate the test;
- Smart bricks deployed in a coarse sensor network allowed the detection and localization of earthquake-induced damages developed on an URM building specimen subjected to shaking table tests of increasing seismic intensity. In particular, the obtained results permitted to achieve a satisfactory comprehension of the major cracking patterns developed on the tested mock-up, as well as the identification of the portions of the building most affected by damages. A good agreement was found by benchmarking the experimental results from smart bricks against those obtained from a mechanical model built to numerically simulate the test.

According to this, it is worth remarking the main aspects for which the use of the smart bricks should be preferred to the use of strain-sensing devices currently available on the market for seismic SHM of masonry constructions:

- Smart bricks are made of a composite material possessing physical and mechanical properties similar to those of the conventional clay bricks. This results in sensors durable in time and capable of providing strain measurements truly representative of the mechanical response of a brick strained in compression;
- Smart bricks can be embedded within a load-bearing structure without altering its structural response, including portions of a building not inspectable during its service life. This allows the novel sensors to reveal changes in strain even of small magnitude, as well as overcoming sensor deployment issues due to aesthetic and architectural limitations characterizing historical masonry constructions;
- Strain measurements from smart bricks can be post-processed through fairly simple algorithms, which at the same time are very effective for the assessment of critical conditions that may occur to a masonry construction. The novel sensors can therefore aid the detection and localization of portions of a building interested by high strain concentrations/relaxations, as well as those affected by the development of damages. As proven, smart bricks are effective for the identification of earthquake-induced damages at a very early stage, however, their use can be extended for the monitoring of constructions under differential foundation settlements, aging of materials, and the other typical structural pathologies affecting masonry buildings.

Insights for further studies aimed at the improvement of the smart brick technology can be also derived from this research work. Some of the most relevant ones are listed below:

- The employment of industrial instrumentation and quality checks in the production process of the smart bricks should be considered and assessed with the aim of improving the repeatability of the electromechanical properties of the novel sensors. Alternative dispersion methodologies can be also investigated;
- The bonding between smart bricks and the neighboring masonry components should be mechanically characterized to evaluate the influence of the insulating polymeric tape, currently adopted for limiting the propagation of the current flow within each sensor, in the mechanical response of the masonry;
- A methodology for the replacement of brick units with smart bricks in existing masonry structures has not yet been proposed. The operation of the novel sensors after the post-construction insertion should be experimentally demonstrated;

- Other input-output regression models, as well as input-only models, can be explored for compensating the environmental effects from the total electrical resistance of the smart bricks;
- The validation of the proposed damage detection and localization methods should be also carried out by considering applications of the smart brick technology to full-scale masonry building specimens subjected to controlled damages of non-seismic nature;
- A specific electronic hardware should be developed to perform electrical measurements from smart bricks, thus proposing even less invasive SHM systems for masonry structures, in particular for the ancient ones.

Overall, the Ph.D. thesis demonstrated that the smart bricks developed in this work can be considered an effective smart sensing solution for seismic SHM of masonry constructions ready for achieving a higher Technology Readiness Level (TRL) and for field validations.

Bibliography

Abdulla, Kurdo F, Lee S Cunningham, and Martin Gillie (2017). “Simulating masonry wall behaviour using a simplified micro-model approach”. In: *Engineering Structures* 151, pp. 349–365.

Addessi, Daniela, S Marfia, E Sacco, and J Toti (2014). “Modeling approaches for masonry structures”. In: *The Open Civil Engineering Journal* 8.1.

Alaggio, Rocco, Angelo Aloisio, Elena Antonacci, and Riccardo Cirella (2020). “Two-years static and dynamic monitoring of the Santa Maria di Collemaggio basilica”. In: *Construction and Building Materials*, p. 121069.

Anand, Sandeep V and D Roy Mahapatra (2009). “Quasi-static and dynamic strain sensing using carbon nanotube/epoxy nanocomposite thin films”. In: *Smart Materials and Structures* 18.4, p. 045013.

Angjeliu, Grigor, Dario Coronelli, and Giuliana Cardani (2020). “Development of the simulation model for Digital Twin applications in historical masonry buildings: The integration between numerical and experimental reality”. In: *Computers & Structures* 238, p. 106282.

Azhari, Faezeh and Nemkumar Banthia (2012a). “Cement-based sensors with carbon fibers and carbon nanotubes for piezoresistive sensing”. In: *Cement and Concrete Composites* 34.7, pp. 866–873.

— (2012b). “Cement-based sensors with carbon fibers and carbon nanotubes for piezoresistive sensing”. In: *Cement and Concrete Composites* 34.7, pp. 866–873.

Bao, Xiaoyi and Liang Chen (2012). “Recent progress in distributed fiber optic sensors”. In: *sensors* 12.7, pp. 8601–8639.

Berger, JR and JW Dally (1988). “An overdeterministic approach for measuringK I using strain gages”. In: *Experimental Mechanics* 28.2, pp. 142–145.

Birgin, H., Antonella D'Alessandro, and Filippo Ubertini (Aug. 2020). "Smart Graphite–Cement Composite for Roadway-Integrated Weigh-In-Motion Sensing". In: *Sensors* 20, p. 4518. DOI: `10.3390/s20164518`.

Bradski, G. (2000). "The OpenCV Library". In: *Dr. Dobb's Journal of Software Tools*.

Cacciotti, Riccardo, Jaroslav Valach, and Benjamin Wolf (2018). "Innovative and easy-to-implement moisture monitoring system for brick units". In: *Construction and Building Materials* 186, pp. 598–614.

Carrara, Pietro, Rolands Kruse, Dale P Bentz, M Lunardelli, Thorsten Leusmann, PA Varady, and Laura De Lorenzis (2018). "Improved mesoscale segmentation of concrete from 3D X-ray images using contrast enhancers". In: *Cement and Concrete Composites* 93, pp. 30–42.

Cavalagli, Nicola, Matteo Ciano, Gianluca Fagotti, Massimiliano Gioffrè, Vittorio Gusella, and Chiara Pepi (2020). "Shaking Table Investigation on the Masonry Structures Behaviour to Earthquakes with Strong Vertical Component". In: *Nonlinear Dynamics of Structures, Systems and Devices*. Springer, pp. 337–345.

Chen, Zengtao and Abdolhamid Akbarzadeh (2020). "Multiphysics of Smart Materials and Structures". In: *Advanced Thermal Stress Analysis of Smart Materials and Structures*. Springer, pp. 65–117.

Chung, D. D. L. (2002). "Piezoresistive Cement-Based Materials for Strain Sensing". In: *Journal of Intelligent Material Systems and Structures* 13.9, pp. 599–609. DOI: `10.1106/104538902031861`.

Cińcio, A and A Wawrzynek (2005). "Plastic-damage macro-model for non-linear masonry structures subjected to cyclic or dynamic loads". In: *Analytical Models and New Concepts in Concrete and Masonry Structures AMCM2005*, pp. 131–132.

Circolare esplicativa del 02.02.2009 contenente "Istruzioni per l'applicazione delle nuove norme tecniche per le costruzioni di cui al D.M. 17.01.2018" (2009). (In Italian).

Clementi, F, A Pierdicca, A Formisano, F Catinari, and S Lenci (2017). "Numerical model upgrading of a historical masonry building damaged during the 2016 Italian earthquakes: the case study of the Podestà palace in Montelupone (Italy)". In: *Journal of Civil Structural Health Monitoring* 7.5, pp. 703–717.

Cluni, Federico and Vittorio Gusella (2004). "Homogenization of non-periodic masonry structures". In: *International Journal of Solids and Structures* 41.7, pp. 1911–1923.

Cochrane, Cédric, Vladan Koncar, Maryline Lewandowski, and Claude Dufour (2007). "Design and development of a flexible strain sensor for textile structures based on a conductive polymer composite". In: *Sensors* 7.4, pp. 473–492.

Compán, Víctor, Pablo Pachón, Margarita Cámara, Paulo B Lourenço, and Andrés Sáez (2017). "Structural safety assessment of geometrically complex masonry vaults by non-linear analysis. The Chapel of the Würzburg Residence (Germany)". In: *Engineering Structures* 140, pp. 1–13.

Coppola, Luigi, Alessandra Buoso, and Fabio Corazza (2011). "Electrical properties of carbon nanotubes cement composites for monitoring stress conditions in concrete structures". In: *Applied Mechanics and Materials* 82, pp. 118–123.

Cressie, Noel (1992). "Statistics for spatial data". In: *Terra Nova* 4.5, pp. 613–617.

D'Alessandro, Antonella, Marco Rallini, Filippo Ubertini, Annibale Luigi Materazzi, and Jose Maria Kenny (2016). "Investigations on scalable fabrication procedures for self-sensing carbon nanotube cement-matrix composites for SHM applications". In: *Cement and Concrete Composites* 65, pp. 200–213.

Dally, JW and RJ Sanford (1987). "Strain-gage methods for measuring the opening-mode stress-intensity factor, K I". In: *Experimental Mechanics* 27.4, pp. 381–388.

D'Altri, Antonio, Stefano Miranda, Giovanni Castellazzi, and Vasilis Sarhosis (June 2018). "A 3D detailed micro-model for the in-plane and out-of-plane numerical analysis of masonry panels". In: *Computers Structures* 206. DOI: `10.1016/j.compstruc.2018.06.007`.

D'Altri, Antonio et al. (Aug. 2019). "Modeling Strategies for the Computational Analysis of Unreinforced Masonry Structures: Review and Classification". In: *Archives of Computational Methods in Engineering.* DOI: `10.1007/s11831-019-09351-x`.

De Fino, Mariella and Giambattista De Tommasi (2008). "Structural Health Monitoring of Historical Buildings Using Fibre Optic Sensors". In:

De Lorenzis, Laura, Matthew DeJong, and John Ochsendorf (2007). "Failure of masonry arches under impulse base motion". In: *Earthquake Engineering & Structural Dynamics* 36.14, pp. 2119–2136.

Derakhshan, Hossein, Phillip Visintin, and Michael C Griffith (2017). "Case studies of material properties of late nineteenth-century unreinforced masonry buildings in Adelaide". In: *Australian Journal of Civil Engineering* 15.2, pp. 109–116.

Ding, Siqi, Yanfeng Ruan, Xun Yu, Baoguo Han, and Yi-Qing Ni (2019). "Self-monitoring of smart concrete column incorporating CNT/NCB composite fillers modified cementitious sensors". In: *Construction and Building Materials* 201, pp. 127–137.

Dolce, M, FC Ponzo, C Moroni, D Nigro, A Goretti, F Giordano, G De Canio, and R Marnetto (2008). "3d dynamic tests on 2/3 scale masonry buildings retrofitted with different systems". In: *Proceeding of the 14th world conference on earthquake engineering* China.

Dolce, Mauro, Felice Carlo Ponzo, M Di Croce, C Moroni, F Giordano, D Nigro, and R Marnetto (2009). "Experimental assessment of the CAM and DIS-CAM systems for the seismic upgrading of monumental masonry buildings". In: *Proceedings of the 1st International Conference on Protection of Historical Constructions, Rome, Italy* 2628.

Downey, Austin, Antonella D'Alessandro, Micah Baquera, Enrique García-Macías, Daniel Rolfes, Filippo Ubertini, Simon Laflamme, and Rafael Castro-Triguero (2017a). "Damage detection, localization and quantification in conductive smart concrete structures using a resistor mesh model". In: *Engineering Structures* 148, pp. 924–935.

Downey, Austin, Antonella D'Alessandro, Simon Laflamme, and Filippo Ubertini (2017b). "Smart bricks for strain sensing and crack detection in masonry structures". In: *Smart Materials and Structures* 27.1, p. 015009.

Downey, Austin, Antonella D'Alessandro, Filippo Ubertini, Simon Laflamme, and Randall Geiger (2017c). "Biphasic DC measurement approach for enhanced measurement stability and multi-channel sampling of self-sensing multi-functional structural materials doped with carbon-based additives". In: *Smart Materials and Structures* 26.065008, p. 6.

Duvnjak, Ivan, Domagoj Damjanović, and Joško Krolo (2016). "Structural health monitoring of cultural heritage structures: applications on peristyle of Diocletian's palace in split". In: *8th European workshop on structural health monitoring, EWSHM*. Vol. 4, pp. 2661–2669.

European Committee, for Standardization (1992). *EN 1992 Eurocode 2: Design of concrete structures.*

— (1993). *EN 1993 Eurocode 3: Design of steel structures.*

— (1996). *EN 1996 Eurocode 6: Design of masonry structures.*

Formisano, Antonio, Generoso Vaiano, Francesco Fabbrocino, and Gabriele Milani (2018). "Seismic vulnerability of Italian masonry churches: The case of the Nativity of Blessed Virgin Mary in Stellata of Bondeno". In: *Journal of Building Engineering* 20, pp. 179–200.

Galao, O, F Javier Baeza, Emilio Zornoza, and Pedro Garcés (2014). "Strain and damage sensing properties on multifunctional cement composites with CNF admixture". In: *Cement and concrete composites* 46, pp. 90–98.

Gandhi, Mukesh V and BD Thompson (1992). *Smart materials and structures*. Springer Science & Business Media.

García-Macías, Enrique, Rafael Castro-Triguero, Andrés Sáez, and Filippo Ubertini (2018a). "3D mixed micromechanics-FEM modeling of piezoresistive carbon nanotube smart concrete". In: *Computer Methods in Applied Mechanics and Engineering* 340, pp. 396–423.

García-Macías, Enrique, Luis Rodríguez-Tembleque, Andrés Sáez, and Filippo Ubertini (2018b). "Crack detection and localization in RC beams through smart MWCNT/epoxy strip-like strain sensors". In: *Smart Materials and Structures* 27.11, p. 115022.

García-Macías, Enrique and Filippo Ubertini (2019). "Earthquake-induced damage detection and localization in masonry structures using smart bricks and Kriging strain reconstruction: A numerical study". In: *Earthquake Engineering & Structural Dynamics* 48.5, pp. 548–569.

Gentile, Carmelo, Marco Guidobaldi, and Antonella Saisi (2016). "One-year dynamic monitoring of a historic tower: damage detection under changing environment". In: *Meccanica* 51.11, pp. 2873–2889.

Gentile, Carmelo, Antonello Ruccolo, and Antonella Saisi (2019). "Continuous Dynamic Monitoring to Enhance the Knowledge of a Historic Bell-Tower". In: *International Journal of Architectural Heritage*, pp. 1–13.

Glisic, Branko, David L Hubbell, Dorotea H Sigurdardottir, and Yao Yao (2013). "Damage detection and characterization using long-gauge and distributed fiber optic sensors". In: *Optical Engineering* 52.8, p. 087101.

Glisic, Branko and Daniele Inaudi (2008). *Fibre optic methods for structural health monitoring.* John Wiley & Sons.

Glisic, Branko and Naveen Verma (2011). "Very dense arrays of sensors for SHM based on large area electronics". In: *8th International Workshop on Structural Health Monitoring 2011: Condition-Based Maintenance and Intelligent Structures*, pp. 1409–1416.

Gorini, Antonella, Mario Nicoletti, Paolo Marsan, Riccardo Bianconi, Rita De Nardis, Luisa Filippi, Sandro Marcucci, Franco Palma, and Elisa Zambonelli (2010). "The Italian strong motion network". In: *Bulletin of Earthquake Engineering* 8.5, pp. 1075–1090.

Grünthal, Gottfried (1998). *European macroseismic scale 1998.* Tech. rep. European Seismological Commission (ESC).

Habel, Wolfgang R and Katerina Krebber (2011). "Fiber-optic sensor applications in civil and geotechnical engineering". In: *Photonic Sensors* 1.3, pp. 268–280.

Han, Baoguo, Xun Yu, and Eil Kwon (2009). "A self-sensing carbon nanotube/cement composite for traffic monitoring". In: *Nanotechnology* 20.44, p. 445501.

Han, Baoguo, Xun Yu, and Jinping Ou (2011). “Multifunctional and smart carbon nanotube reinforced cement-based materials”. In: *Nanotechnology in civil infrastructure*, pp. 1–47.

Heijs, Anton WJ, J De Lange, JF Th Schoute, and J Bouma (1995). “Computed tomography as a tool for non-destructive analysis of flow patterns in macroporous clay soils”. In: *Geoderma* 64.3-4, pp. 183–196.

Heise, Richard E (1965). “Low-cycle fatigue-crack indications by strain gages operating in elastic strain fields”. In: *Experimental Mechanics* 5.4, 19A–24A.

Hibbett, Karlsson, and Sorensen (1998). *ABAQUS/Standard User’s Manual.* Hibbitt, Karlsson Sorensen.

Hilding, Jenny, Eric A Grulke, Z George Zhang, and Fran Lockwood (2003). “Dispersion of carbon nanotubes in liquids”. In: *Journal of dispersion science and technology* 24.1, pp. 1–41.

Hillerborg, Arne, Mats Modéer, and P-E Petersson (1976). “Analysis of crack formation and crack growth in concrete by means of fracture mechanics and finite elements”. In: *Cement and concrete research* 6.6, pp. 773–781.

Honda, Riki and Sumio Sawada (1992). “Time integration scheme that eliminates high frequency noise by digital filter”. In: *Proceedings of 10th world conference on earthquake engineering*, pp. 19–24.

Horn, Roger A and Charles R Johnson (1990). “Norms for vectors and matrices”. In: *Matrix analysis*, pp. 313–386.

Hou, T. C. and Jerome P. Lynch (2005). “Conductivity-based strain monitoring and damage characterization of fiber reinforced cementitious structural components”. In: *SPIE Smart Structures and Materials + Nondestructive Evaluation and Health Monitoring.*

Ivorra, Salvador and Francisco J Pallarés (2006). “Dynamic investigations on a masonry bell tower”. In: *Engineering structures* 28.5, pp. 660–667.

Jones, Eric, Travis Oliphant, and Pearu Peterson (2001). “SciPy: Open source scientific tools for Python”. In:

Jørgensen, Sven Erik and Giuseppe Bendoricchio (2001). *Fundamentals of ecological modelling.* Vol. 21. Elsevier.

Kita, Alban, Nicola Cavalagli, and Filippo Ubertini (2019). “Temperature effects on static and dynamic behavior of Consoli Palace in Gubbio, Italy”. In: *Mechanical Systems and Signal Processing* 120, pp. 180–202.

Krige, D.G. (1951). “A statistical approach to some basic mine valuation problems on the Witwatersrand”. In: *Journal of the Southern African Institute of Mining and Metallurgy* 52.6, pp. 119–139. ISSN: 0038-223X.

Krstevska, L, Lj Tashkov, N Naumovski, G Florio, A Formisano, A Fornaro, and R Landolfo (2010). “In-situ experimental testing of four historical buildings damaged during the 2009 L’Aquila earthquake”. In: *COST ACTION C26: Urban Habitat Constructions under Catastrophic Events - Proceedings of the Final Conference* 26, pp. 427–432.

Kuang, JH and LS Chen (1995). “A single strain gage method for KI measurement”. In: *Engineering Fracture Mechanics* 51.5, pp. 871–878.

Laflamme, Simon, Liang Cao, Eleni Chatzi, and Filippo Ubertini (2016a). “Damage detection and localization from dense network of strain sensors”. In: *Shock and Vibration* 2016.

— (2016b). “Damage detection and localization from dense network of strain sensors”. In: *Shock and Vibration* 2016.

Laflamme, Simon, David Eisenmann, Kejin Wang, Filippo Ubertini, Irvin Pinto, and Akira DeMoss (2018). “Smart Concrete for Enhanced Nondestructive Evaluation”. In: *Materials Evaluation* 76.10, pp. 1395–1404.

Lagomarsino, Sergio (2006). “On the vulnerability assessment of monumental buildings”. In: *Bulletin of Earthquake Engineering* 4.4, pp. 445–463.

Lee, Jeeho and Gregory L Fenves (1998). “Plastic-damage model for cyclic loading of concrete structures”. In: *Journal of engineering mechanics* 124.8, pp. 892–900.

Libecajtová, Aneta (2020). “Numerical Analysis of Compressed Masonry Columns”. In: *Periodica Polytechnica Civil Engineering*.

Liehr, Sascha, Philipp Lenke, Mario Wendt, Katerina Krebber, Monika Seeger, Elke Thiele, Heike Metschies, Berhane Gebreselassie, and Johannes Christian Munich (2009). “Polymer optical fiber sensors for distributed strain measurement and application in structural health monitoring”. In: *IEEE Sensors Journal* 9.11, pp. 1330–1338.

Loh, Kenneth J and Jesus Gonzalez (2015). “Cementitious composites engineered with embedded carbon nanotube thin films for enhanced sensing performance”. In: *Journal of Physics: Conference Series*. Vol. 628. 1. IOP Publishing, p. 012042.

López-Almansa, Francisco, V Sarrablo, Paulo B Lourenço, Joaquim AO Barros, Pere Roca, F Da Porto, and C Modena (2010). “Reinforced brick masonry light vaults: Semi-prefabrication, construction, testing and numerical modeling”. In: *Construction and Building Materials* 24.10, pp. 1799–1814.

Lourenco, Paulo (Jan. 1996). “Computational Strategy for Masonry Structures”. In:

Lubliner, J, J Oliver, Sand Oller, and E Onate (1989). “A plastic-damage model for concrete”. In: *Smart Materials and Structures* 25.3, pp. 299–329.

Magalhães, Filipe, A Cunha, and Elsa Caetano (2012). “Vibration based structural health monitoring of an arch bridge: from automated OMA to damage detection”. In: *Mechanical Systems and Signal Processing* 28, pp. 212–228.

Martinez, M, L Gang, D Backman, A Oudovikine, and N Bellinger (2008). “Crack detection on composite and metallic aerospace structures”. In: *Structural Health Monitoring*, pp. 560–569.

Masciotta, Maria-Giovanna, Luís F Ramos, and Paulo B Lourenço (2017). “The importance of structural monitoring as a diagnosis and control tool in the restoration process of heritage structures: a case study in Portugal”. In: *Journal of Cultural Heritage* 27, pp. 36–47.

Matheron, Georges (1963). “Principles of geostatistics”. In: *Economic geology* 58.8, pp. 1246–1266.

Mesquita, Esequiel, António Arêde, Nuno Pinto, Paulo Antunes, and Humberto Varum (2018). “Long-term monitoring of a damaged historic structure using a wireless sensor network”. In: *Engineering Structures* 161, pp. 108 –117. ISSN: 0141-0296. DOI: `https://doi.org/10.1016/j.engstruct.2018.02.013`. URL: `http://www.sciencedirect.com/science/article/pii/S0141029617311549`.

Michał, Szczecina and Winnicki Andrzej. “Calibration of the CDP model parameters in Abaqus”. In:

Mooney, Sacha Jon (2002). “Three-dimensional visualization and quantification of soil macroporosity and water flow patterns using computed tomography”. In: *Soil Use and Management* 18.2, pp. 142–151.

Murphy, BS (2014). “PyKrige: development of a kriging toolkit for Python”. In: *AGU fall meeting abstracts*.

Oliphant, Travis E (2006). *A guide to NumPy*. Vol. 1. Trelgol Publishing USA.

Pepi, Chiara, Nicola Cavalagli, Massimiliano Gioffrè, and Vittorio Gusella (2019). “Dynamic Identification and Damage Detection on Masonry Buildings Using Shaking Table Tests”. In: *Conference of the Italian Association of Theoretical and Applied Mechanics*. Springer, pp. 1819–1837.

Pereira, João M and Paulo B Lourenço (2016). “Experimental characterization of masonry and masonry components at high strain rates”. In: *Journal of Materials in Civil Engineering* 29.2, p. 04016223.

Petracca, Massimo, Luca Pelà, Riccardo Rossi, Stefano Zaghi, Guido Camata, and Enrico Spacone (2017). "Micro-scale continuous and discrete numerical models for nonlinear analysis of masonry shear walls". In: *Construction and Building Materials* 149, pp. 296–314.

Pierdicca, Alessio, Francesco Clementi, Daniela Isidori, Enrico Concettoni, Cristina Cristalli, and Stefano Lenci (2016). "Numerical model upgrading of a historical masonry palace monitored with a wireless sensor network". In: *International Journal of Masonry Research and Innovation* 1.1, pp. 74–98.

Pluijm, van der, R. (1992). "Material properties of masonry and its components under tension and shear". English. In: *Proceedings 6th Canadian Masonry Symposium, 15-17 June 1992, Saskatoon, Canada.* University of Saskatchewan, pp. 675–686.

Ponnamma, Deepalekshmi, Neethu Ninan, and Sabu Thomas (2018). "Chapter 13 - Carbon Nanotube Tube Filled Polymer Nanocomposites and Their Applications in Tissue Engineering". In: *Applications of Nanomaterials.* Ed. by Sneha Mohan Bhagyaraj, Oluwatobi Samuel Oluwafemi, Nandakumar Kalarikkal, and Sabu Thomas. Micro and Nano Technologies. Woodhead Publishing, pp. 391 –414. ISBN: 978-0-08-101971-9. DOI: `https://doi.org/10.1016/B978-0-08-101971-9.00014-4`.

Qin, Shiqiang, Yazhou Zhang, Yun-Lai Zhou, and Juntao Kang (2018). "Dynamic model updating for bridge structures using the kriging model and PSO algorithm ensemble with higher vibration modes". In: *Sensors* 18.6, p. 1879.

Ramos, Luís F, Guido De Roeck, Paulo B Lourenço, and A Campos-Costa (2010). "Damage identification on arched masonry structures using ambient and random impact vibrations". In: *Engineering Structures* 32.1, pp. 146–162.

Rana, Sohel, P Subramani, Raul Fangueiro, and Antonio Gomes Correia (2016). "A review on smart self-sensing composite materials for civil engineering applications". In: *AIMS Materials Science* 3.2, pp. 357–379.

Rathod, Vivek T and Anjana Jain (2018). "Ultrasonic guided wave sensitivity of piezopolymer films subjected to thermal exposure". In: *ISSS Journal of Micro and Smart Systems* 7.1, pp. 15–24.

Ridwan, Muhammad, Isamu Yoshitake, and Ayman Y Nassif (2017). "Proposal of design formulae for equivalent elasticity of masonry structures made with bricks of low modulus". In: *Advances in Civil Engineering* 2017.

RILEM, Draft Recommendation (1985). "Determination of the fracture energy of mortar and concrete by means of three-point bend tests on notched beams". In: *Materials and structures* 18.106, pp. 285–290.

Rossum, Guido (1995). "Python reference manual". In:

Saafi, Mohamed (2009). "Wireless and embedded carbon nanotube networks for damage detection in concrete structures". In: *Nanotechnology* 20.39, p. 395502.

Sacco, Elio, Daniela Addessi, and Karam Sab (2018). "New trends in mechanics of masonry". In: *Meccanica* 53.7, pp. 1565–1569.

Sacco, Elio and Jessica Toti (Nov. 2010). "Interface Elements for the Analysis of Masonry Structures". In: *International Journal for Computational Methods in Engineering Science and Mechanics* 11, pp. 354–373. DOI: `10.1080/15502287.2010.516793`.

Sadoughi, Mohammadkazem, Austin Downey, Jin Yan, Chao Hu, and Simon Laflamme (2018a). "Reconstruction of unidirectional strain maps via iterative signal fusion for mesoscale structures monitored by a sensing skin". In: *Mechanical Systems and Signal Processing* 112, pp. 401–416.

— (2018b). "Reconstruction of unidirectional strain maps via iterative signal fusion for mesoscale structures monitored by a sensing skin". In: *Mechanical Systems and Signal Processing* 112, pp. 401–416.

Saisi, Antonella, Carmelo Gentile, Marco Guidobaldi, and Man Xu (2014). "Dynamic monitoring and seismic response of a historic masonry tower." In: *Key Engineering Materials* 628, pp. 55–60.

Saisi, Antonella, Carmelo Gentile, and Antonello Ruccolo (2018). "Continuous monitoring of a challenging heritage tower in Monza, Italy". In: *Journal of Civil Structural Health Monitoring* 8.1, pp. 77–90.

Scientific, TF (2018). "Avizo Software 9 User's Guide". In: *vol* 9, pp. 1–915.

Shah, Surendra P, MS Konsta-Gdoutos, ZS Metaxa, and P Mondal (2009). "Nanoscale modification of cementitious materials". In: *Nanotechnology in Construction 3*. Springer, pp. 125–130.

Simulia. *ABAQUS/Analysis User's and Theory Manual.* Dassault Systèmes.

Stafford, Peter J, John B Berrill, and Jarg R Pettinga (2009). "New predictive equations for Arias intensity from crustal earthquakes in New Zealand". In: *Journal of Seismology* 13.1, pp. 31–52.

Sumita, Masao, Kazuya Sakata, Shigeo Asai, Keizo Miyasaka, and Hideaki Nakagawa (1991). "Dispersion of fillers and the electrical conductivity of polymer blends filled with carbon black". In: *Polymer bulletin* 25.2, pp. 265–271.

Ubertini, F, A D'Alessandro, AL Materazzi, Simon Laflamme, and Austin Downey (2017a). "Novel nanocomposite clay brick for strain sensing in structural masonry". In: *2017 IEEE International Conference on Environment and Electrical Engineering and 2017*

IEEE Industrial and Commercial Power Systems Europe (EEEIC/I&CPS Europe). IEEE, pp. 1–4.

Ubertini, Filippo, Nicola Cavalagli, Alban Kita, and Gabriele Comanducci (2018). "Assessment of a monumental masonry bell-tower after 2016 Central Italy seismic sequence by long-term SHM". In: *Bulletin of Earthquake Engineering* 16.2, pp. 775–801.

Ubertini, Filippo, Gabriele Comanducci, Nicola Cavalagli, Anna Laura Pisello, Annibale Luigi Materazzi, and Franco Cotana (2017b). "Environmental effects on natural frequencies of the San Pietro bell tower in Perugia, Italy, and their removal for structural performance assessment". In: *Mechanical Systems and Signal Processing* 82, pp. 307–322.

Valente, Marco and Gabriele Milani (2016). "Non-linear dynamic and static analyses on eight historical masonry towers in the North-East of Italy". In: *Engineering Structures* 114, pp. 241–270.

— (2019a). "Damage assessment and collapse investigation of three historical masonry palaces under seismic actions". In: *Engineering Failure Analysis* 98, pp. 10–37.

— (2019b). "Earthquake-induced damage assessment and partial failure mechanisms of an Italian Medieval castle". In: *Engineering Failure Analysis* 99, pp. 292–309.

Valvona, Filippo, Jessica Toti, Vincenzo Gattulli, and Francesco Potenza (2017). "Effective seismic strengthening and monitoring of a masonry vault by using Glass Fiber Reinforced Cementitious Matrix with embedded Fiber Bragg Grating sensors". In: *Composites Part B: Engineering* 113, pp. 355–370.

Venanzi, Ilaria, Alban Kita, Nicola Cavalagli, Laura Ierimonti, and Filippo Ubertini (2020). "Earthquake-induced damage localization in an historic masonry tower through long-term dynamic monitoring and FE model calibration". In: *Bulletin of Earthquake Engineering* 18.5, pp. 2247–2274.

Vermeltfoort, AT, DRW Martens, and GPAG Van Zijl (2007). "Brick–mortar interface effects on masonry under compression". In: *Canadian Journal of Civil Engineering* 34.11, pp. 1475–1485.

Verstrynge, Els, Kristof De Wilder, Anastasios Drougkas, Eli Voet, Koen Van Balen, and Martine Wevers (2018). "Crack monitoring in historical masonry with distributed strain and acoustic emission sensing techniques". In: *Construction and Building Materials* 162, pp. 898–907.

Wael, W and Robert G Drysdale (2004). "3-D Finite element modelling of masonry-infilled frames with and without openings". In: *13th International Brick and Block Masonry Conference, Amsterdam.*

Wang, Hongmin, Yifan Diao, Yang Lu, Haoru Yang, Qingjun Zhou, Kenneth Chrulski, and Julio M. D'Arcy (Aug. 2020). "Energy storing bricks for stationary PEDOT supercapacitors". In: *Nature Communications* 11, p. 3882. DOI: `10.1038/s41467-020-17708-1`.

Ward, Malcolm Russell (1971). "Electrical engineering science". In:

Wen, Sihai and D.D.L. Chung (2002). "Cement-based materials for stress sensing by dielectric measurement". In:

Wen, Sihai and DDL Chung (2007). "Double percolation in the electrical conduction in carbon fiber reinforced cement-based materials". In: *Carbon* 45.2, pp. 263–267.

Wu, Chengqing and Hong Hao (2006). "Derivation of 3D masonry properties using numerical homogenization technique". In: *International journal for numerical methods in engineering* 66.11, pp. 1717–1737.

Yang, Qilin, Pengfei Liu, Zhi Ge, and Dawei Wang (2020). "Self-Sensing Carbon Nanotube-Cement Composite Material for Structural Health Monitoring of Pavements". In: *Journal of Testing and Evaluation* 48.3.

Yeo, Hong Goo, Joontaek Jung, Minkyung Sim, Jae Eun Jang, and Hongsoo Choi (2020). "Integrated Piezoelectric AlN Thin Film with SU-8/PDMS Supporting Layer for Flexible Sensor Array". In: *Sensors* 20.1, p. 315.

Yoshimura, Takashi, Toyomitsu Harada, and Hiroshi Noguchi (2004). "Three-dimensional crack detection method for structures using simulated strain gages and the body force method". In: *Journal of Testing and Evaluation* 32.2, pp. 106–113.

Zhang, Qianying and Jitao Wu (2015). "Image super-resolution using windowed ordinary Kriging interpolation". In: *Optics Communications* 336, pp. 140–145.

Zhang, Songchang, Xiaolong Zhao, Ming Ye, and Yongning He (2019). "Theoretical and Experimental Study on Electrical Contact Resistance of Metal Bolt Joints". In: *IEEE Transactions on Components, Packaging and Manufacturing Technology* 9.7, pp. 1301–1309.

Zienkiewicz, Olgierd Cecil, Robert Leroy Taylor, Perumal Nithiarasu, and JZ Zhu (1977). *The finite element method.* Vol. 3. McGraw-hill London.

Zizi, Mattia, Francesco Campitiello, Adrian Dogariu, and Gianfranco De Matteis (July 2017). "Cyclic response of brick-cement mortar masonry shear-walls retrofitted with steel grids". In: p. 12.